DETERMINATION OF GRATING SHAPE AND PHYSICAL MECHANISMS IN LITHIUM NIOBATE HOLOGRAPHIC RECORDING

A THESIS

Presented to

The Faculty of the Graduate Division

by

Shing-fong Su

In Partial Fulfillment

of the Requirements for the Degree

Doctor of Philosophy

in the School of Electrical Engineering

Georgia Institute of Technology

February, 1976

DETERMINATION OF GRATING SHAPE AND PHYSICAL MECHANISMS

IN LITHIUM NIOBATE HOLOGRAPHIC RECORDING

Approved:

T. K. Gaylord, Chairman

W. R. Callen

D. C. Ray

Date approved by Chairman: February 18, 1976

ACKNOWLEDGMENTS

I wish to express my gratitute to Dr. T. K. Gaylord. Without his deep insight, boundless patience, infectious enthusiasm, careful guidance, and continuous encouragement, this work could not have been done.

I am also greatly indebted to the members of the reading committee, Dr. W. R. Callen and Dr. D. C. Ray, for their valuable criticisms and suggestions. The assistance and financial support provided by the School of Electrical Engineering are greatly appreciated.

Finally, I would like to thank my wife, Bih-hwa, for her patience and encouragement during the course of my Ph. D. program.

TABLE OF CONTENTS

TABLE OF CONTENTS (Continued)

Chapter

TABLE OF CONTENTS (Continued)

LIST OF TABLES

LIST OF TABLES (Continued)

LIST OF ILLUSTRATIONS

LIST OF ILLUSTRATIONS (Continued)

LIST OF ILLUSTRATIONS (Continued)

SUMMARY

This dissertation attempts to determine the grating shape and physical mechanisms in lithium niobate holographic recording. A four part research program is conducted. The first part of this research program is a simple method of calculating arbitrary-order diffraction efficiencies of thick transmission gratings with arbitrary periodic grating shapes. The analysis uses a coupled-wave theory to obtain a closed-form expression for the diffraction efficiency of an arbitrary order. This method provides results with relative computational ease and results that are in close agreement with those obtained by extending Burckhardt's numerical method.

The second part of this research program is the investigation of the relationship between the grating shape and the physical mechanisms (diffusion and drift of charge carriers) that are occuring during hologram recording. The space-charge field patterns (and thus the grating refractive index profiles for lithium niobate crystals) generated through diffusion and drift of electrons during hologram recording in ferroelectric crystals are obtained by numerically solving the appropriate difference-differential equations. The treatment allows for the presence of an effective electric field due to the photovoltaic effect and an externally applied electric field. The results of this approach agree with those of the existing analytic approaches.

The third part of this research program presents a procedure for determining the refractive index profiles (grating shapes) of optically-

induced thick dielectric gratings in ferroelectric crystals. This procedure, based on the coupled-wave theory, requires a knowledge of the modulation ratio and the fundamental and the higher-order diffraction efficiencies of the grating. The calculational accuracy of the procedure is tested by determining the refractive index profiles from the calculated diffraction efficiencies of known grating profiles. As an illustration of the procedure, the refractive index profile of a lithium niobate holographic grating is determined from measurements of its fundamental and higher-order diffraction efficiencies.

The fourth and last part of this research program is an experimental application of the preceding procedure to a lithium niobate crystal. Three typical experiments with different experimental conditions are conducted. The holograms in these three experiments are recorded in different parts of the crystal. The diffraction efficiencies of these gratings are measured. The grating profiles of these gratings, as well as the percentage amounts of diffusion and drift in the process of hologram recording, are determined.

CHAPTER I

INTRODUCTION

1.1 Background

The principle of holography was discovered by Gabor[1] in 1948 and later extended by Leith and Upatnieks.[2-4] Holography, essentially, consists of two processes: (1) production of the hologram by interference of light beams, and (2) reconstruction of the wavefront by diffraction. In the early years, the theory of holography was based on the assumption that the hologram is recorded on a two-dimensional surface. The fact that holograms can be recorded in a three-dimensional medium was first described by Denisyuk[5] and van Heerden[6] in 1963. Denisyuk[5] assumed that the emulsion of the hologram had a finite thickness. In his recording configuration, the object beam and the reference beam impinged on the hologram from opposite sides and, therefore, a standing wave pattern was recorded in the three-dimensional emulsion. This standing wave pattern, when illuminated with light, reflects waves of the same form and wavelength as that which originally produced the pattern. Van Heerden[6] has analyzed the case where the reconstruction wave is identical to one of two original exposing waves. The impinging and diffraction properties of thick holograms (three-dimensional holograms) are significantly different from those of thin holograms (two-dimensional holograms).

Thick holograms recorded in three-dimensional emulsions have received a large share of attention over the years, whereas thick holo-

grams recorded in crystals have been relatively neglected because of a lack of extended thickness recording materials. However, recent developments in recording materials (such as lithium niobate) have led to a shift of emphasis to this area. The thickness of the recording material may be hundreds or even thousands of times greater than the wavelength of light.

1.2 Applications of Thick Holograms

Thick holograms have attracted a great deal of interest by their use in high-capacity information storage,[6] in color holography,[7] and in white-light reconstruction of holograms.[8] Thick holograms may be regarded as recordings of an infinite number of thick gratings. Thick diffraction gratings differ from thin gratings in a number of important ways. Among these are the capability of high diffraction efficiency,[9] wavelength selectivity,[9] angular selectivity,[9] and reduced noise.[10] These give rise to the use of thick gratings as highly efficient diffraction gratings, narrow-band spectral filters,[11] thick-grating optical components, such as lenses,[12] and imaging systems capable of spectral resolution of extended objects.[10] In the field of integrated optics, thick gratings may be used as diffraction gratings for surface guiding of waves,[13] for thin-film distributed-feedback lasers,[14] for frequency-selective grating reflectors in thin-film lasers,[15] for grating couplers for launching single-mode light waves into thin-film waveguides,[16,17] and for electro-optic grating deflectors and modulators.[18]

In the area of high-capacity information storage, thick holograms are especially important due to their ability to store information in

three dimensions. The theoretical storage density of two dimensional (thin) holograms is 4×10^8 bits/cm^2 (one bit per square area one wavelength on a side) whereas in three dimensional volume (thick) holograms the theoretical storage density is 8×10^{12} bits/cm^3 (one bit per cubic volume one wavelength on a side).[6] For truly high capacity storage, thick holograms (such as in optical crystals) are vastly superior to thin holograms (such as in photographic emulsions or metal films). Holographic memory systems have been described that utilize three dimensional storage.[19,20] These systems superpose many holograms at a single location inside the thick recording medium by using a different reference beam angle for each hologram. Because of their volume nature, these holograms exhibit very strong angular selectivity.[9,21] That is, in order to read a hologram, the reference beam must illuminate the hologram within a narrow angular corridor about the Bragg angle for that hologram. Illumination outside of this angular corridor produces a rapidly decreasing intensity of reconstructed data. In addition, the thicker the hologram is, the narrower the angular corridor for reconstruction becomes. The superposition of multiple holograms at a single volume location introduces the additional problem of writing new holograms in that volume without affecting those already there. When lithium niobate is used as the three dimensional storage material, this problem may be solved by the application of an external electric field.[22,23] This greatly increases the sensitivity for writing, while the sensitivity for erasure remains unchanged at a much lower value. Thus as a new hologram is written, the other holograms at that location are only slightly erased.

1.3 Motivation

The properties of thick holographic gratings are now in general well understood. However, the investigations of the higher-order diffraction efficiencies and the grating shapes (refractive index profiles) of thick gratings, so far, have not been available. The grating shapes are usually assumed to be sinusoidal because the light interference patterns are sinusoidal. But, this is not always true because of the nonlinear response of the material. In addition, as will be seen in Chapter III, different physical mechanisms (such as drift or diffusion of charge carriers) in electro-optic recording materials generate different grating shapes. Therefore, as a part of this thesis, a method of calculating arbitrary-order diffraction efficiencies of thick gratings with arbitrary grating shape is developed. In addition, a method of determining the grating shape of a thick grating by external measurements is also developed. These two methods are presented in Chapter II and Chapter IV, respectively.

The grating patterns of thick holograms are optically induced refractive index changes in the bulk material. Three different models of the physical mechanisms have been proposed[24-26] to explain the phenomenon of this optically induced refractive index change. Chen[24] explained the refractive index change by drift of photoexcited carriers under the influence of an internal field. He assumed that there are electron traps in the material. Initially, some of the traps are filled and neutral and they provide electrons upon photoexcitation. The others are empty and they capture electrons. He also assumed that there is an internal electric field in the direction opposite to that of the spontaneous

polarization. The photoexcited electrons drift toward the positive side of the field (or the spontaneous polarization) leaving behind positive charges of ionized trap centers. The photoexcited charges will be re-trapped and reexcited out of the traps until they finally drift out of the illuminated region and are trapped. Therefore, a space-charge field is created between the positive ionized centers and the trapped negative charges. This space-charge field causes the spatial variation of the refractive index via the electro-optic effect of the sample. The need for an internal field in Chen's model was removed by Glass et al.[27] by introducing the concept of high-field photoeffect. They found that the current inside the crystal is due to a bulk photovoltaic effect and not due to internal fields.

Johnston[25] proposed a light-generated polarization pattern to explain the variation of the refractive index. In his model, an extremely high density of free electrons is required to generate the large field necessary to account for the variation of the refractive index.

Another model has been proposed by Amodei.[26] He has pointed out that charge migration by diffusion is an important factor in holographic recording for sufficiently small grating periods. He has shown that even in the absence of an internal field or an externally applied field, the photoexcited electrons still can migrate out of the illuminated region by thermal processes. Further, he has derived[28] expressions for the electric field patterns generated through drift and through diffusion, respectively, for plane-wave holograms for the cases of the initial and the steady-state stages of holographic recording.

Young et al.[29] have generalized Amodei's formulation by removing

the assumption that the diffusion length is small compared to a grating period. This treatment applies only to the initial stage of hologram formation.

All of the above work has undoubtedly contributed greatly to our understanding of the formation of phase plane-wave holograms in crystals. However, in none of these investigations is a comprehensive treatment developed either to reveal the relationship between the grating profile and the exposure for the entire process of hologram recording or to determine the grating profile by measuring the diffraction efficiencies of the grating. In this dissertation, both of these two problems are solved.

1.4 Approach Taken in Thesis

The goal of this dissertation is to determine the grating shape and physical mechanisms in lithium niobate holographic recording. To achieve this goal, a four part research program is conducted. Each part of this research program is respectively presented in a chapter.

Chapter II presents a method for calculating arbitrary-order diffraction efficiencies of thick, lossless transmission gratings with arbitrary grating shapes. A Fourier-series representation of the grating profile is employed, along with a coupled-wave theory of diffraction. For illustration, numerical values of the diffraction efficiencies at the first three Bragg angles are calculated for sinusoidal, square-wave, triangular, and saw-tooth gratings. Numerical results for the same gratings with the same parameters are also calculated for comparison, by extending Burckhardt's numerical method for analyzing thick sinusoidal gratings. The comparison shows that the coupled-wave theory provides

results with relative computational ease and results that are in agreement with calculations obtained by extending the more-rigorous Burckhardt theory to nonsinusoidal grating shapes and to higher-order Bragg angles. The descriptions of the extended Burckhardt theory for H mode and E mode polarizations are presented in the appendix.

Chapter III presents the description of the relationship between the grating profile and the exposure for the entire range of exposures. This is accomplished by numerical methods. The electric field patterns generated through diffusion and drift of electrons are obtained. The treatment allows for the presence of an effective electric field due to the photovoltaic effect and an externally applied electric field. The results of this approach agree with those of the existing analytical methods.

In Chapter IV, a method for determining the refractive index profiles (grating shapes) of thick dielectric gratings is presented. This method, based on the coupled-wave theory, requires a knowledge of the modulation ratio and the fundamental and the higher-order diffraction efficiencies of the grating. The method also allows for the presence of an effective electric field due to the bulk photovoltaic effect and an externally applied electric field. The calculational accuracy of the method is tested by determining the grating profile from the calculated diffraction efficiencies of known grating profiles. In addition, as an illustration of the method, the grating profile of a lithium niobate holographic grating is determined from measurements of its fundamental and higher-order diffraction efficiencies.

In Chapter V, three typical experiments under different experimen-

tal conditions are presented. The diffraction efficiencies of the gratings are measured. With these diffraction efficiency data, the refractive index profiles of the gratings are determined using the method described in Chapter IV. The magnitude as well as the direction of the effective electric field during recording is estimated by means of the least square best fit of the analytical expression to the predicted grating profile. The relative amounts of diffusion and drift in a hologram recording are also calculated.

CHAPTER II

ARBITRARY-ORDER DIFFRACTION EFFICIENCIES OF THICK GRATINGS[30]

2.1 Introduction

The diffraction of a plane wave by a thick sinusoidal grating at or near Bragg incidence has been considered by Burckhardt[31] and by Kogelnik.[9] Burckhardt has treated this case by solving the exact electromagnetic boundary-value problem and has obtained numerical results with a digital computer to determine the eigenvalues of a matrix and to solve the resulting set of linear algebraic equations. Kogelnik has obtained a closed-form expression for the diffraction efficiency at the first-order Bragg angle by employing a coupled-wave theory. Coupled-wave theories have been used successfully in the treatment of light diffraction by acoustic waves.[32,33] Recently, Chu and Tamir[34] treated this problem by using a guided-wave technique. They assumed sinusoidal modulation of the relative permittivity by the sound wave. Their treatment was based on a rigorous modal approach, utilizing the interrelationships between the characteristic-mode and the coupled-mode representations. With their method, not only the diffraction efficiency at the first order but also that of any higher order can be obtained.

In this chapter, the coupled-wave approach is extended to examine the first- and higher-order diffraction efficiencies of thick, arbitrary-shape gratings. Because of the periodicity of the grating, a Fourier-series representation of the grating is employed. The gratings are

assumed to be lossless. The reflections at surfaces of the gratings are at first neglected in the derivation, because, in practice, these can be eliminated by antireflection coatings. When surface and internal reflections are present, the results are corrected by a multiplicative transmittance factor.[35] For illustration, numerical values of the diffraction efficiencies at the first three Bragg angles are calculated for sinusoidal, square-wave, triangular, and saw-tooth gratings. For comparison, numerical results for the same grating shapes with the same parameters are also calculated by extending Burckhardt's numerical method (see Appendix). The comparison shows that the results from these two methods are in close agreement and that the present method is computationally simpler and more efficient.

2.2 Theoretical Analysis

The model for a thick periodic grating is represented by Fig. 1. The x axis is chosen in the plane of incidence and parallel to the surfaces of the medium, the z axis is perpendicular to the surfaces of the medium, and the y axis is perpendicular to the page. For convenience, the fringe planes of the grating are assumed to be perpendicular to the surfaces of the medium and to the plane of incidence. The grating vector $\vec{K}$ is, therefore, parallel to the x axis. Thus, for lossless periodic gratings, the fringes of the grating can be represented by a spatial modulation of the relative dielectric constant

$$\varepsilon_r(x) = \frac{\varepsilon(x)}{\varepsilon_o} = \varepsilon_{ro} + \sum_{h=1}^{\infty} \left[\varepsilon_{ch}\cos(hKx) + \varepsilon_{sh}\sin(hKx)\right], \qquad (1)$$

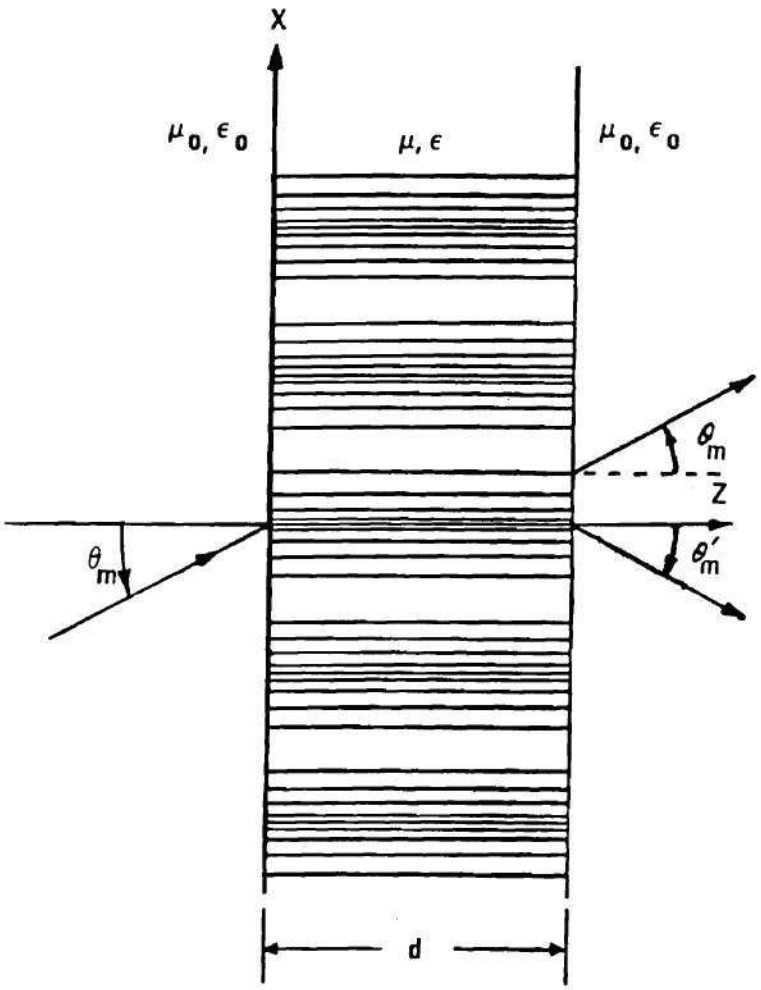

Figure 1. Geometry of a Thick Grating with Unslanted Fringes.

where $K = 2\pi/L$, L is the period of the grating, ε_{ro} is the average value of ε_r, and ε_{ch} and ε_{sh} are the spatial modulations of ε_r, the subscripts c, s, and h denote the quantities connected with the cosine gratings, the sine gratings, and the h th-harmonic grating, respectively. Corresponding to the distribution of the relative dielectric constant, the distribution of the refractive index of the medium is

$$n(x) = n_o + \sum_{h=1}^{\infty} \left[n_{ch}\cos(hKx) + n_{sh}\sin(hKx) \right], \qquad (2)$$

where n_o is the average refractive index of the medium, and n_{ch} and n_{sh} are the spatial modulations of n ($n_o >> n_{ch}, n_{sh}$).

There are two typical polarizations for the electric field of the incident wave; it can be polarized either perpendicular to or parallel to the plane of incidence.

2.2.1 H-Mode Polarization

In this case, the electric field of the incident wave is polarized perpendicular to the plane of incidence. Assume that the incident wave is of the form $\exp[j(\eta_o x + \xi_o z - \omega_o t)]$. The wave propagation in the grating can be described by the scalar wave equation

$$\left[\nabla^2 + k^2 \varepsilon_r(x)\right] E(x,z) = 0, \qquad (3)$$

where $k = 2\pi/\lambda_r$, λ_r is the free-space wavelength of the incident (reading) plane wave, and E(x,z) is the complex amplitude of the y component of the electric field, which is independent of y.

Equation (3) has been solved by Burckhardt,[31] using separation of

variables, an infinite-series solution for the x-dependent equation, and a matrix method to solve the eigenvalue problem associated with a truncated set of the resulting infinite system of equations. This approach has been used to obtain numerical results for sinusoidal gratings. Kaspar[36] has extended Burckhardt's method to find the diffraction efficiency for nonsinusoidal absorption gratings. He has pointed out that when the absorption is strong, the phase-grating contribution to the diffraction efficiency is very small.

Chu and Tamir[34] have shown that the field inside the grating can be described in terms of coupled modes if the modulations of the relative dielectric constant (or the refractive index) are very small. In general, in addition to the zeroth mode, many higher-order modes are excited, because of the presence of the grating. For an incident wave (zero-order mode) of wavelength λ_r and at an incident angle θ, the fundamental grating will diffract this wave if the Bragg condition, $m\lambda_r = 2L \sin\theta$, is satisfied or nearly satisfied. For this particular wavelength and angle, the harmonic gratings may or may not produce diffraction, depending on whether or not their corresponding Bragg conditions are satisfied or nearly satisfied. These diffracted modes of the fundamental and the harmonic gratings propagate in the same direction.

The dimensionless quantities

$$q_{ch} = 2(L/h\lambda_r)^2 \varepsilon_{ch}, \qquad h = 1, 2, 3, \cdots, \tag{4}$$

and

$$q_{sh} = 2(L/h\lambda_r)^2 \varepsilon_{sh}, \qquad h = 1, 2, 3, \cdots \tag{5}$$

are called the effective-modulation indices.[34,37] Because ε_{ch} and ε_{sh} would typically be 10^{-4} or smaller, q_{ch} and q_{sh} are small even if L is many times as large as λ_r. For example, if $\theta = 5^o$ and $\varepsilon_{cl} = 10^{-4}$, then $q_{cl} = 0.0066$. When q is very small compared to unity, it can be shown[34] that two coupled-wave equations and therefore two modes are sufficient to describe the coupling effects when the incident angle is equal to or near the Bragg angle. Therefore, for an incident wave of wavelength λ_r and at an angle θ_m, the electric field inside the grating can be written as the sum of the fundamental mode and an arbitrary mode

$$\tilde{E}(x, z) = \tilde{S}_o(z)\exp(j\tilde{\eta}_o x) + \tilde{S}_m(z)\exp(j\tilde{\eta}_m x), \tag{6}$$

where $\tilde{\eta}_o$ and $\tilde{\eta}_m$ are the zeroth-mode and the m th-mode (with respect to the fundamental grating) transverse wave numbers, respectively. The continuity of the electric field at z = 0 and the Floquet theorem require that $\tilde{\eta}_o = \eta_o = k \sin\theta_m$ and $\tilde{\eta}_m = \eta_m = \eta_o - 2m\pi/L$. The notations with $\sim$ on the head denote the quantities inside the dielectric medium when the gratings are present. The integer subscript m represents the m th-order diffraction. The integer h represents the h th-harmonic grating. Diffraction occurs when the h th-harmonic grating satisfies or nearly satisfies the Bragg condition $m_h \lambda_r = 2(L/h) \sin\theta_m$, where m_h represents the m_h th-mode (with respect to the h th-harmonic grating) excited due to the h th-harmonic grating. Exact Bragg conditions occur when m_h is equal to m/h, where h divides evenly into m. Near-Bragg conditions occur for

the wavelength λ_r when (i) the angle of incidence is near, but not equal to θ_m and/or (ii) when the value of m is large, and h divides nearly evenly into m, so that m/h is almost an integer. Thus $\tilde{S}_m(z)$ in Eq. (6) represents the total amplitude, together with the propagation factor in the z direction, of the diffracted mode due to all of the gratings that satisfy or nearly satisfy the foregoing Bragg condition. At the boundary z = d, $\tilde{S}_o$ propagates at the angle θ_m, whereas $\tilde{S}_m$ propagates at an angle θ_m', which is determined by

$$\theta_m' = - \sin^{-1}(\eta_m/k) = - \sin^{-1}(\sin\theta_m - m\lambda_r/L). \tag{7}$$

The diffracted modes due to the gratings that are far from obeying the Bragg condition are assumed to be negligibly small compared with $\tilde{S}_o$ and $\tilde{S}_m$. Therefore, the interaction between $\tilde{S}_o$ and $\tilde{S}_m$ can be characterized by the coupled-wave euations[39]

$$\frac{d\tilde{S}_o}{dz} - j\bar{\xi}_o\tilde{S}_o - j\left(\sum_h^m (C_{chm_h} + jC_{shm_h})\right)\tilde{S}_m = 0, \tag{8}$$

$$\frac{d\tilde{S}_m}{dz} - j\bar{\xi}_m\tilde{S}_m - j\left(\sum_h^m (C_{chm_h} - jC_{shm_h})\right)\tilde{S}_o = 0, \tag{9}$$

where $\bar{\xi}_o$ and $\bar{\xi}_m$ are the longitudinal wave numbers inside the medium when the gratings are absent. They are given by $\bar{\xi}_o = k(\varepsilon_{ro})^{\frac{1}{2}}\cos\phi_m$ and $\bar{\xi}_m = \{k^2\varepsilon_{ro} - [k(\varepsilon_{ro})^{\frac{1}{2}}\sin\phi_m - (2m\pi/L)]^2\}^{\frac{1}{2}}$, where ϕ_m, the refraction angle in the medium, is given by $\phi_m = \sin^{-1}[(\sin\theta_m)/(\varepsilon_{ro})^{\frac{1}{2}}]$. The notations with a bar on the head denote the quantities inside the medium when the gratings

are absent. For a given value of the integer m, the subscript h may be any integer that divides evenly or nearly evenly into m, provided that the corresponding h th-harmonic grating exists. The symbol $\sum_{h}^{m}$ denotes the summation over all of these possible values of h. The coupling coefficients in Eqs. (8) and (9) are given by[34,38]

$$C_{chm_h} = \frac{1}{\bar{\xi}_o + \bar{\xi}_m} \left(\frac{1}{(2)^{(m_h-1)}(m_h - 1)!} \right)^2 \left(\frac{\pi}{L/h} \right)^2 \left\{ \left[(q_{ch})^2 + (q_{sh})^2 \right]^{\frac{1}{2}} \right\}^{m_h}$$

$$\times \cos\left[m_h \tan^{-1}(\epsilon_{sh}/\epsilon_{ch}) \right], \tag{10}$$

$$C_{shm_h} = \frac{1}{\bar{\xi}_o + \bar{\xi}_m} \left(\frac{1}{(2)^{(m_h-1)}(m_h - 1)!} \right)^2 \left(\frac{\pi}{L/h} \right)^2 \left\{ \left[(q_{ch})^2 + (q_{sh})^2 \right]^{\frac{1}{2}} \right\}^{m_h}$$

$$\times \sin\left[m_h \tan^{-1}(\epsilon_{sh}/\epsilon_{ch}) \right]. \tag{11}$$

If the grating does not exist, $C_{chm_h} = C_{shm_h} = 0$, there is no coupling between $\bar{S}_o$ and $\bar{S}_m$ and therefore no diffraction. Under this condition, only Eq. (8) has physical significance. It represents the propagation of the fundamental mode (incident wave) inside the medium.

The solutions of Eqs. (8) and (9) are of the form

$$\tilde{S}_o(z) = A_o \exp(j\tilde{\xi}_o z) + B_o \exp(j\tilde{\xi}_m z), \tag{12}$$

$$\tilde{S}_m(z) = A_m \exp(j\tilde{\xi}_o z) + B_m \exp(j\tilde{\xi}_m z). \tag{13}$$

The wave numbers $\tilde{\xi}_o$ and $\tilde{\xi}_m$ can be found directly by substituting Eqs. (12) and (13) into Eqs. (8) and (9). They are

$$\tilde{\xi}_{o,m} = \frac{\bar{\xi}_o + \bar{\xi}_m}{2} \pm \left[\left(\frac{\bar{\xi}_o - \bar{\xi}_m}{2} \right)^2 + \left(\sum_h^m C_{chm_h} \right)^2 + \left(\sum_h^m C_{shm_h} \right)^2 \right]^{\frac{1}{2}}, \quad (14)$$

where the plus sign corresponds to $\tilde{\xi}_o$ and the minus sign to $\tilde{\xi}_m$. The constants A_o, B_o, A_m, and B_m are determined by the boundary conditions and

$$\left(\sum_h^m (C_{chm_h} - jC_{shm_h}) \right) A_o - (\tilde{\xi}_o - \bar{\xi}_m) A_m = 0, \quad (15)$$

$$\left(\sum_h^m (C_{chm_h} - jC_{shm_h}) \right) B_o - (\tilde{\xi}_m - \bar{\xi}_m) B_m = 0, \quad (16)$$

which are obtained from Eqs. (9), (12), and (13). To specify the boundary conditions, the amplitude of the incident wave is assumed to be unity at $z = 0$ so that, from Eq. (12),

$$\tilde{S}_o(0) = A_o + B_o = 1. \quad (17)$$

Initially, the amplitude of the diffracted wave is zero. Therefore, evaluating Eq. (13) at $z = 0$ gives

$$\tilde{S}_m(0) = A_m + B_m = 0. \quad (18)$$

Solving Eqs. (15), (16), (17), and (18) for A_o, B_o, A_m, and B_m gives

$$A_o = \frac{\tilde{\xi}_o - \bar{\xi}_m}{\tilde{\xi}_o - \tilde{\xi}_m}$$

$$= \frac{1}{2}\left((\bar{\xi}_o - \bar{\xi}_m) + \left\{(\bar{\xi}_o - \bar{\xi}_m)^2 + 4\left[\left(\sum_h^m C_{chm_h}\right)^2 + \left(\sum_h^m C_{shm_h}\right)^2\right]\right\}^{\frac{1}{2}}\right) \Bigg/$$

$$\left(\left\{(\bar{\xi}_o - \bar{\xi}_m)^2 + 4\left[\left(\sum_h^m C_{chm_h}\right)^2 + \left(\sum_h^m C_{shm_h}\right)^2\right]\right\}^{\frac{1}{2}}\right), \qquad (19)$$

$$B_o = \frac{\bar{\xi}_m - \tilde{\xi}_m}{\tilde{\xi}_o - \tilde{\xi}_m}$$

$$= \frac{1}{2}\left((\bar{\xi}_m - \bar{\xi}_o) + \left\{(\bar{\xi}_o - \bar{\xi}_m)^2 + 4\left[\left(\sum_h^m C_{chm_h}\right)^2 + \left(\sum_h^m C_{shm_h}\right)^2\right]\right\}^{\frac{1}{2}}\right) \Bigg/$$

$$\left(\left\{(\bar{\xi}_o - \bar{\xi}_m)^2 + 4\left[\left(\sum_h^m C_{chm_h}\right)^2 + \left(\sum_h^m C_{shm_h}\right)^2\right]\right\}^{\frac{1}{2}}\right), \qquad (20)$$

$$A_m = -B_m$$

$$= \left[\left(\sum_h^m C_{chm_h}\right) - j\left(\sum_h^m C_{shm_h}\right)\right] \Bigg/ \left(\left\{(\bar{\xi}_o - \bar{\xi}_m)^2\right.\right.$$

$$\left.\left. + 4\left[\left(\sum_h^m C_{chm_h}\right)^2 + \left(\sum_h^m C_{shm_h}\right)^2\right]\right\}^{\frac{1}{2}}\right). \qquad (21)$$

For the exact Bragg condition, $\bar{\xi}_m = \bar{\xi}_o$ and $\theta_m' = \theta_m$. Hence, Eqs. (14), (19), (20), and (21) become

$$\tilde{\xi}_{o,m} = \bar{\xi}_o \pm \left[\left(\sum_h^m C_{chm_h}\right)^2 + \left(\sum_h^m C_{shm_h}\right)^2\right]^{\frac{1}{2}}, \qquad (22)$$

$$A_o = \frac{1}{2} = B_o, \qquad (23)$$

$$A_m = -B_m = \frac{1}{2}\left[\left(\sum_h^m C_{chm_h}\right) - j\left(\sum_h^m C_{shm_h}\right)\right] \Bigg/ \left\{\left[\left(\sum_h^m C_{chm_h}\right)^2 + \left(\sum_h^m C_{shm_h}\right)^2\right]^{\frac{1}{2}}\right\}. \quad (24)$$

Thus, the transmitted and the diffracted modes are

$$S_o(z) = \exp(j\bar{\xi}_o z)\cos\left\{\left[\left(\sum_h^m C_{chm_h}\right)^2 + \left(\sum_h^m C_{shm_h}\right)^2\right]^{\frac{1}{2}} z\right\}, \quad (25)$$

$$S_m(z) = j2A_m \exp(j\bar{\xi}_o z)$$

$$\times \sin\left\{\left[\left(\sum_h^m C_{chm_h}\right)^2 + \left(\sum_h^m C_{shm_h}\right)^2\right]^{\frac{1}{2}} z\right\}, \quad (26)$$

where C_{chm_h} and C_{shm_h} are given by Eqs. (10) and (11) with $\bar{\xi}_m = \bar{\xi}_o$, and A_m is given by Eq. (24). Equation (26) is the general formula for the m th-diffracted mode due to any periodic grating when the incident angle of the zeroth mode satisfies the Bragg condition $m\lambda_r = 2L \sin\theta_m$. The diffraction efficiency for the m th order of diffraction is defined as

$$DE_m = \tilde{S}_m(d)\, \tilde{S}_m^*(d) / \tilde{S}_o(0)\, \tilde{S}_o^*(0), \quad (27)$$

where the asterisk denotes complex conjugate. For exact Bragg conditions,

$$DE_m = \sin^2\left\{\left[\left(\sum_h^m C_{chm_h}\right)^2 + \left(\sum_h^m C_{shm_h}\right)^2\right]^{\frac{1}{2}} d\right\}. \quad (28)$$

Upon substituting Eqs. (10) and (11), with $\bar{\xi}_m = \bar{\xi}_o$, into Eq. (20) and

performing some algebraic manipulations, we find that

$$DE_m = \sin^2\Bigg(\Bigg\{\Bigg[\sum_{h}^{m} \frac{\pi}{(2)^{m_h}}\left(\frac{L^{(m_h-1)}}{(m_h-1)!(h)^{(m_h-1)}}\right)^2 \times \frac{\{[(\varepsilon_{ch})^2+(\varepsilon_{sh})^2]^{\frac{1}{2}}\}^{m_h}}{(\lambda_r)^{(2m_h-1)}} \frac{\cos[m_h\tan^{-1}(\varepsilon_{sh}/\varepsilon_{ch})]}{(\varepsilon_{ro})^{\frac{1}{2}}\cos\phi_m}\Bigg]^2 + \Bigg[\sum_{h}^{m} \frac{\pi}{(2)^{m_h}}\left(\frac{L^{(m_h-1)}}{(m_h-1)!(h)^{(m_h-1)}}\right)^2 \frac{\{[(\varepsilon_{ch})^2+(\varepsilon_{sh})^2]^{\frac{1}{2}}\}^{m_h}}{(\lambda_r)^{(2m_h-1)}} \times \frac{\sin[m_h\tan^{-1}(\varepsilon_{sh}/\varepsilon_{ch})]}{(\varepsilon_{ro})^{\frac{1}{2}}\cos\phi_m}\Bigg]^2\Bigg\}^{\frac{1}{2}} d\Bigg). \tag{29}$$

Equation (29) is the general expression for the diffraction efficiency at the m th-order Bragg angle for a periodic grating of arbitrary grating shape. For example, the first-, second-, and third-order diffraction efficiencies for a grating, whose dielectric constant profile can be expressed as a Fourier sine series, are

$$DE_1 = \sin^2\left(\frac{\varepsilon_{s1}\pi d}{2\lambda_r(\varepsilon_{ro})^{\frac{1}{2}}\cos\phi_1}\right), \tag{30}$$

$$DE_2 = \sin^2\left[\left(\frac{L^4(\varepsilon_{s1})^4}{4(\lambda_r)^4} + (\varepsilon_{s2})^2\right)^{\frac{1}{2}} \frac{\pi d}{2\lambda_r(\varepsilon_{ro})^{\frac{1}{2}}\cos\phi_2}\right], \tag{31}$$

and

$$DE_3 = \sin^2\left[\left(\varepsilon_{s3} - \frac{L^4(\varepsilon_{s1})^3}{16(\lambda_r)^4}\right)\frac{\pi\, d}{2\lambda_r(\varepsilon_{ro})^{\frac{1}{2}}\cos\phi_3}\right]. \qquad (32)$$

In Eqs. (30), (31), and (32), only the Fourier grating components ε_{s1}, ε_{s2}, and ε_{s3} are required to evaluate the diffraction efficiencies DE_1, DE_2, and DE_3. Table 1 gives these Fourier components, normalized to the amplitude of the fundamental grating ε_{s1} for gratings having sinusoidal, square-wave, triangular, and saw-tooth dielectric constant profiles. Note that the sinusoidal, square-wave, and triangular grating shapes can each be represented by a Fourier cosine series also. In this case, the resultant diffraction-efficiency expressions contain only ε_{c1}, ε_{c2}, and ε_{c3}. If $n_{ch} \ll n_o$ and $n_{sh} \ll n_o$, which are true in most cases,[9] it can be shown that $\varepsilon_{ch} = 2n_o n_{ch}$ and $\varepsilon_{sh} = 2n_o n_{sh}$. Therefore, with $(\varepsilon_{ro})^{\frac{1}{2}} = n_o$, Eq. (29) becomes

$$DE_m = \sin^2\left(\left\{\left[\sum_h^m \left(\frac{L^{(m_h-1)}}{(m_h-1)!(h)^{(m_h-1)}}\right)^2 (n_o)^{(m_h-1)}\right.\right.\right.$$

$$\left.\times \frac{\left\{\left[(n_{ch})^2 + (n_{sh})^2\right]^{\frac{1}{2}}\right\}^{m_h}}{(\lambda_r)^{(2m_h-1)}} \cos\left[m_h \tan^{-1}(n_{sh}/n_{ch})\right]\right]^2$$

$$+\left[\sum_h^m \left(\frac{L^{(m_h-1)}}{(m_h-1)!(h)^{(m_h-1)}}\right)^2 (n_o)^{(m_h-1)}\right.$$

$$\left.\left.\left.\times \frac{\left\{\left[(n_{ch})^2 + (n_{sh})^2\right]^{\frac{1}{2}}\right\}^{m_h}}{(\lambda_r)^{(2m_h-1)}} \sin\left[m_h \tan^{-1}(n_{sh}/n_{ch})\right]\right]^2\right\}^{\frac{1}{2}} \frac{\pi\, d}{\cos\phi_m}\right). \qquad (33)$$

Table 1. First Three Fourier Components for Various Relative Dielectric Constant Profiles (Grating Shapes). Components are Normalized to the Amplitude of the Fundamental Grating ε_{s1}.

Grating component	Sinusoidal grating	Square-wave grating	Triangular grating	Saw-tooth grating
$\varepsilon_{s1}/\varepsilon_{s1}$	1	1	1	1
$\varepsilon_{s2}/\varepsilon_{s1}$	0	0	0	-1/2
$\varepsilon_{s3}/\varepsilon_{s1}$	0	1/3	-1/9	1/3

The results calculated with Eqs. (30) - (32) do not agree with those calculated by use of Burckhardt's matrix method. This is because Burckhardt takes the boundary reflections into account, whereas they are not included in the foregoing derivation. The results may be corrected to include boundary reflections by multiplying the diffraction efficiency by the transmittance factor

$$\tau_m = (1 - R_m)^2 \left[1 + 2R_m\cos(2\beta_m d) + (R_m)^2\right]/\{\left[1 - (R_m)^2\right]^2 + 4(R_m)^2$$

$$x \left[\cos^2(2\nu_m d) + \cos^2(2\beta_m d)\right] - 4R_m\left[1 + (R_m)^2\right]\cos(2\nu_m d)\cos(2\beta_m d)\}, \quad (34)$$

where $R_m = \sin^2(\theta_m - \phi_m)/\sin^2(\theta_m + \phi_m)$, $\beta_m = 2\pi(\varepsilon_{ro})^{\frac{1}{2}}(\cos\phi_m)/\lambda_r$, and $\nu_m = \left[(\Sigma_h^m C_{chm_h})^2 + (\Sigma_h^m C_{shm_h})^2\right]^{\frac{1}{2}}$ evaluated with $\bar{\xi}_m = \bar{\xi}_o$ for exact Bragg conditions. This factor is the same as the transmittance factor derived by Kogelnik and given as Eq. (8) in Ref. 35, but with νd in that equation replaced by the argument of the squared sine function in Eq. (28). This allows generalization to higher diffraction orders and non-sinusoidal gratings.

2.2.2 E-Mode Polarization

When the electric field of the incident wave is polarized parallel to the plane of incidence (E-mode polarization) and also of the form $\exp\left[j(\eta_o x + \xi_o z - \omega_o t)\right]$, the wave equation that describes the wave propagation in the grating is

$$\nabla^2\vec{E} - \nabla(\nabla\cdot\vec{E}) + k^2\varepsilon_r(x)\vec{E} = 0. \quad (35)$$

Here, in contrast to Eq. (3), the electric field is described by the vector quantity $\vec{E}$ and the term $\nabla(\nabla \cdot \vec{E})$ is not necessarily zero. However, the electric field inside the grating can also be written as the sum of the fundamental and an arbitrary mode as given by Eq. (6), but with the scalar quantities $\tilde{E}$, $\tilde{S}_o$, and $\tilde{S}_m$ replaced by the vector quantities $\tilde{\vec{E}}$, $\tilde{\vec{S}}_o$, and $\tilde{\vec{S}}_m$, respectively.

Assume that both $\vec{S}_o$ and $\vec{S}_m$ represent transverse waves and that the polarizations of $\vec{S}_o$ and $\vec{S}_m$ do not change inside the grating. Then,

$$\tilde{\vec{S}}_o(z) = \tilde{S}_o(z)\hat{s}_o, \tag{36}$$

$$\tilde{\vec{S}}_m(z) = \tilde{S}_m(z)\hat{s}_m, \tag{37}$$

where $\tilde{S}_o(z)$ and $\tilde{S}_m(z)$ are the scalar amplitudes of the two waves and $\hat{s}_o$ and $\hat{s}_m$ are the unit polarization vectors independent of z. Therefore, the coupled-wave equations for this case are

$$\frac{d\tilde{S}_o}{dz}\hat{s}_o - j\bar{\xi}_o\tilde{S}_o\hat{s}_o - j\left(\sum_h^m (C_{chm_h} + jC_{shm_h})\right)\tilde{S}_m\hat{s}_m = 0, \tag{38}$$

and

$$\frac{d\tilde{S}_m}{dz}\hat{s}_m - j\bar{\xi}_m\tilde{S}_m\hat{s}_m - j\left(\sum_h^m (C_{chm_h} - jC_{shm_h})\right)\tilde{S}_o\hat{s}_o = 0. \tag{39}$$

After forming the dot product of $\hat{s}_o$ with Eq. (38) and of $\hat{s}_m$ with Eq. (39), we have

$$\frac{d\tilde{S}_o}{dz} - j\,\bar{\xi}_o\tilde{S}_o - j\left(\sum_h^m \left(C_{chm_h} + jC_{shm_h}\right)\right)(\hat{s}_o \cdot \hat{s}_m)\,\tilde{S}_m = 0, \quad (40)$$

$$\frac{d\tilde{S}_m}{dz} - j\,\bar{\xi}_m\tilde{S}_m - j\left(\sum_h^m \left(C_{chm_h} - jC_{shm_h}\right)\right)(\hat{s}_o \cdot \hat{s}_m)\,\tilde{S}_o = 0. \quad (41)$$

They are similar in form to Eqs. (8) and (9). The only difference is a reduction of the effective coupling coefficients by the dot product $(\hat{s}_o \cdot \hat{s}_m)$ of the two unit polarization-vectors. For transverse waves, it can be shown that $(\hat{s}_o \cdot \hat{s}_m)$ is equal to $\cos(2\theta_m)$. Therefore, similar to the solutions for H-mode polarization, the general expression for the E-mode diffraction efficiency at the m th-order Bragg angle of an arbitrary periodic thick transmission grating is given by

$$DE_m = \sin^2\left(\left\{\left[\sum_h^m \frac{\pi}{(2)^{m_h}}\left(\frac{L^{(m_h-1)}}{(m_h-1)!(h)^{(m_h-1)}}\right)^2 \times \frac{\left\{\left[(\epsilon_{ch})^2 + (\epsilon_{sh})^2\right]^{\frac{1}{2}}\right\}^{m_h}}{(\lambda_r)^{(2m_h-1)}} \frac{\cos\left[m_h \tan^{-1}(\epsilon_{sh}/\epsilon_{ch})\right]}{(\epsilon_{ro})^{\frac{1}{2}}\cos\phi_m}\right]^2 + \left[\sum_h^m \frac{\pi}{(2)^{m_h}}\left(\frac{L^{(m_h-1)}}{(m_h-1)!(h)^{(m_h-1)}}\right)^2 \frac{\left\{\left[(\epsilon_{ch})^2 + (\epsilon_{sh})^2\right]^{\frac{1}{2}}\right\}^{m_h}}{(\lambda_r)^{(2m_h-1)}} \times \frac{\sin\left[m_h \tan^{-1}(\epsilon_{sh}/\epsilon_{ch})\right]}{(\epsilon_{ro})^{\frac{1}{2}}\cos\phi_m}\right]^2\right\}^{\frac{1}{2}} d\cos(2\theta_m)\right). \quad (42)$$

Corresponding to Eqs. (30), (31), and (32), the first-, second-, and third-order diffraction efficiencies for a grating, whose dielectric

constant profile can be expressed as a Fourier sine series, are

$$DE_1 = \sin^2\left(\frac{\varepsilon_{s1}\pi d\cos(2\theta_1)}{2\lambda_r(\varepsilon_{ro})^{\frac{1}{2}}\cos\phi_1}\right), \tag{43}$$

$$DE_2 = \sin^2\left[\left(\frac{L^4(\varepsilon_{s1})^4}{4(\lambda_r)^4} + (\varepsilon_{s2})^2\right)^{\frac{1}{2}} \frac{\pi d\cos(2\theta_2)}{2\lambda_r(\varepsilon_{ro})^{\frac{1}{2}}\cos\phi_2}\right], \tag{44}$$

and

$$DE_3 = \sin^2\left[\left(\varepsilon_{s3} - \frac{L^4(\varepsilon_{s1})^3}{16(\lambda_r)^4}\right)\frac{\pi d\cos(2\theta_3)}{2\lambda_r(\varepsilon_{ro})^{\frac{1}{2}}\cos\phi_3}\right]. \tag{45}$$

Again, for $n_{ch} << n_o$ and $n_{sh} << n_o$, Eq. (42) can be rewritten as

$$DE_m = \sin^2\left(\left\{\left[\sum_h^m \left(\frac{L^{(m_h-1)}}{(m_h-1)!(h)^{(m_h-1)}}\right)^2 (n_o)^{(m_h-1)}\right.\right.$$

$$\left.\times \frac{\left\{\left[(n_{ch})^2 + (n_{sh})^2\right]^{\frac{1}{2}}\right\}^{m_h}}{(\lambda_r)^{(2m_h-1)}}\cos\left[m_h\tan^{-1}(n_{sh}/n_{ch})\right]\right]^2$$

$$+\left[\sum_h^m \left(\frac{L^{(m_h-1)}}{(m_h-1)!(h)^{(m_h-1)}}\right)^2 (n_o)^{(m_h-1)} \frac{\left\{\left[(n_{ch})^2 + (n_{sh})^2\right]^{\frac{1}{2}}\right\}^{m_h}}{(\lambda_r)^{(2m_h-1)}}\right.$$

$$\left.\left.\times \sin\left[m_h\tan^{-1}(n_{sh}/n_{ch})\right]\right]^2\right\}^{\frac{1}{2}} \frac{\pi d\cos(2\theta_m)}{\cos\phi_m}\Bigg). \tag{46}$$

Similar to H-mode polarization, the results of Eqs. (43), (44), and (45) may be corrected to include boundary reflections by multiplying by the transmittance factor as given by Eq. (34) but with R_m in that equation being defined as $R_m = \tan^2(\theta_m - \phi_m)/\tan^2(\theta_m + \phi_m)$. In addition, for this polarization there is a trivial case of a Bragg angle of 45° where $(\hat{s}_o \cdot \hat{s}_m) = 0$ and the intensity of the diffracted wave goes to zero.

2.3 Results and Comparison with Numerical Method

The coupled-wave analysis in the preceding section was numerically implemented on a digital computer and calculations were performed for gratings having sinusoidal, square-wave, triangular, and saw-tooth distributions of the dielectric constant.

2.3.1 Results for H-Mode Polarization

Tables 2 and 3 give numerical values for the H-mode diffraction efficiencies (without boundary reflections) at the first-, second-, and third-order Bragg angles for these gratings. Diffraction efficiencies of less than $5 \times 10^{-8}\%$ have been listed as zero in the tables. Table 2 presents data for gratings with a fundamental spacing of $L = 3.6303$ μm (resulting from recording with two beams of $\lambda_r = 632.8$ nm at $\theta_1 = \pm 5.0^\circ$). Table 3 presents data for gratings with a fundamental spacing of $L = 1.822$ μm (resulting from recording with two beams of $\lambda_r = 632.8$ nm at $\theta_1 = \pm 10.0^\circ$). The H-mode transmittance factors for these gratings are given in Tables 4 and 5. In tables 6 and 7, the H-mode diffraction efficiencies with boundary reflections included are presented for the same set of gratings. These results represent $DE_1\ \tau_1$, $DE_2\ \tau_2$, and $DE_3\ \tau_3$ as obtained from Eqs. (30) – (32) and (34) with $\varepsilon_{ro} = 2.3225$ (value used in

Refs. 30 and 34) and $\varepsilon_{sl} = 10^{-4}\varepsilon_{ro}$. For comparison, the results obtained by extending Burckhardt's numerical method (see appendix) to nonsinusoidal gratings are also shown in Tables 6 and 7. These results were calculated by programming an extension of Burckhardt's method on a digital computer and solving the eigenvalue problem and the set of linear algebraic equations. Tables 6 and 7 show that the results of these two methods are in close agreement; the deviation between these two methods does not exceed 2.8% for diffraction efficiencies larger than 5×10^{-6}%. Diffraction efficiencies smaller than 5×10^{-6}% are less significant physically because the corresponding low-level diffracted intensities are difficult to measure. In addition to the results in Tables 6 and 7, calculations were performed for other grating thickness[30] (10 and 100 μm) and another wavelength (514.5 nm). It was found that the deviation between the coupled-wave analysis and the numerical method does not exceed 6.7% for any case with a diffraction efficiency larger than 5×10^{-6}%. Typically, the percentage deviation is a few tenths of one percent.

2.3.2 Results for E-Mode Polarization

Tables 8 and 9 present the E-Mode diffraction efficiencies with boundary reflections included for the same set of gratings. These results were obtained from Eqs. (43) – (45) and (34) with the appropriate R_m. The results obtained by extending Burckhardt's method to nonsinusoidal gratings for this polarization are also given in the tables for comparison. The comparison shows that the results of these two methods are also in good agreement for this polarization.

2.3.3 Comparison with Numerical Method

Although Burckhardt's numerical approach is rigorous, a number of

Table 2. H-Mode Diffraction Efficiency in Percent at the First-, Second-, and Third-order Bragg Angles for Gratings Without Boundary Reflections and With the Same Average and Fundamental Fourier Grating Components. The Grating Parameters Are: $\varepsilon_{ro} = 2.3225$ (Value Used in Refs. 30 and 34), $\varepsilon_{sl} = 10^{-4}\varepsilon_{ro}$, $L \equiv 3.6303$ μm, and the wavelength $\lambda_r = 0.6328$ μm. Diffraction Efficiencies of Less Than 5×10^{-8}% Are Listed as 0.00(-5).

Grating thickness (microns)	Diffraction order	Diffraction Efficiency (in % with power of ten in parentheses)			
		Sinusoidal grating	Square-wave grating	Triangular grating	Saw-tooth grating
15	1	3.23(-3)	3.23(-3)	3.23(-3)	3.23(-3)
	2	0.00(-5)	0.00(-5)	0.00(-5)	8.16(-4)
	3	0.00(-5)	3.69(-4)	4.10(-5)	3.69(-4)
50	1	3.59(-2)	3.59(-2)	3.59(-2)	3.59(-2)
	2	0.05(-5)	0.05(-5)	0.05(-5)	9.06(-3)
	3	0.00(-5)	4.10(-3)	4.55(-4)	4.10(-3)
1000	1	1.37(+1)	1.37(+1)	1.37(+1)	1.37(+1)
	2	2.12(-4)	2.12(-4)	2.12(-4)	3.58(+0)
	3	0.00(-5)	1.63(+0)	1.82(-1)	1.63(+0)
1500	1	2.90(+1)	2.90(+1)	2.90(+1)	2.90(+1)
	2	4.77(-4)	4.77(-4)	4.77(-4)	7.94(+0)
	3	0.00(-5)	3.64(+0)	4.09(-1)	3.64(+0)
2000	1	4.72(+1)	4.72(+1)	4.72(+1)	4.72(+1)
	2	8.47(-4)	8.47(-4)	8.47(-4)	1.38(+1)
	3	0.00(-5)	6.41(+0)	7.26(-1)	6.41(+0)

Table 3. Same as Table 2 but for Grating Periodicity Length L = 1.8221μm.

Grating thickness (microns)	Diffraction order	Diffraction Efficiency (in % with power of ten in parentheses)			
		Sinusoidal grating	Square-wave grating	Triangular grating	Saw-tooth grating
15	1	3.26(-3)	3.26(-3)	3.26(-3)	3.26(-3)
	2	0.00(-5)	0.00(-5)	0.00(-5)	8.49(-4)
	3	0.00(-5)	4.05(-4)	4.50(-5)	4.05(-4)
50	1	3.62(-2)	3.62(-2)	3.62(-2)	3.62(-2)
	2	0.00(-5)	0.00(-5)	0.00(-5)	9.43(-3)
	3	0.00(-5)	4.50(-3)	5.00(-4)	4.50(-3)
1000	1	1.38(+1)	1.38(+1)	1.38(+1)	1.38(+1)
	2	1.40(-5)	1.40(-5)	1.40(-5)	3.73(+0)
	3	0.00(-5)	1.79(+0)	2.00(-1)	1.79(+0)
1500	1	2.92(+1)	2.92(+1)	2.92(+1)	2.92(+1)
	2	3.15(-5)	3.15(-5)	3.15(-5)	8.25(+0)
	3	0.00(-5)	4.00(+0)	4.49(-1)	4.00(+0)
2000	1	4.76(+1)	4.76(+1)	4.76(+1)	4.76(+1)
	2	5.60(-5)	5.60(-5)	5.60(-5)	1.44(+1)
	3	0.00(-5)	7.03(+0)	7.98(-1)	7.03(+0)

Table 4. H-Mode Transmittance Factor at the First-, Second-, and Third-order Bragg Angles for Gratings With the Same Average and Fundamental Fourier Grating Components. The Grating Parameters Are: $\varepsilon_{ro} = 2.3225$, $\varepsilon_{sl} = 10^{-4}\varepsilon_{ro}$, L = 3.6303 μm, and the Wavelength λ_r=0.6328 μm.

Grating thickness (microns)	Diffraction order	Transmittance Factor			
		Sinusoidal grating	Square-wave grating	Triangular grating	Saw-tooth grating
15	1	1.09	1.09	1.09	1.09
	2	0.95	0.95	0.95	0.95
	3	1.03	1.03	1.03	1.03
50	1	0.72	0.72	0.72	0.72
	2	0.91	0.91	0.91	0.91
	3	0.89	0.89	0.89	0.89
1000	1	0.89	0.89	0.89	0.89
	2	1.20	1.20	1.20	1.18
	3	1.01	1.01	1.01	1.01
1500	1	1.05	1.05	1.05	1.05
	2	0.70	0.70	0.70	0.72
	3	0.96	0.96	0.96	0.96
2000	1	0.83	0.83	0.83	0.83
	2	1.20	1.20	1.20	1.14
	3	0.74	0.75	0.74	0.75

Table 5. Same as Table 4 but for Grating Periodicity Length L = 1.8221μm.

Grating thickness (microns)	Diffraction order	Transmittance Factor			
		Sinusoidal grating	Square-wave grating	Triangular grating	Saw-tooth grating
15	1	0.96	0.96	0.96	0.96
	2	0.75	0.75	0.75	0.75
	3	1.19	1.19	1.19	1.19
50	1	0.89	0.89	0.89	0.89
	2	0.67	0.67	0.67	0.67
	3	0.74	0.74	0.74	0.74
1000	1	0.93	0.93	0.93	0.93
	2	1.11	1.11	1.11	1.10
	3	0.61	0.61	0.61	0.61
1500	1	1.01	1.01	1.01	1.01
	2	1.00	1.00	1.00	0.99
	3	0.76	0.77	0.76	0.77
2000	1	0.82	0.82	0.82	0.82
	2	0.88	0.88	0.88	0.89
	3	1.23	1.19	1.23	1.19

Table 6. Comparison of H-Mode Diffraction Efficiency in Percent at the First-, Second-, and Third-order Bragg Angles for Transmission Gratings With Boundary Reflections and With the Same Average and Fundamental Fourier Grating Components. The Grating Parameters Are $\varepsilon_{ro}=2.3225$, $\varepsilon_{s1}=10^{-4}\varepsilon_{ro}$, $L = 3.6303$ μm, and the Wavelength $\lambda_r=0.6328$ μm. Diffraction Efficiencies of Less Than 5×10^{-8}% Are Listed as 0.00(-5).

Grating thickness (microns)	Diffraction order	Diffraction Efficiency (in % with power of ten in parentheses)							
		Sinusoidal grating		Square-wave grating		Triangular grating		Saw-tooth grating	
		Coupled wave	Matrix	Coupled wave	Matrix	Coupled wave	Matrix	Coupled wave	Matrix
15	1	3.53(-3)	3.53(-3)	3.53(-3)	3.53(-3)	3.53(-3)	3.53(-3)	3.53(-3)	3.53(-3)
	2	0.00(-5)	0.00(-5)	0.00(-5)	0.00(-5)	0.00(-5)	0.01(-5)	7.75(-4)	7.73(-4)
	3	0.00(-5)	0.00(-5)	3.78(-4)	3.78(-4)	4.20(-5)	4.24(-5)	3.78(-4)	3.83(-4)
50	1	2.58(-2)	2.58(-2)	2.58(-2)	2.58(-2)	2.58(-2)	2.58(-2)	2.58(-2)	2.58(-2)
	2	0.05(-5)	0.00(-5)	0.05(-5)	0.03(-5)	0.05(-5)	0.13(-5)	8.25(-3)	8.36(-3)
	3	0.00(-5)	0.00(-5)	3.65(-3)	3.64(-3)	4.05(-4)	4.08(-4)	3.65(-3)	3.70(-3)
1000	1	1.21(+1)	1.21(+1)	1.21(+1)	1.21(+1)	1.21(+1)	1.21(+1)	1.21(+1)	1.21(+1)
	2	2.53(-4)	2.46(-4)	2.53(-4)	2.46(-4)	2.53(-4)	2.46(-4)	4.23(+0)	4.26(+0)
	3	0.00(-5)	0.00(-5)	1.64(+0)	1.64(+0)	1.83(-1)	1.84(-1)	1.64(+0)	1.66(+0)
1500	1	3.03(+1)	3.03(+1)	3.03(+1)	3.03(+1)	3.03(+1)	3.02(+1)	3.03(+1)	3.02(+1)
	2	3.33(-4)	3.12(-4)	3.33(-4)	3.12(-4)	3.33(-4)	3.12(-4)	5.69(+0)	5.75(+0)
	3	0.00(-5)	0.00(-5)	3.49(+0)	3.49(+0)	3.92(-1)	3.95(-1)	3.49(+0)	3.53(+0)
2000	1	3.92(+1)	3.92(+1)	3.92(+1)	3.92(+1)	3.92(+1)	3.91(+1)	3.92(+1)	3.91(+1)
	2	1.01(-3)	9.76(-4)	1.01(-3)	9.76(-4)	1.01(-3)	9.76(-4)	1.57(+1)	1.58(+1)
	3	0.00(-5)	0.00(-5)	4.83(+0)	4.83(+0)	5.39(-1)	5.43(-1)	4.83(+0)	4.90(+0)

Table 7. Same as Table 6 but for Grating Periodicity Length L = 1.8221 μm.

Grating thickness (microns)	Diffraction order	Diffraction Efficiency (in % with power of ten in parentheses)							
		Sinusoidal grating		Square-wave grating		Triangular grating		Saw-tooth grating	
		Coupled wave	Matrix	Coupled wave	Matrix	Coupled wave	Matrix	Coupled wave	Matrix
15	1	3.12(-3)	3.11(-3)	3.12(-3)	3.11(-3)	3.12(-3)	3.11(-3)	3.12(-3)	3.11(-3)
	2	0.00(-5)	0.00(-5)	0.00(-5)	0.00(-5)	0.00(-5)	0.00(-5)	6.41(-4)	6.46(-4)
	3	0.00(-5)	0.00(-5)	4.83(-4)	4.82(-4)	5.36(-5)	5.40(-5)	4.83(-4)	4.83(-4)
50	1	3.23(-2)	3.23(-2)	3.23(-2)	3.23(-2)	3.23(-2)	3.23(-2)	3.23(-2)	3.23(-2)
	2	0.00(-5)	0.00(-5)	0.00(-5)	0.00(-5)	0.00(-5)	0.00(-5)	6.28(-3)	6.32(-3)
	3	0.00(-5)	0.00(-5)	3.32(-3)	3.30(-3)	3.69(-4)	3.60(-4)	3.32(-3)	3.30(-3)
1000	1	1.28(+1)	1.28(+1)	1.28(+1)	1.28(+1)	1.28(+1)	1.28(+1)	1.28(+1)	1.28(+1)
	2	1.55(-5)	1.00(-5)	1.55(-5)	1.00(-5)	1.55(-5)	1.00(-5)	4.10(+0)	4.12(+0)
	3	0.00(-5)	0.07(-5)	1.09(+0)	1.09(+0)	1.21(-1)	1.23(-1)	1.09(+0)	1.08(+0)
1500	1	2.96(+1)	2.96(+1)	2.96(+1)	2.95(+1)	2.96(+1)	2.96(+1)	2.96(+1)	2.96(+1)
	2	3.15(-5)	2.50(-5)	3.15(-5)	2.50(-5)	3.15(-5)	2.50(-5)	8.16(+0)	8.21(+0)
	3	0.00(-5)	0.21(-5)	3.06(+0)	3.05(+0)	3.41(-1)	3.48(-1)	3.06(+0)	3.04(+0)
2000	1	3.92(+1)	3.92(+1)	3.92(+1)	3.91(+1)	3.92(+1)	3.92(+1)	3.92(+1)	3.92(+1)
	2	4.94(-5)	3.73(-5)	4.94(-5)	3.73(-5)	4.94(-5)	3.73(-5)	1.28(+1)	1.28(+1)
	3	0.00 -5)	0.57(-5)	8.36(+0)	8.25(+0)	9.78(-1)	9.96(-1)	8.36(+0)	8.30(+0)

Table 8. Comparison of E-Mode Diffraction Efficiency in Percent at the First-, Second-, and Third-order Bragg Angles for Transmission Gratings With Boundary Reflrctions and With the Same Average and Fundamental Fourier Grating Components. The Grating Parameters Are ε_{ro}=2.3225, $\varepsilon_{s1} = 10^{-4}\varepsilon_{ro}$, L = 3.6303 μm, and the Wavelength λ_r=0.6328 μm. Diffraction Efficiencies of Less Than 5 x 10^{-8}% Are Listed as 0.00(-5).

Grating thickness (microns)	Diffraction order	Diffraction Efficiency (in % with power of ten in parentheses)							
		Sinusoidal grating		Square-wave grating		Triangular grating		Saw-tooth grating	
		Coupled wave	Matrix	Coupled wave	Matrix	Coupled wave	Matrix	Coupled wave	Matrix
15	1	3.42(-3)	3.52(-3)	3.42(-3)	3.52(-3)	3.42(-3)	3.52(-3)	3.42(-3)	3.52(-3)
	2	0.00(-5)	0.00(-5)	0.00(-5)	0.00(-5)	0.00(-5)	0.00(-5)	6.86(-4)	6.78(-4)
	3	0.00(-5)	0.00(-5)	2.81(-4)	2.73(-4)	3.12(-5)	3.16(-5)	2.81(-4)	2.78(-4)
50	1	2.52(-2)	2.60(-2)	2.52(-2)	2.60(-2)	2.52(-2)	2.60(-2)	2.52(-2)	2.60(-2)
	2	0.00(-5)	0.06(-5)	0.00(-5)	0.05(-5)	0.00(-5)	0.05(-5)	7.34(-3)	7.40(-3)
	3	0.00(-5)	0.00(-5)	2.78(-3)	2.69(-3)	3.08(-4)	3.11(-4)	2.78(-3)	2.74(-3)
1000	1	1.18(+1)	1.21(+1)	1.18(+1)	1.21(+1)	1.18(+1)	1.21(+1)	1.18(+1)	1.21(+1)
	2	2.20(-4)	2.14(-4)	2.20(-4)	2.14(-4)	2.20(-4)	2.14(-4)	3.69(+0)	4.20(+0)
	3	0.00(-5)	0.26(-5)	1.22(+0)	1.13(+0)	1.37(-1)	1.52(-1)	1.22(+0)	1.15(+0)
1500	1	2.95(+1)	3.03(+1)	2.95(+1)	3.03(+1)	2.95(+1)	3.03(+1)	2.95(+1)	3.03(+1)
	2	3.02(-4)	2.78(-4)	3.02(-4)	2.78(-4)	3.02(-4)	2.78(-4)	5.16(+0)	5.88(+0)
	3	0.00(-5)	0.57(-5)	2.63(+0)	2.48(+0)	2.95(-1)	2.92(-1)	2.63(+0)	2.48(+0)
2000	1	3.83(+1)	3.93(+1)	3.83(+1)	3.93(+1)	3.83(+1)	3.93(+1)	3.83(+1)	3.93(+1)
	2	8.82(-4)	8.46(-4)	8.82(-4)	8.46(-4)	8.82(-4)	8.46(-4)	1.38(+1)	1.56(+1)
	3	0.00(-5)	0.80(-5)	3.79(+0)	4.04(+0)	4.23(-1)	4.65(-1)	3.79(+0)	4.04(+0)

Table 9. Same as Table 8 but for Grating Periodicity Length L = 1.8221 μm.

Grating thickness (microns)	Diffraction order	Diffraction Efficiency (in % with power of ten in parentheses)							
		Sinusoidal grating		Square-wave grating		Triangular grating		Saw-tooth grating	
		Coupled wave	Matrix	Coupled wave	Matrix	Coupled wave	Matrix	Coupled wave	Matrix
15	1	2.76(-3)	3.12(-3)	2.76(-3)	3.12(-3)	2.76(-3)	3.12(-3)	2.76(-3)	3.12(-3)
	2	0.00(-5)	0.00(-5)	0.00(-5)	0.00(-5)	0.00(-5)	0.00(-5)	4.01(-4)	4.08(-4)
	3	0.00(-5)	0.00(-5)	0.91(-4)	0.43(-4)	1.01(-5)	1.11(-5)	0.91(-4)	0.43(-4)
50	1	2.88(-2)	3.26(-2)	2.88(-2)	3.26(-2)	2.88(-2)	3.26(-2)	2.88(-2)	3.26(-2)
	2	0.00(-5)	0.00(-5)	0.00(-5)	0.00(-5)	0.00(-5)	0.00(-5)	4.08(-3)	4.21(-3)
	3	0.00(-5)	0.00(-5)	8.33(-4)	8.03(-4)	9.25(-5)	9.55(-5)	8.33(-4)	8.03(-4)
1000	1	1.14(+1)	1.28(+1)	1.14(+1)	1.28(+1)	1.14(+1)	1.28(+1)	1.14(+1)	1.28(+1)
	2	0.90(-5)	2.52(-5)	0.90(-5)	2.52(-5)	0.90(-5)	2.52(-5)	2.31(+0)	2.37(+0)
	3	0.00(-5)	0.02(-5)	3.07(-1)	3.27(-1)	3.41(-2)	3.61(-2)	3.07(-1)	3.27(-1)
1500	1	2.66(+1)	2.95(+1)	2.66(+1)	2.96(+1)	2.66(+1)	2.96(+1)	2.66(+1)	2.95(+1)
	2	1.80(-5)	5.32(-5)	1.80(-5)	5.32(-5)	1.80(-5)	5.32(-5)	4.79(+0)	4.92(+0)
	3	0.00(-5)	0.04(-5)	7.57(-1)	7.87(-1)	8.43(-2)	8.75(-2)	7.57(-1)	7.87(-1)
2000	1	3.55(+1)	3.98(+1)	3.55(+1)	3.98(+1)	3.55(+1)	3.98(+1)	3.55(+1)	3.98(+1)
	2	3.00(-5)	8.60(-5)	3.00(-5)	8.60(-5)	3.00(-5)	8.60(-5)	7.76(+0)	7.93(+0)
	3	0.00(-5)	0.09(-5)	1.63(+0)	1.83(+0)	1.82(-1)	1.98(-1)	1.63(+0)	1.83(+0)

mathematical problems such as truncation of the matrix and discarding of large positive eigenvalues must be overcome. A discussion of these is included in Ref. 31. In addition, another mathematical difficulty associated with the Burckhardt method, encountered in the present work,[30] is a singularity that arises in the process of solving a set of linear algebraic equations. For pure phase gratings, Eqs. (9) and (45) in Ref. 31 are real and symmetric. When the incident wave is at the Bragg angle, pairs of equal elements are introduced on the principal diagonal of the matrix in those equations. Thus, when the modulation amplitude is small, pairs of equal eigenvalues are usually induced. This results in a singularity in the matrix in Eqs. (34) and (63) in Ref. 31, and therefore, the equations are nonsolvable. For the parameters in the particular examples in Ref. 31, this problem does not occur because the modulation amplitude is large ($0.0035\epsilon_{ro}$). However, the modulation amplitude may, in practice, be very small (of the order 10^{-4} or smaller) and the singularity problem must, therefore, be overcome. A way to avoid the singularity is by shifting the incident angle by a negligible amount away from the Bragg angle. Physically, because the shift is negligibly small (10^{-5} degrees was used here), the incident wave can still be regarded as being incident at the Bragg angle. As an example, Fig. 2 presents the second-order diffraction efficiency of a sinusoidal grating as a function of the deviation from the second Bragg angle. In the present method, a closed-form expression for the diffraction efficiency is obtained, and no mathematical difficulties arise in the process of calculation. The computer time needed in the present method is only about 1/20 of that needed with the extended Burckhardt method to perform the same calculations.

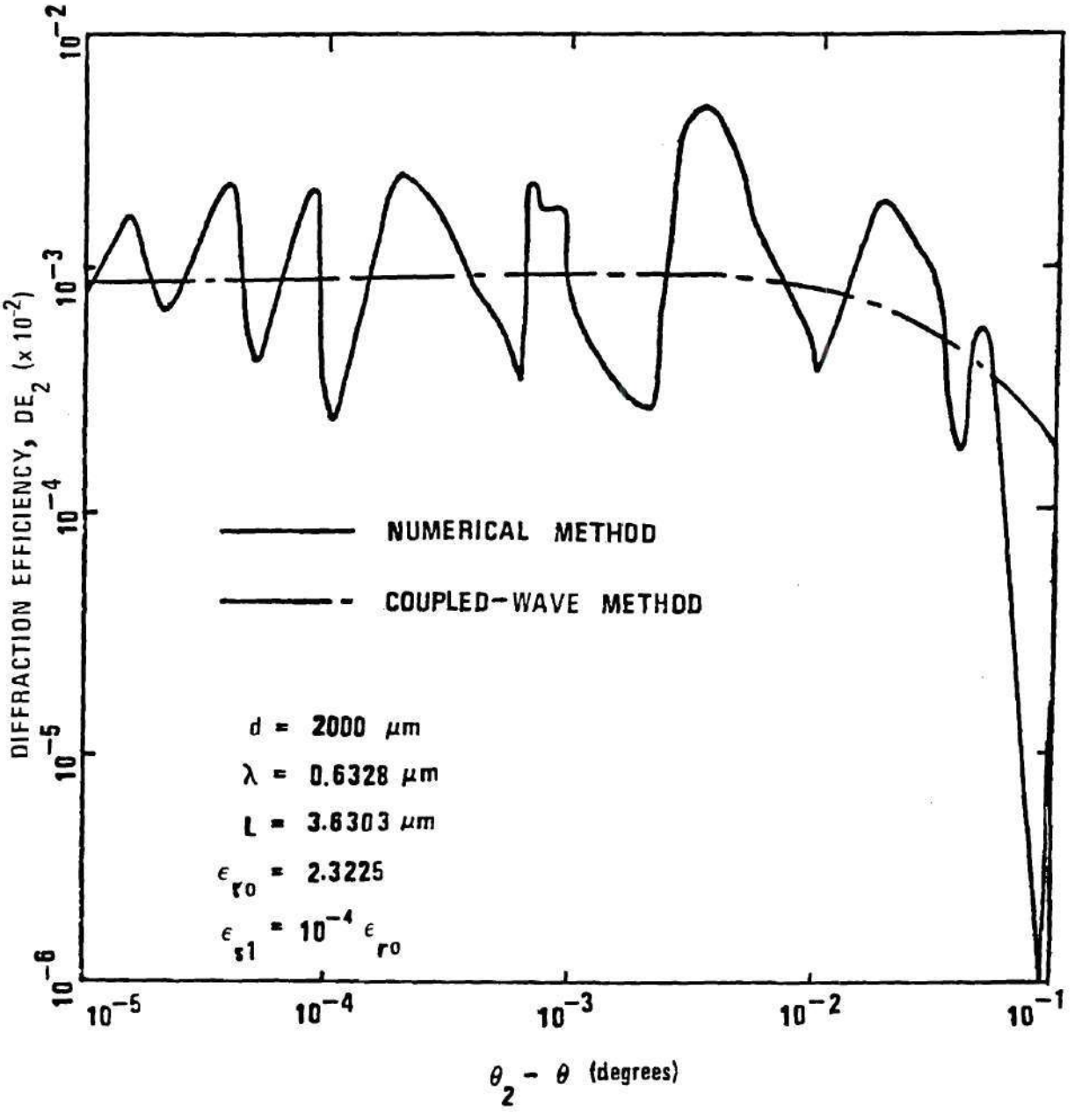

Figure 2. Second-order Diffraction Efficiency of a Sinusoidal Grating Versus Deviation from the Second Bragg Angle.

2.4 Discussion

2.4.1 Validity of Coupled-wave Theory

The coupled-wave theory is valid only for thick gratings. Historically, an appropriate measure of grating "thickness" is the parameter Q that is defined[9] as

$$Q = 2\pi\lambda_r d / n_o L^2. \tag{47}$$

We can regard a grating as thick when $Q >> 1$. It has been shown[40,41] that the coupled-wave theory begins to give good results for values of $Q = 10$. For the majority of practical holograms, the parameter Q is larger, and sometimes even much larger, than 10. However, if the modulation of the refractive index is very small, the coupled-wave theory is still valid[36] even though Q is smaller than 10. For example, for the case of the grating thickness of 15 μm as given in Table 6, the coupled-wave theory gives very good results even though Q is only 3.0.

2.4.2 Influence of Boundary Reflections

From the results, we found that boundary reflections produced by the surfaces can considerably change the diffraction efficiency. The change can be an increase or a decrease, depending on whether the transmittance factor is greater or less than unity. This effect has been studied by Cohen and Gordon.[42] For the grating parameters used here, it is typically in the range of 0.60 to 1.20. In practice, the boundary reflections can be eliminated by antireflection coatings on the surfaces of the gratings.

2.4.3 General Discussion

From the results, it is also found that the diffraction efficiency of a given higher order is mainly contributed by the corresponding higher order Fourier component of the grating. The difference between the diffraction efficiencies for sinusoidal and nonsinusoidal gratings (having the same average and fundamental grating amplitudes) appears only in the higher-order diffractions. The higher-order diffraction efficiencies, however, very strongly depend on the grating shape. Also, for small grating modulations, the diffraction efficiencies at any order are very dependent on grating thickness; they increase with increasing thickness. Marcuse[43] has suggested that, for small-amplitude thick nonsinusoidal phase gratings, the higher-order diffraction efficiencies might be estimated from the relative amplitudes of the spatial harmonics, consistent with the assumption of perturbation theory that only one Fourier component can satisfy the Bragg condition for a given wavelength incident wave. Our calculations show that this is true except when the amplitude of the harmonic grating ($h = m$) is very small compared to the amplitude of the fundamental and the lower-order contributing harmonic gratings. In this case, the contributions from higher-order diffractions ($h < m$) are significant. In addition, we found that the agreement between the coupled-wave method and the numerical method is better when the $h = m$ term is dominant over $h < m$ terms. Rigrod[44] has shown that for reflection gratings there is no correlation between higher-order diffraction efficiencies and the corresponding harmonics of the index profile. The present results show that this is not true for transmission gratings.

The present method can be used to analyze the diffraction effi-

ciency of any thick periodic grating, regardless of the dielectric constant profile (grating shape). The examples analyzed here have had even or odd symmetry. However, the method does not require any symmetry to exist, but only that the grating be periodic. From the gratings analyzed, different grating shapes have shown different distributions of higher-order diffraction efficiencies. This indicates the possibility that this type of analysis might be used in reverse to predict the grating shapes of thick hologram gratings such as those recorded in ferroelectric crystals.[45] Due to nonlinearities in these materials a sinusoidal exposure does not necessarily produce a sinusoidal change in refractive index. Depending on which of the possible physical mechanisms is operative in a given situation (such as diffusion of charge carriers or drift of carriers) different grating shapes are generated[28] (see Chapter III).

Further, the derivations in this chapter have assumed that the grating medium is lossless, that the gratings are unslanted with respect to the grating boundaries (grating vector parallel to surfaces of medium). If the medium is lossy, the results still apply, except that the coupling coefficients are complex; therefore, the attenuation factors are implicitly contained in the expressions for the transmitted wave and the diffracted wave. Likewise, slanted gratings may also be analyzed by using the theory presented here.

CHAPTER III

GRATING SHAPE AND PHYSICAL MECHANISMS IN LITHIUM NIOBATE HOLOGRAPHIC RECORDING[46]

3.1 Introduction

The recording of thick phase holograms in ferroelectric crystals was first shown in lithium niobate by Chen et al.[45] The grating patterns of the holograms were optically induced refractive index changes in the bulk material. Their work stimulated study of the theory of hologram formation in lithium niobate. Three different models of the physical mechanisms have been proposed[24-26] to explain the phenomenon of this optically induced refractive index change. Chen[24] explained the refractive index change by drift of photoexcited electrons under the influence of an internal electric field. Johnston[25] proposed a light-generated polarization pattern to explain the variation of the refractive index. Amodei[26] has pointed out that charge migration by diffusion is also an important factor in holographic recording for sufficiently small grating periods.

In this chapter the formation of plane-wave holograms for the entire range of exposure is investigated. This is accomplished by a numerical approach and both the diffusion and the drift of electrons are included. The electric field patterns, and therefore the grating shapes, generated through any combinations of these two mechanisms are obtained. Amodei[28] has treated this problem for the cases of the initial and the

final steady-state stages of hologram formation. More recently, Alphonse et al.[47] and Cornish et al.[48] have treated the same problem using analytic methods. The results of the present approach reduce to the existing analytic expressions[28] for the limiting cases of the initial and the final steady-state stages of holographic recording. The electro-optic effect for lithium niobate is linear, the magnitude of the modulation of the refractive index is proportional to the magnitude of the electric field. Therefore, the refractive index pattern caused by the electric field via the electro-optic effect is the same as the electric field patterns obtained here.

3.2 Interference Pattern and Basic Equations

3.2.1 Formation of Interference Pattern

The two plane light waves $\vec{R}$ and $\vec{S}$ of wavelength λ are symmetrically incident at an angle θ relative to the z axis as shown in Fig. 3. Assume that the wavefronts are perpendicular to the x-z plane and that the two waves are in phase. Then, they can be expressed as

$$\vec{R} = \vec{E}_1 \exp\left[j(\vec{k}_1 \cdot \vec{r} - \omega t)\right], \tag{48}$$

$$\vec{S} = \vec{E}_2 \exp\left[j(\vec{k}_2 \cdot \vec{r} - \omega t)\right], \tag{49}$$

with

$$\begin{aligned} \vec{k}_1 &= k\sin\theta\,\hat{x} + k\cos\theta\,\hat{z}, \\ \vec{k}_2 &= -k\sin\theta\,\hat{x} + k\cos\theta\,\hat{z}, \\ \vec{r} &= x\hat{x} + z\hat{z}, \end{aligned} \tag{50}$$

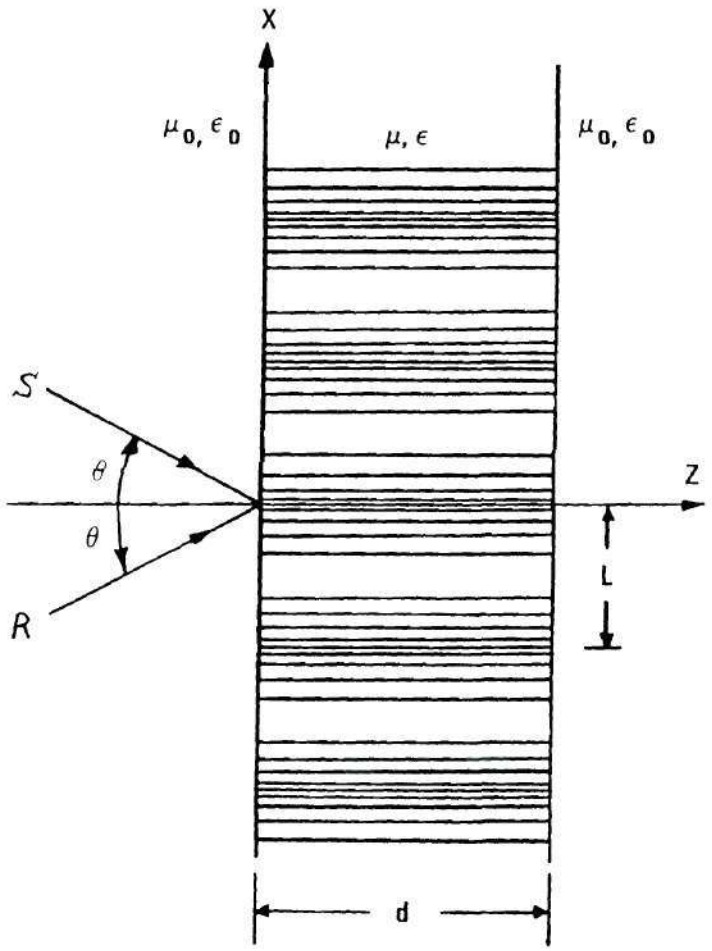

Figure 3. Geometry for Holographic Recording.

where $\vec{E}_1$ and $\vec{E}_2$ are the electric field vectors of the incident waves, ω is the angular frequency, $k = 2\pi/\lambda$, and $\hat{x}$ and $\hat{z}$ are unit vectors. The total electric field inside the medium is

$$\vec{E} = \vec{R} + \vec{S}$$

$$= \vec{E}_1 \exp\left[j(\vec{k}_1 \cdot \vec{r} - \omega t)\right] + \vec{E}_2 \exp\left[j(\vec{k}_2 \cdot \vec{r} - \omega t)\right]$$

$$= \vec{E}_1 \exp\left[j(kx \sin\theta + kz \cos\theta - \omega t)\right] + \vec{E}_2 \exp\left[j(-kx \sin\theta + kz \cos\theta - \omega t)\right]. \quad (51)$$

Therefore, the total intensity (watt/m^2) inside the medium is

$$I = \frac{1}{2}(\varepsilon/\mu)^{\frac{1}{2}} \vec{E} \cdot \vec{E}^*$$

$$= \frac{1}{2}(\varepsilon/\mu)^{\frac{1}{2}} \left[\vec{E}_1 \cdot \vec{E}_1 + \vec{E}_2 \cdot \vec{E}_2 + 2\, \vec{E}_1 \cdot \vec{E}_2 \cos(2kx \sin\theta)\right]$$

$$= I_1 + I_2 + (\varepsilon/\mu)^{\frac{1}{2}} \vec{E}_1 \cdot \vec{E}_2 \cos(2kx \sin\theta), \quad (52)$$

where ε is the permittivity of the medium, μ is the permeability of the medium, $I_1 = (1/2)(\varepsilon/\mu)^{\frac{1}{2}} \vec{E}_1 \cdot \vec{E}_1$, and $I_2 = (1/2)(\varepsilon/\mu)^{\frac{1}{2}} \vec{E}_2 \cdot \vec{E}_2$. Thus the intensity at any point in the interference pattern formed by the two waves is the sum of the intensities of the individual waves plus an interference term. By using the Bragg condition, $\lambda = 2L \sin\theta$, and $K = 2\pi/L$, Eq. (52) can be rewritten as

$$I = I_o (1 + m \cos Kx), \quad (53)$$

where $I_o = I_1 + I_2$ and the modulation ratio, m, is defined as

$$m = (\epsilon/\mu)^{\frac{1}{2}}(\vec{E}_1 \cdot \vec{E}_2)/I_o. \qquad (54)$$

The value of m is greater than -1 but smaller than +1. It becomes zero when the two incident (writing) beams are polarized in mutually perpendicular directions. Equation (53) is the general expression for the interference pattern formed by the two writing beams.

3.2.2 Basic Equations

Staebler and Amodei[49] have shown for lithium niobate that the electric field patterns, which cause the spatial variation of the refractive index, are generated through both diffusion and drift of photogenerated free electrons (as opposed to holes). Thus the charge carriers will be assumed to be electrons. Assuming that the concentration of the trapped electrons is sufficiently large so that its variation due to migration is negligibly small and that the generation rate and trapping time are essentially unchanged during recording, then the concentration of the free electrons excited to the conduction band is given by[28]

$$n_f(x) = \tau g_o(1 + m \cos Kx), \qquad (55)$$

where τ is the lifetime of photoexcited electrons and g_o, the photoelectron generation rate, is given by[28]

$$g_o = I_o \alpha/hf, \qquad (56)$$

where α is the optical absorption coefficient, h is Planck's constant, and f is the light frequency. For an isotropic material (or if the x

direction is along one of the crystallographic axes for anisotropic materials), the spatial distribution of the current density at any time is given by

$$J(x,t) = eD_n \frac{dn_f}{dx} + e\,\mu_n n_f \left[E_o' + E_{sc}(x,t)\right] + \kappa_1 \alpha I, \qquad (57)$$

where e is the magnitude of the electronic charge, D_n is the diffusion coefficient for electrons, μ_n is the mobility for electrons, E_o' is the externally applied electric field (if any), $E_{sc}(x,t)$ is the space-charge field, and κ_1 is a constant depending on the nature of the absorption center and wavelength.[27] The third term on the right hand side of Eq. (57) represents the photovoltaic effect.[27] Using Eqs. (53), (55), and (56), Eq. (57) can be rewritten as

$$J(x,t) = eD_n \frac{dn_f}{dx} + e\,\mu_n n_f \left[E_o + E_{sc}(x,t)\right], \qquad (58)$$

where

$$E_o = E_o' + \kappa_1 \alpha h f/(e\mu_n \tau g_o). \qquad (59)$$

The last term in Eq. (59) may be regarded as an effective electric field due to the photovoltaic effect. Using the Einstein relation, $\mu_n/D_n = e/k_bT$, where k_b is the Boltzmann constant and T is the absclute temperature, the current density, Eq. (58), can be rewritten as

$$J(x,t) = e\mu_n \left\{ \frac{k_bT}{e} \frac{dn_f}{dx} + n_f \left[E_o + E_{sc}(x,t)\right] \right\}. \qquad (60)$$

The accumulation rate of the space-charge density, ρ, at any point and at any time is given by the one-dimensional continuity equation,

$$\frac{\partial \rho(x,t)}{\partial t} = - \frac{\partial J(x,t)}{\partial x}. \tag{61}$$

Combining this with Poisson's equation gives

$$\frac{\partial E_{sc}(x,t)}{\partial x} = \frac{\rho(x,t)}{\varepsilon} = - \frac{1}{\varepsilon} \int_0^t \frac{\partial J(x,t')}{\partial x} \, dt'. \tag{62}$$

3.3 Solutions of the Equations

Equations (60), (61), and (62) have recently been solved by Alphonse et al.[47] and by Cornish et al.[48] using analytic methods. Their solutions are not identical because they have used different boundary conditions. Here, a numerical approach is employed to solve for $E_{sc}(x,t)$ over the entire range of holographic recording. This can reveal the behavior of $E_{sc}(x,t)$ for all stages of holographic recording. The total space-charge field is $E_{sc}(x,t) = E'_{sc}(x,t) + E''_{sc}(x,t)$, where $E'_{sc}(x,t)$ and $E''_{sc}(x,t)$ are the space-charge fields due to diffusion and drift, respectively. In order to obtain a better insight into the relative importance of diffusion and drift, these two mechanisms are considered separately before their combination is considered.

3.3.1 Diffusion Only

In this case, $E_o = 0$ and $E_{sc}(x,t) = E'_{sc}(x,t)$, therefore Eq. (60) becomes

$$J(x,t) = - e\mu_n \tau g_o \left[-(k_b T/e) mK \sin Kx + (1 + m \cos Kx) E'_{sc}(x,t) \right]. \tag{63}$$

The exposure time t is set equal to $p\Delta t$, where p is any positive integer and Δt is an increment of the exposure time that is sufficiently small so that the variation of dJ/dx is negligible over the time interval Δt. Then, Eq. (62) reduces to a difference-differential equation,

$$\frac{dE_{sc}[x,p\Delta t]}{dx} = \frac{dE_{sc}[x,(p-1)\Delta t]}{dx} - \frac{1}{\epsilon}\frac{dJ[x,(p-1)\Delta t]}{dx}\Delta t. \qquad (64)$$

Substituting Eq. (63) into Eq. (64) with E_{sc} replaced by E'_{sc}, we obtain

$$\frac{dE'_{sc}[x,p\Delta t]}{dx} = \frac{dE'_{sc}[x,(p-1)\Delta t]}{dx} + (e\mu_n \tau g_o/\epsilon)\Big\{(k_b T/e)mK^2 \cos Kx$$

$$- (1 + m \cos Kx)\frac{dE'_{sc}[x,(p-1)\Delta t]}{dx} + mK \sin(Kx)\, E'_{sc}[x,(p-1)\Delta t]\Big\}\Delta t. \qquad (65)$$

From Eq. (65), together with the boundary condition $E'_{sc}(0,t) = 0$ and the initial condition $dE'_{sc}(x,0)/dx = 0$, the space-charge field, $E'_{sc}(x,t)$, can be obtained by numerical integration.

3.3.2 Drift Only

In this case, there is a uniform dc field that is sufficiently large so that the diffusion component of the current can be neglected compared with the drift component. Therefore, Eq. (60) becomes

$$J(x,t) = e\mu_n \tau g_o(1 + m \cos Kx)\left[E_o + E''_{sc}(x,t)\right]. \qquad (66)$$

Letting the exposure time t be equal to $p\Delta t$ and substituting Eq. (66) into Eq. (64) with E_{sc} replaced by E''_{sc}, gives

$$\frac{dE''_{sc}[x,p\Delta t]}{dx} = \frac{dE''_{sc}[x,(p-1)\Delta t]}{dx} + (e\mu_n \tau g_o)\Big(mK \sin(Kx)\{E_o + E''_{sc}[x,(p-1)\Delta t]\}$$

$$- (1 + m \cos Kx) \frac{dE''_{sc}[x,(p-1)\Delta t]}{dx}\Big) \Delta t. \qquad (67)$$

Equation (67) is the difference-differential equation for drift. It can also be solved numerically, provided that the boundary and the initial conditions are specified.

3.3.3 Diffusion and Drift

When the electric field, E_o (externally applied field plus effective photovoltaic field), is small such that both the diffusion and drift components are present, Eq. (57) becomes

$$J(x,t) = e\mu_n \tau g_o \{-(k_b T/e)mK \sin Kx + (1 + m \cos Kx)[E_o + E_{sc}(x,t)]\}. \qquad (68)$$

Inserting Eq. (68) into Eq. (64), we obtain

$$\frac{dE_{sc}(x,p\Delta t)}{dx} = \frac{dE_{sc}[x,(p-1)\Delta t]}{dx} + (e\mu_n \tau g_o/\varepsilon)\Big((k_b T/e)mK^2 \cos Kx$$

$$+ mK \sin(Kx)\{E_o + E_{sc}[x,(p-1)\Delta t]\}$$

$$- (1 + m \cos Kx) \frac{dE_{sc}[x,(p-1)\Delta t]}{dx}\Big) \Delta t. \qquad (69)$$

Equation (69) is the difference-differential equation for diffusion and drift. It can also be obtained by adding Eqs. (65) and (67) and using $E_{sc} = E'_{sc} + E''_{sc}$. That is, the total space-charge field is the super-

position of the space-charge fields due to diffusion and drift. Usually, when the electric field E_o is several hundred thousand volts per meter, the space-charge field due to diffusion is very small compared with the space-charge field due to drift.

3.4 Numerical Results

Equations (65), (67), and (69) were numerically solved by use of the Runge-Kutta method. As can be seen from these equations the controlling material parameter is $\mu_n \tau g_o/\varepsilon$. The low frequency permittivity ε is known for most ferroelectrics as a function of temperature and crystallographic direction. For lithium niobate at room temperature, a typical value is $\varepsilon = 30\varepsilon_o$, where ε_o is the permittivity of free space. Values for the parameters μ_n and τ are not accurately known. Photoconductivity data for doped lithium niobate[27] imply that the product $\mu_n\tau \simeq 10^{-13}$ m^2/volt (using $e\mu_n\tau\alpha/hf = 1.4 \times 10^{-10}$ m/volt^2 and $\alpha = 3.8 \times 10^3$ m^{-1} from Ref. 27). The generation rate g_o can vary over an extremely wide range depending on the doping and treatment of the sample as well as on the intensity of the laser beams. A typical value of $g_o = 6 \times 10^{22}$ $m^{-3}sec^{-1}$ is chosen here and thus $\mu_n\tau g_o = 6 \times 10^8$ $V^{-1}m^{-1}sec^{-1}$ in this work. The exposure time increment Δt was 1 sec. The space-charge field distribution for diffusion is shown in Fig. 4. Figure 4 shows that for the initial stage of hologram formation (after one second exposure time in this case), the field distribution is sinusoidal. As the exposure increases, the amplitude of the space-charge field increases and the field distribution becomes nonsinusoidal, and the positions at which the field extrema occur are shifted. However, the field pattern

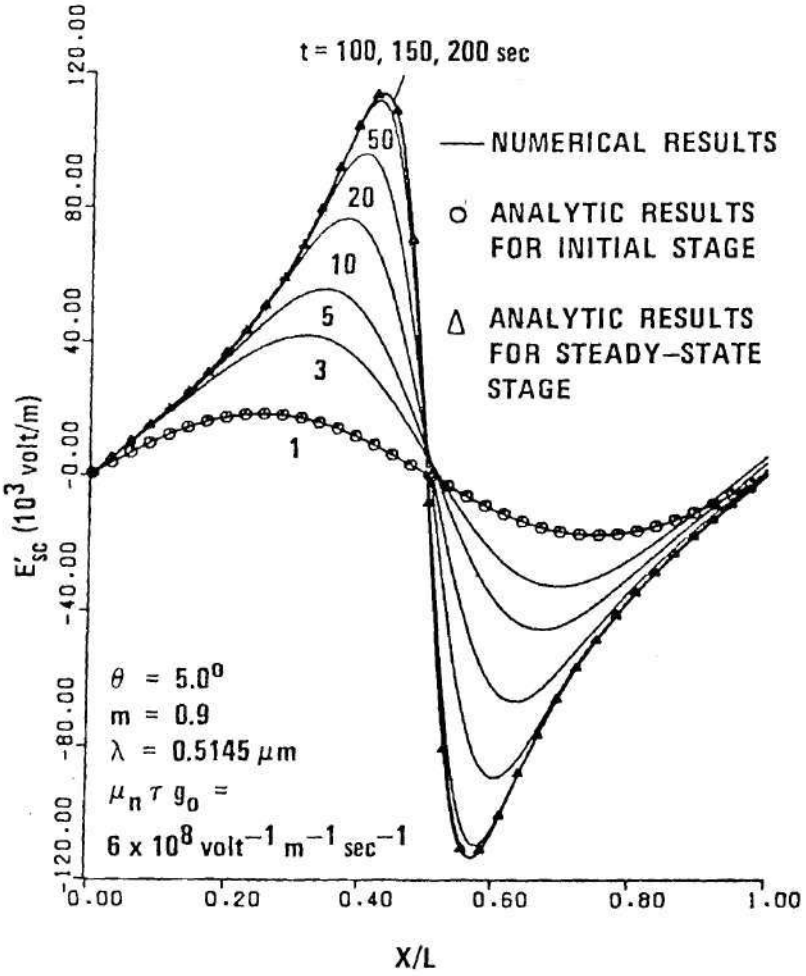

Figure 4. One Grating Period of the Calculated Space-charge Field, $E'_{sc}(x,t)$, produced by diffusion.

retains odd symmetry at all stages of hologram formation. When the steady-state stage of hologram formation is reached (after about 100 sec exposure), the amplitude and the distribution of the space-charge field pattern remain fixed and do not change with further exposure. For comparison, the results of the analytic solutions for the initial and the final steady-state stages of hologram formation are also shown in Fig. 4. The circles in Fig. 4 represent the results for the initial stage of hologram formation as obtained from the amalytical expression[28]

$$E'_{sc}(x,t) = (1/\varepsilon)\ k_b T\ \mu_n \tau\ g_o\ mKt \sin Kx, \qquad (70)$$

evaluated for an exposure time of one second with $\mu_n \tau\, g_o = 6 \times 10^8\ V^{-1}\ m^{-1} sec^{-1}$. The triangles in Fig. 4 represent the results for the steady-state stage of hologram formation as obtained from the analytical expression[28]

$$E'_{sc}(x) = (k_b T/e)\ (mK \sin Kx)/(1 + m \cos Kx), \qquad (71)$$

evaluated at room temperature. The comparison shows that the numerical results correctly reduce to Amodei's results[28] for the limiting cases. In addition, the limits of validity for Eqs. (70) and (71) are established by the numerical approach in terms of exposure and material parameters. For example, from Fig. 4, it is seen that Eq. (70) is valid when $t \leq 1$ sec and that Eq. (71) is valid when t is near or greater than 100 sec for the parameters used here. Figure 5 presents the behavior of the amplitude of the space-charge field as a function of exposure. The

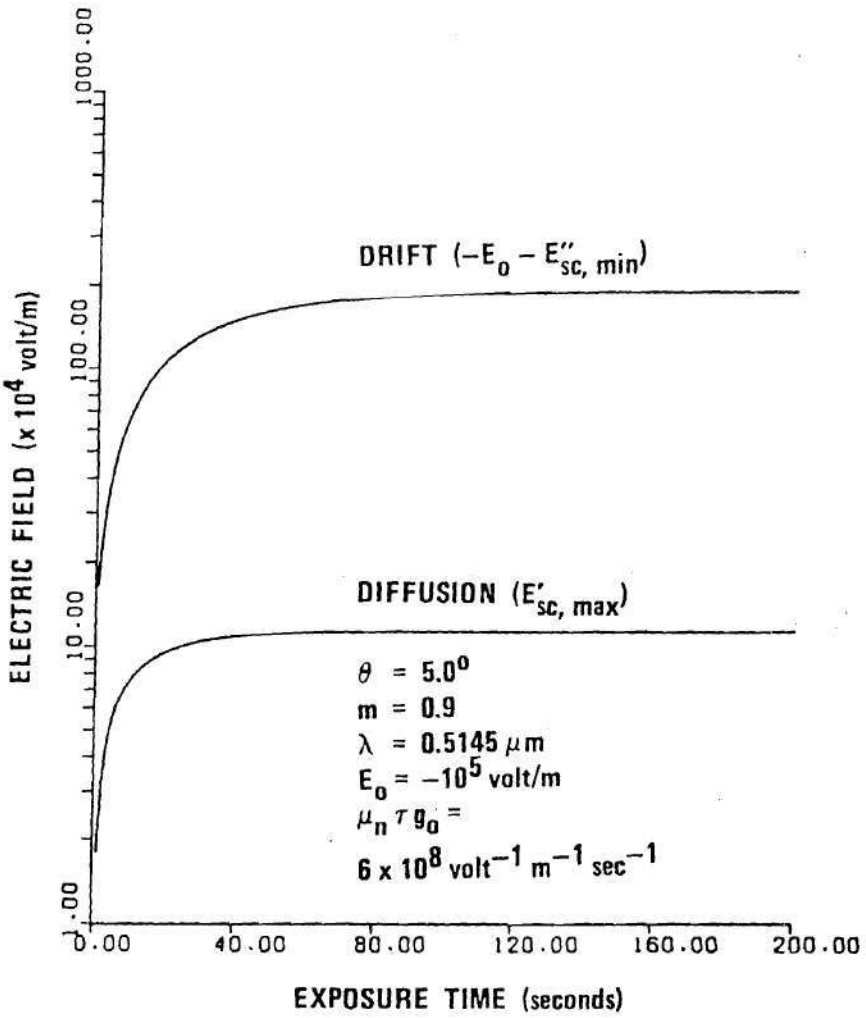

Figure 5. Calculated Values of the Space-charge Field Amplitude Produced by Diffusion and by Drift as a Function of Exposure Time.

amplitude increases rapidly in the early stages of hologram formation. For $\mu_n \tau g_o = 6 \times 10^8\ V^{-1}m^{-1}sec^{-1}$, the amplitude begins to saturate near 40 sec of exposure and finally remains unchanged after about 100 sec of exposure. Since the value of g_o is proportional to I_o as given by Eq. (56), the limits of validity of Eqs. (70) and (71) depend on I_o for a given set of material parameters. Larger values of I_o result in larger values of g_o and, therefore, shorter exposure times are needed to reach any given exposure. In other words, the amplitude of the field saturates more rapidly for larger values of g_o. Equation (70), for the case of the initial stage of hologram formation, is valid as long as the space-charge field is negligible in the transport equation. Strictly speaking, the space-charge field can not be neglected at any time except at the very beginning of hologram formation. In the numerical approach, the space-charge field is neglected in the transport equation only for an exposure time of Δt in duration from the beginning of hologram formation. In the calculation of the results here, Δt was chosen to be one second. In fact, other values of Δt can be used, provided that the values of Δt are small enough to insure that there is no appreciable variation in dJ/dx over the time interval Δt. In addition to $\Delta t = 1.0$ sec, the calculations have been performed with $\Delta t = 0.5$ sec and the same resultant electric field patterns are obtained. In general, in order to maintain the same level of numerical accuracy, a smaller value of Δt must be used for a larger value of g_o for given material parameters, writing angle, and beam modulation ratio. Figures 6 and 7 present the field patterns due to diffusion for various values of the beam modulation ratio, m, in

the steady-state stage of hologram formation with writing angles of 5.0° and 25.0°, respectively. We see that the field pattern changes as the beam modulation ratio changes. The space-charge field amplitude as a function of the beam modulation ratio for the steady-state case is shown in Fig. 8. The squares in Fig. 8 represent the numerical results while the solid curve represents the analytic results. The field amplitude increases as the beam modulation ratio increases. This is true for all stages of hologram formation though only the steady-state case is shown in Fig.8. From Figs. 6 and 7, we see that the field patterns in Fig. 6 are the same as those in Fig. 7 except that the scales for the field amplitudes are different. In other words, the change of writing angle from 5.0° to 25.0° does not change the field patterns but the field amplitudes. A more detailed illustration of this property is shown in Fig. 9, which presents the steady-state field patterns for various writing angles with the beam modulation ratio m equal to 0.9. From Figs. 4, 6, 7, and 9, we observed that the space-charge field pattern due to diffusion has odd symmetry at all times. The amplitude of the space-charge field as a function of writing angle in the steady-state stage of hologram formation is plotted in Fig. 10. Again, the results of the numerical and analytic methods are represented by the squares and the solid curve, respectively. The field amplitude increases as writing angle increases (grating period decreases). This is also true for all other stages of hologram formation.

In the case of drift, the electric field at the boundary is not zero. It depends on the charge density at the surface and the applied voltage across the sample. The electric field at the boundary is assumed

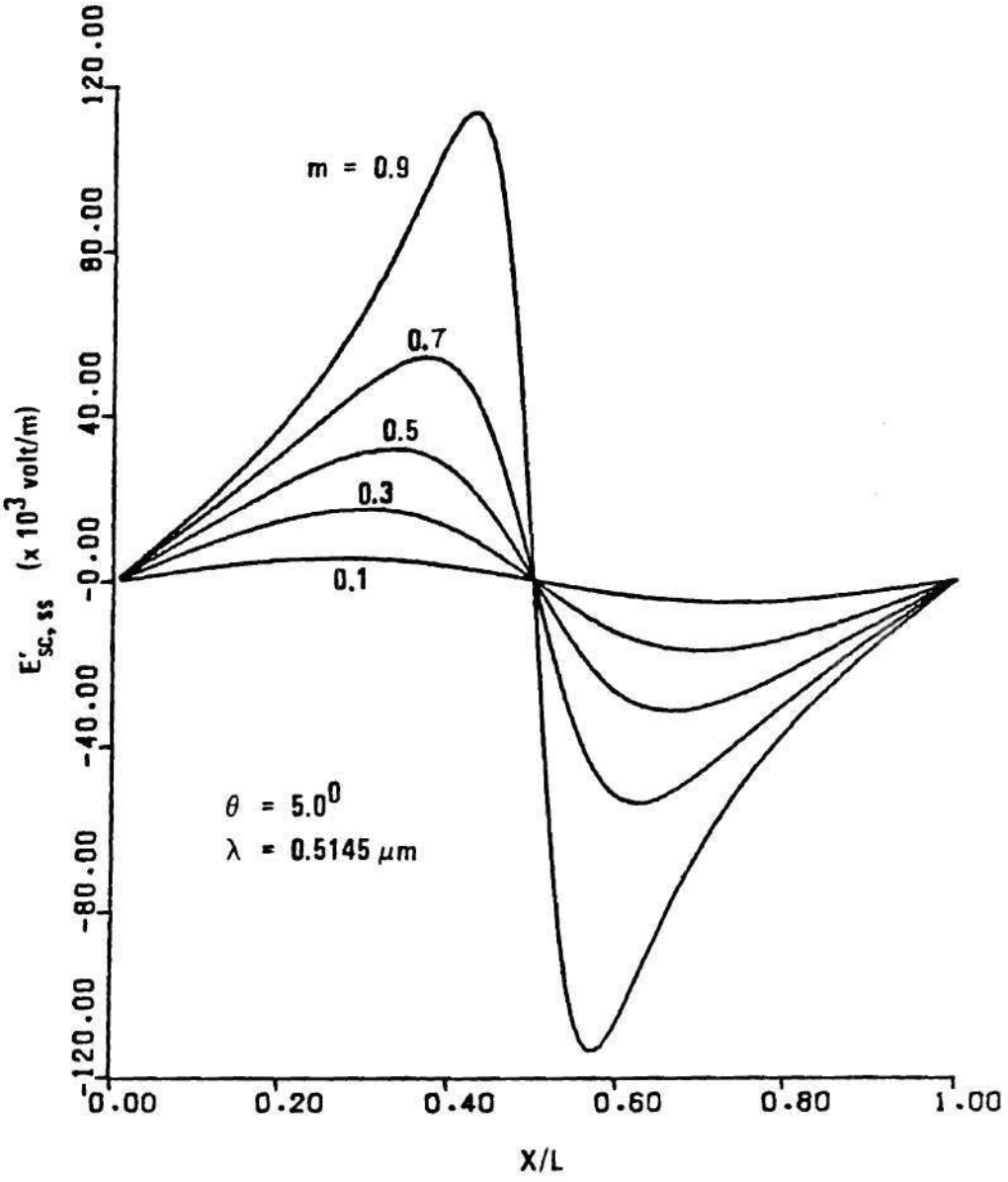

Figure 6. One Grating Period of the Calculated Steady-state Space-charge Field, $E'_{sc}(x)$, Produced by Diffusion for Various Values of the Beam Modulation Ratio, m.

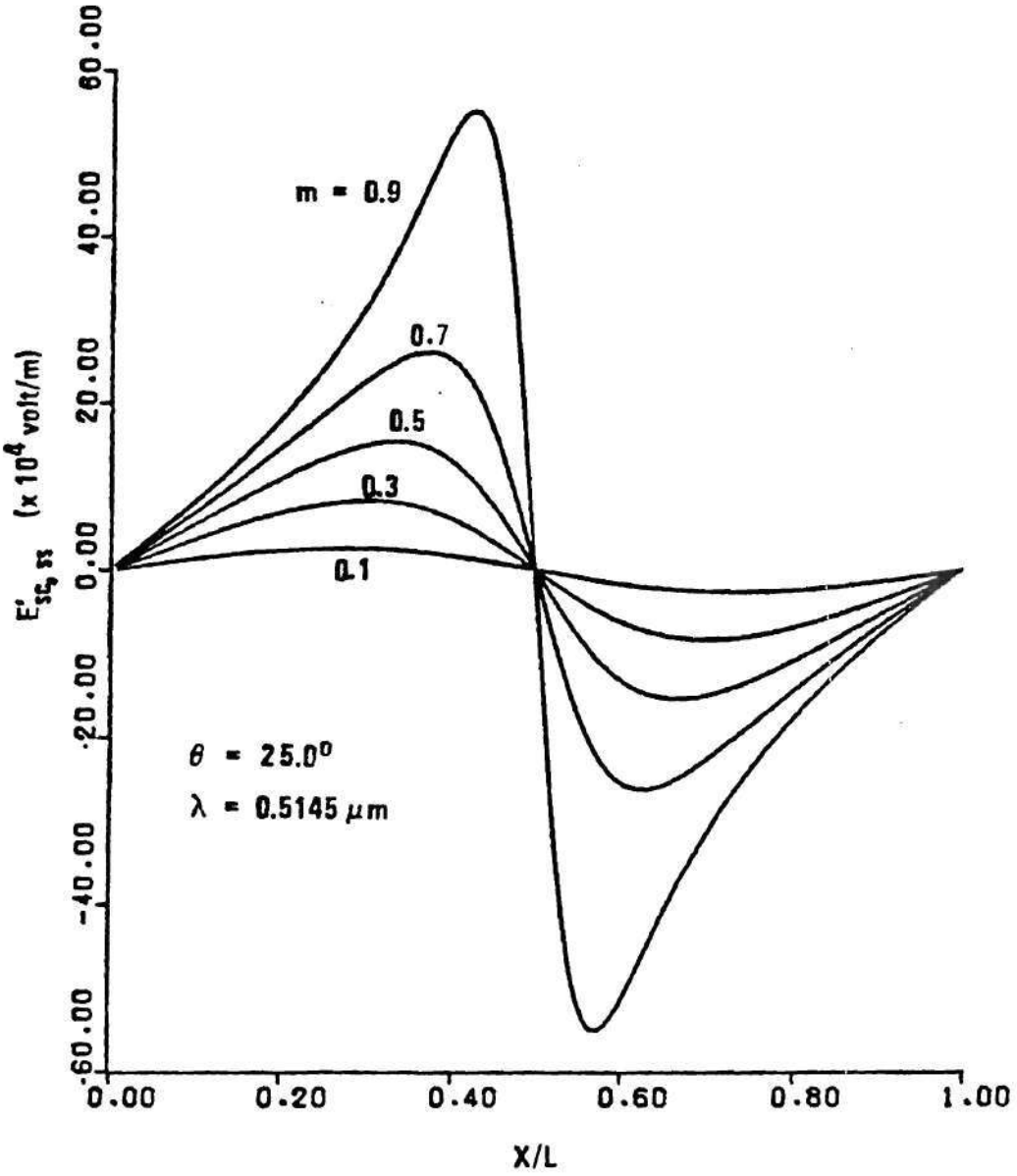

Figure 7. Same as Fig. 6 but for a Writing Angle of 25.0°.

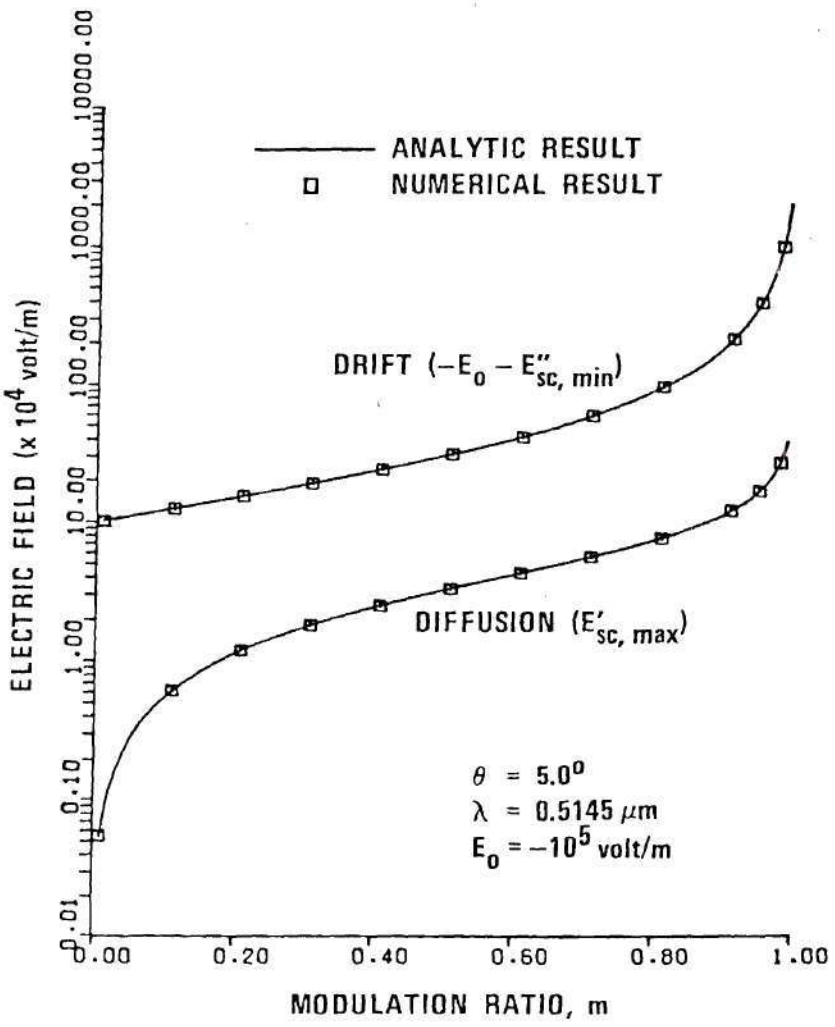

Figure 8. Calculated Steady-state Final Amplitude of the Space-charge Field Produced by Diffusion and by Drift as a Function of Beam Modulation Ratio.

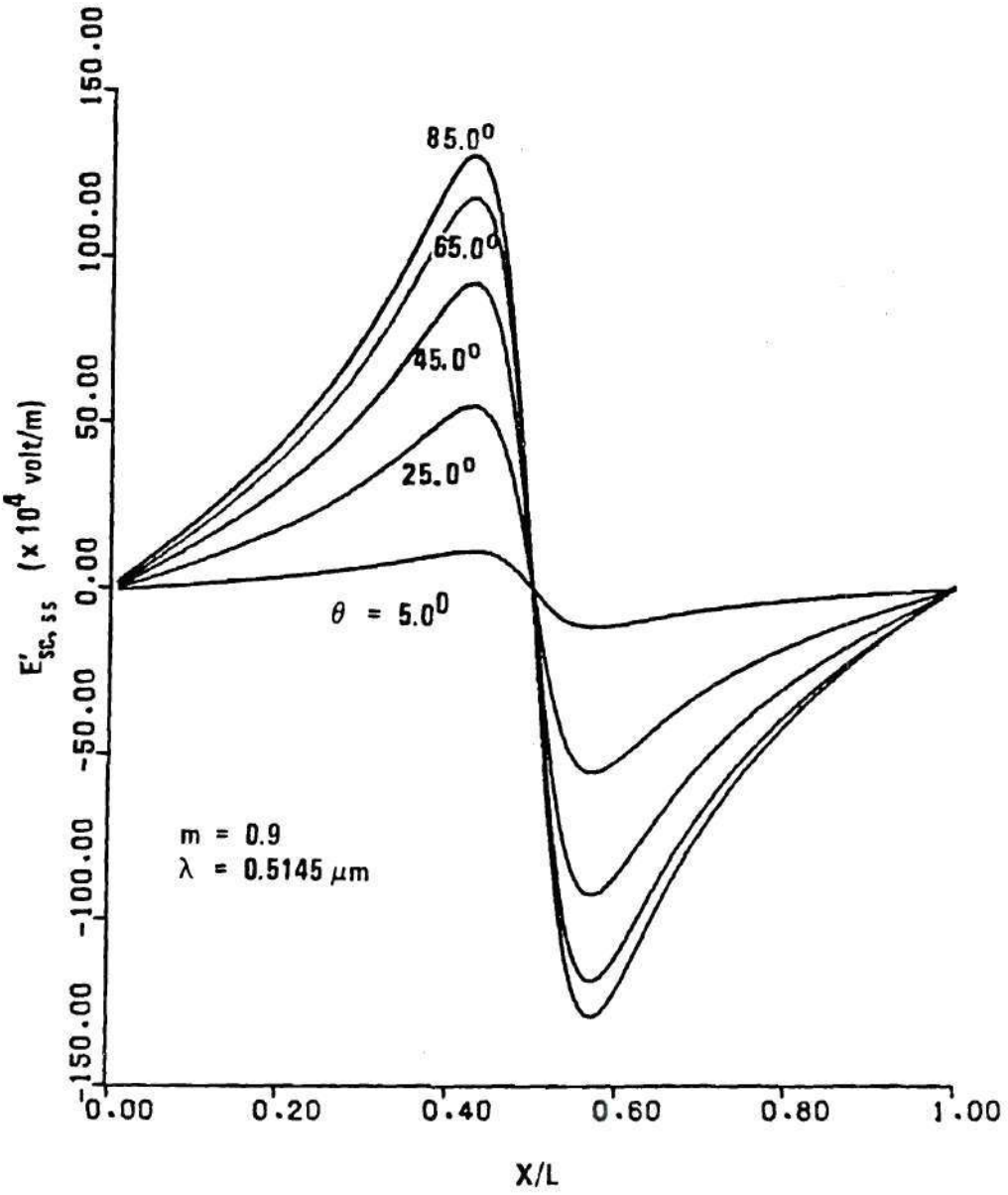

Figure 9. One Grating Period of the Calculated Steady-state Space-charge Field, $E'_{sc}(x)$, Produced by Diffusion for Various Writing Angles.

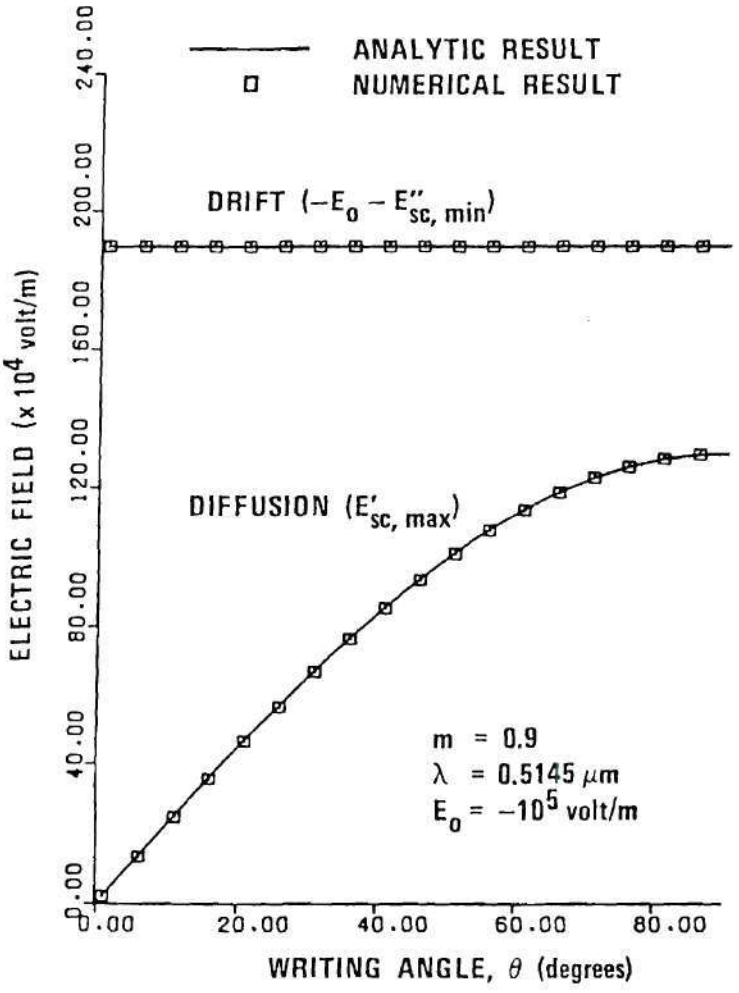

Figure 10. Calculated Steady-state Final Amplitude of the Space-charge Field Produced by Diffusion and by Drift as a Function of Writing Angle.

to be equal to the dc field E_o at all times. The shape of the electric field pattern produced is independent of the value of the dc field E_o. The amplitude of the pattern, however, is dependent upon E_o, increasing with increasing E_o. The initial condition for drift is $\partial E''_{sc}(x,0)/\partial x = 0$. Figure 11 shows the total electric field distribution when drift is dominant. The dc field E_o is assumed to be -1.0×10^5 V/m. As for the diffusion case, the field distribution is sinusoidal at the initial stage of hologram formation. As exposure increases, the amplitude increases and the field distribution becomes nonsinusoidal and sharply peaked. However, the positions at which the field extrema occur do not shift with exposure. In addition, the field pattern has even symmetry at all times. Also shown in Fig. 11 are the analytic solutions for the electric field distribution at the initial and the steady-state stages of hologram formation. The same value for the electric field at the boundary has been used in these analytic solutions. The circles in Fig. 11 represent the results of the initial stage solution (proportional to cos Kx). The triangles represent the steady-state solution [proportional to $(1 + m)/(1 + m \cos Kx)$]. The numerical results again correctly reduce to the analytic solutions. From Fig. 11, it is observed that, for $\mu_n \tau g_o = 6 \times 10^8$ $V^{-1}m^{-1}sec^{-1}$, the analytic solutions are valid when t is equal to or less than one second for the initial stage of hologram recording and when t is near or greater than 150 sec for the steady-state case. The behavior of the drift electric field amplitude as a function of exposure is also plotted in Fig. 5. The saturation time is about 150 sec for $\mu_n \tau g_o = 6 \times 10^8$ $V^{-1}m^{-1}sec^{-1}$, which is somewhat longer than that for the diffusion case. As counterparts of Figs. 6 and 7, Figs. 12

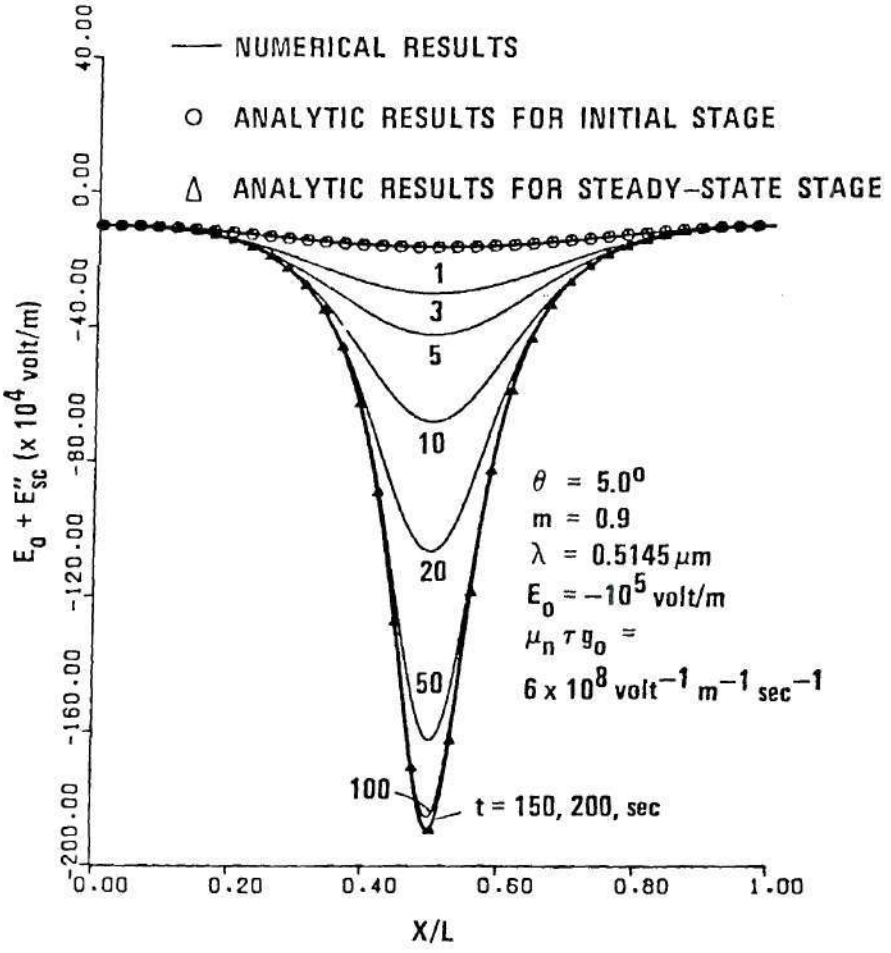

Figure 11. One Grating Period of the Calculated Total Electric Field, $E(x,t) = E_o + E''_{sc}(x,t)$, Produced by Drift.

and 13 present the steady-state electric field patterns due to drift for different values of beam modulation ratio at writing angles of 5.0° and 25.0°, respectively. As for the diffusion case, the absolute value of the amplitude increases as the beam modulation ratio increases. This can also be seen from Fig. 8, which presents the field amplitude as a function of the beam modulation ratio. A comparison of Figs. 12 and 13 shows that they are identical. This means that the change of writing angle from 5.0° to 25.0° does not change either the field pattern or the field amplitude. The steady-state electric field amplitude due to drift as a function of writing is also plotted in Fig. 10. It is observed that the field amplitude does not change with the writing angle (and therefore grating period). This is also true for all other stages of hologram formation as well.

We have examined the results of the cases of diffusion and drift, respectively. Now we turn to the case in which both diffusion and drift are present. Figures 14 through 16 present the electric field patterns due to both diffusion and drift for different values of the dc field E_o. When the dc electric field E_o is small (see Fig. 14), the field pattern is similar to that due to diffusion. As the magnitude of E_o increases, the contribution of the drift component increases and the field pattern is no longer similar to that due to diffusion. When the dc field E_o is large (see Fig. 16), the diffusion component is negligible compared to the drift component, and the field pattern is similar to that due to drift. This can be seen by comparing Figs. 16 and 11. The amplitude of the electric field for a combination of diffusion and drift as a function of exposure is plotted in Fig. 17. Figures 18 and 19 present

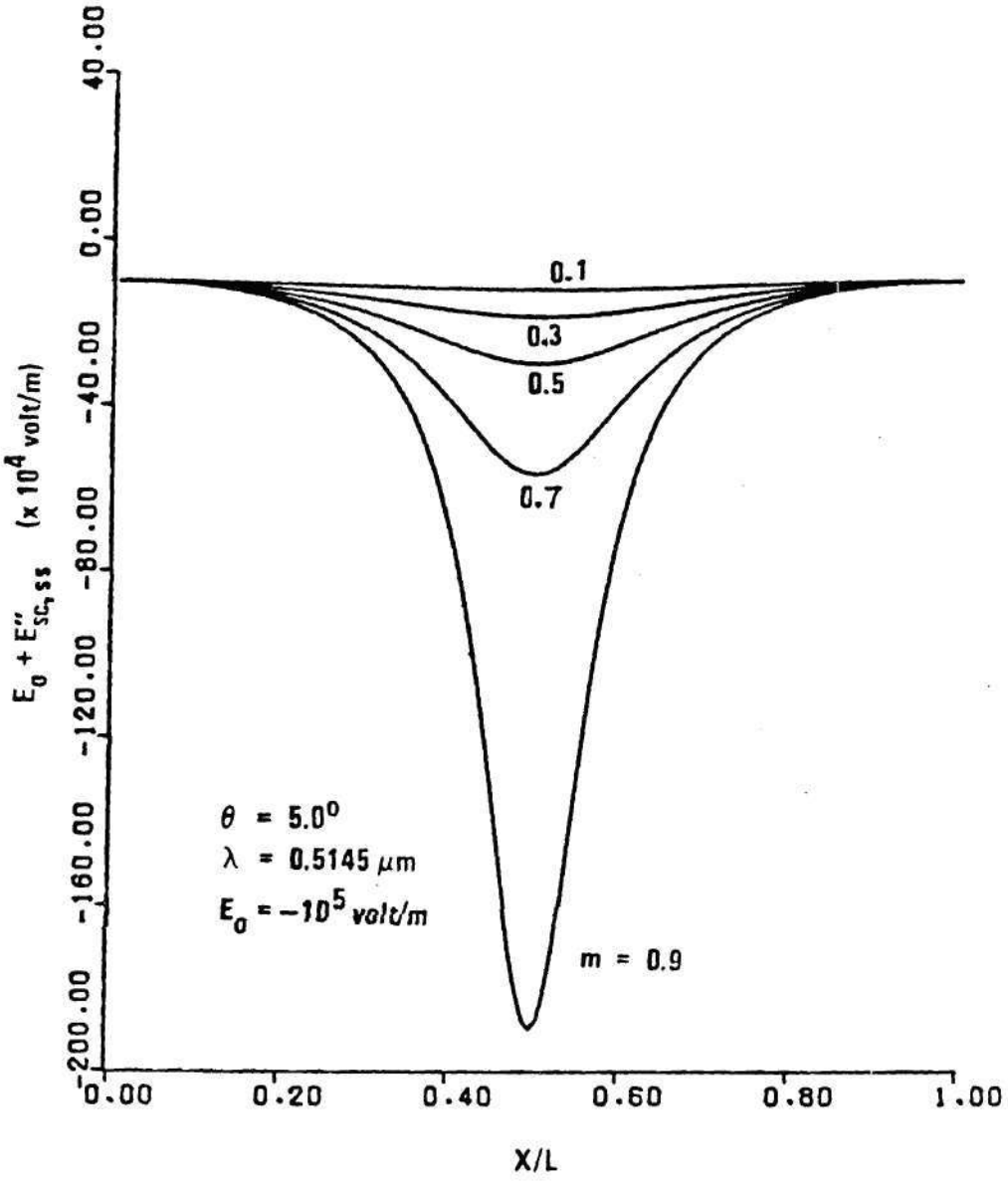

Figure 12. One Grating Period of the Steady-state Total Electric Field, $E(x) = E_o + E''_{sc}(x)$, Produced by Drift for Various Values of Beam Modulation Ratio.

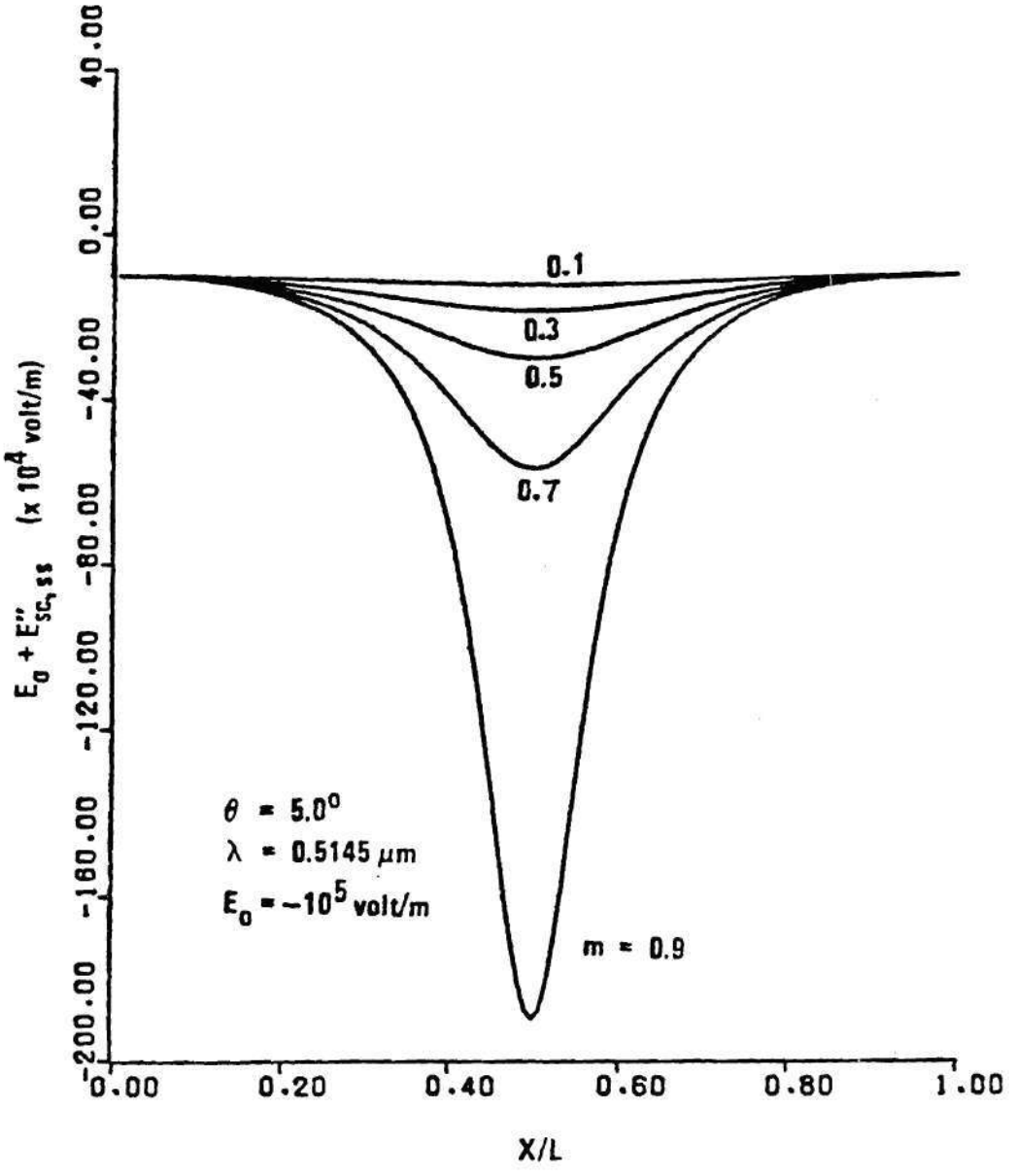

Figure 13. Same as Fig. 12 but for a Writing Angle of 25.0°.

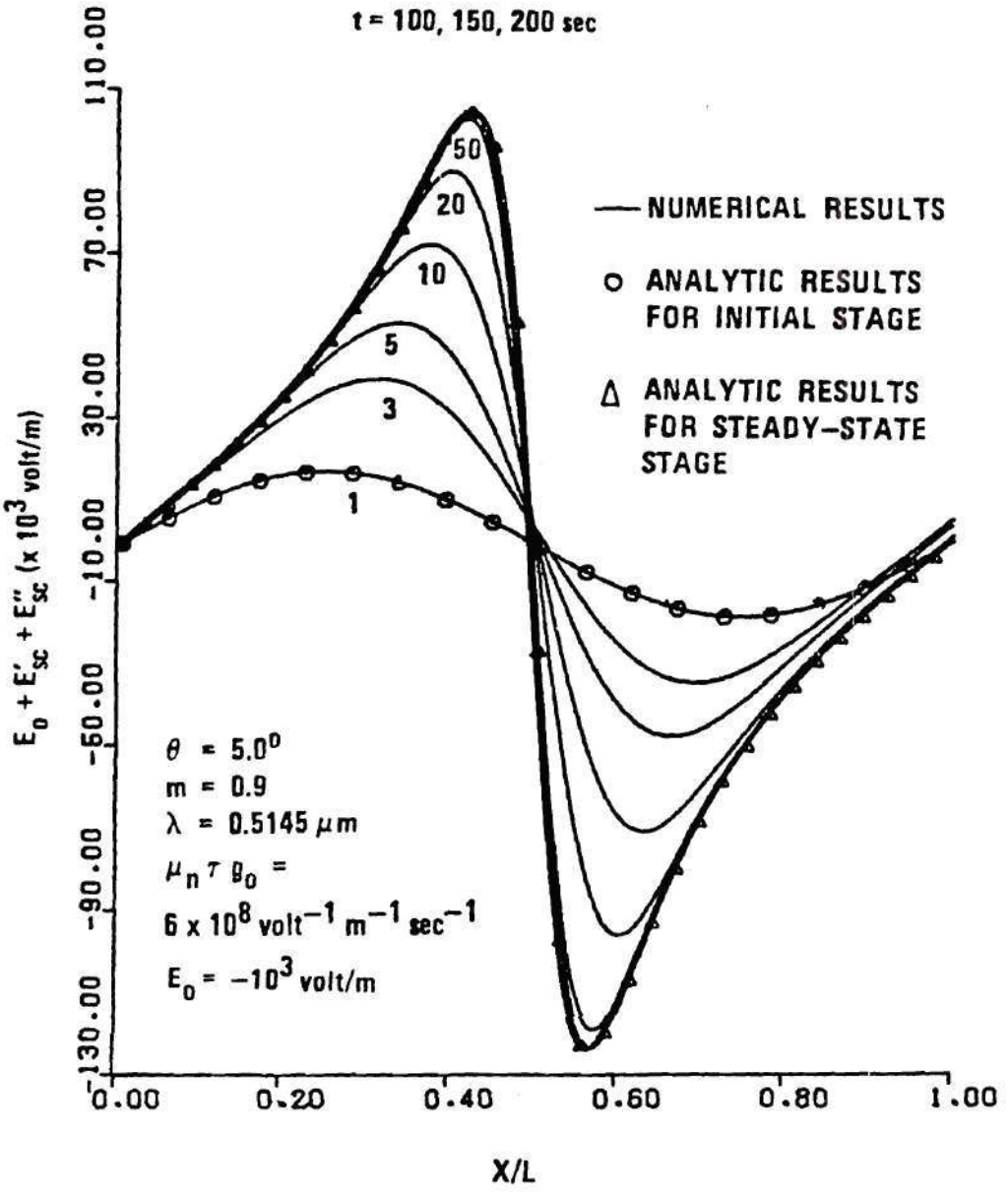

Figure 14. One Grating Period of the Calculated Total Electric Field Produced by a Combination of Diffusion and Drift.

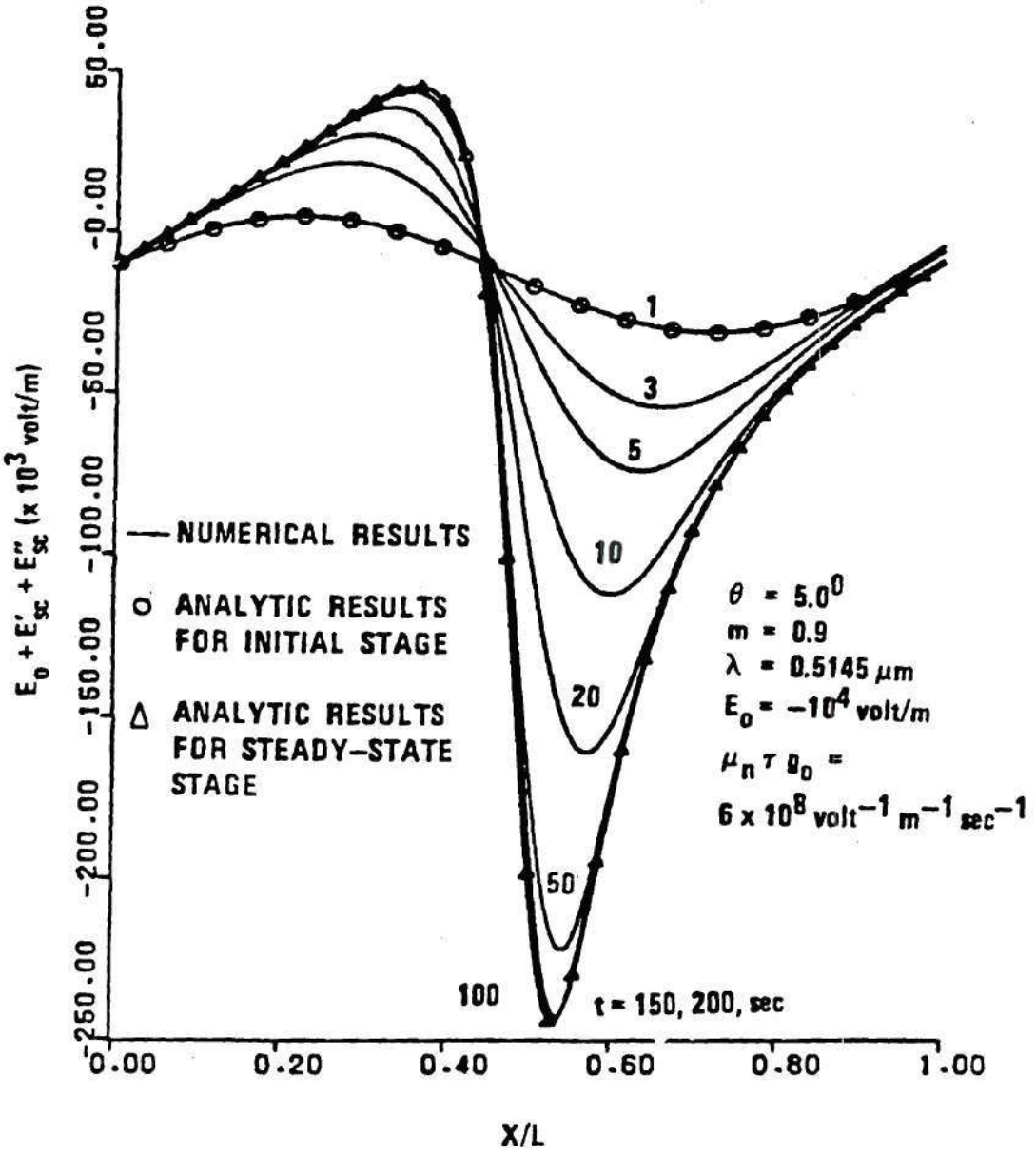

Figure 15. Same as Fig. 14 but with a dc Field of -10^4 V/m.

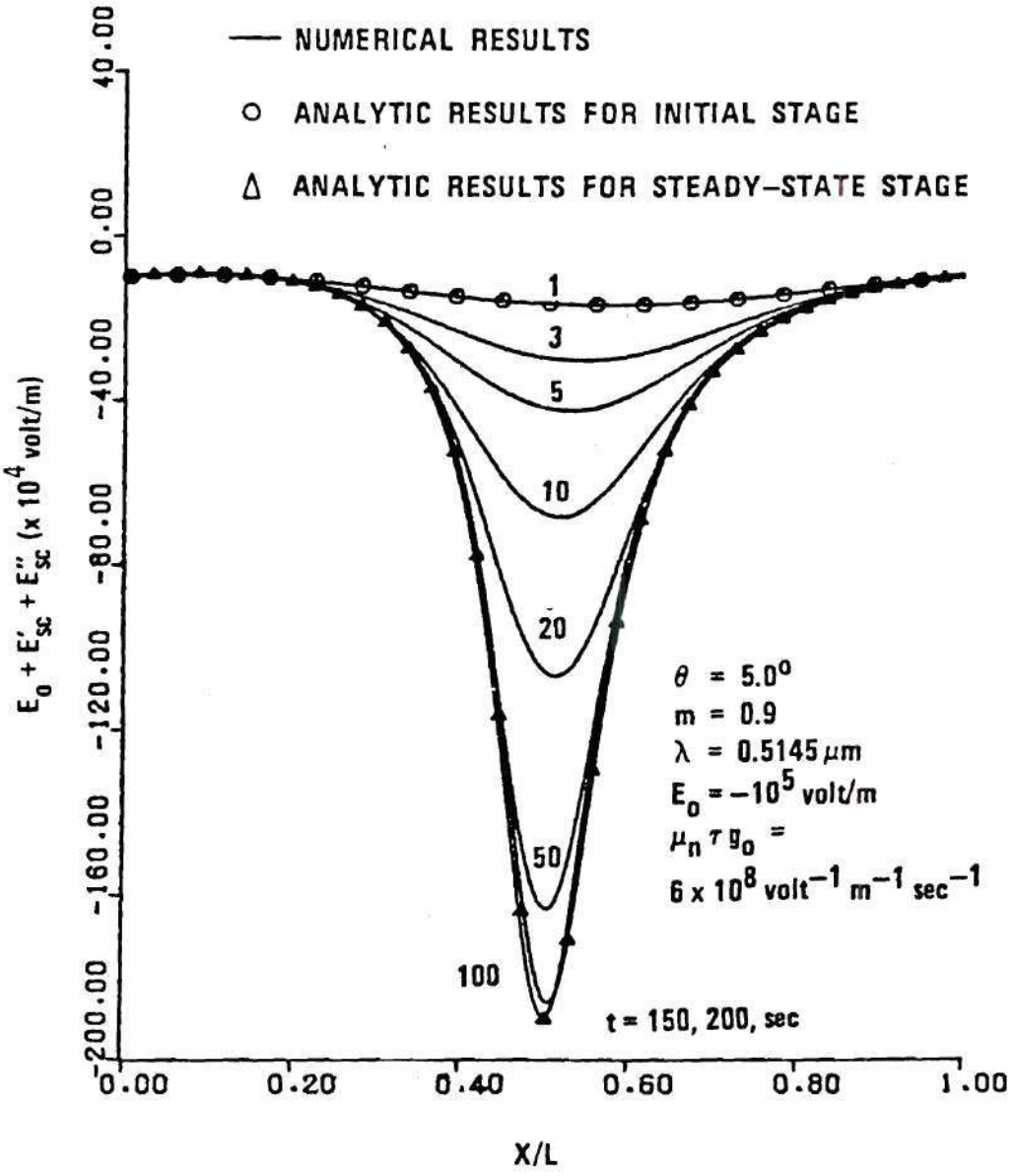

Figure 16. Same as Fig. 14 but with a dc Field of -10^5 V/m.

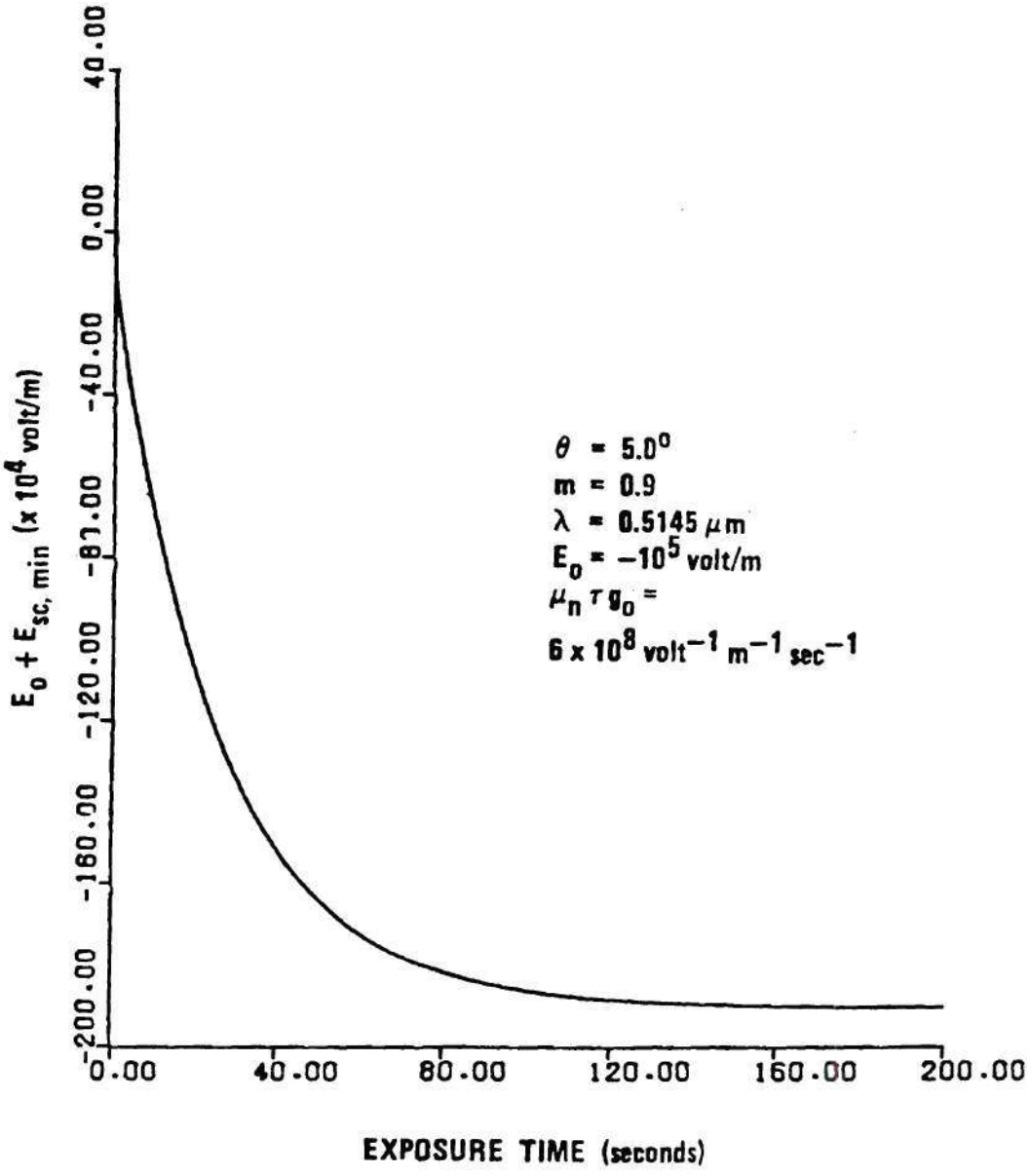

Figure 17. Calculated Value of the Total Electric Field Amplitude Produced by a Combination of Diffusion and Drift as a Function of Exposure Time.

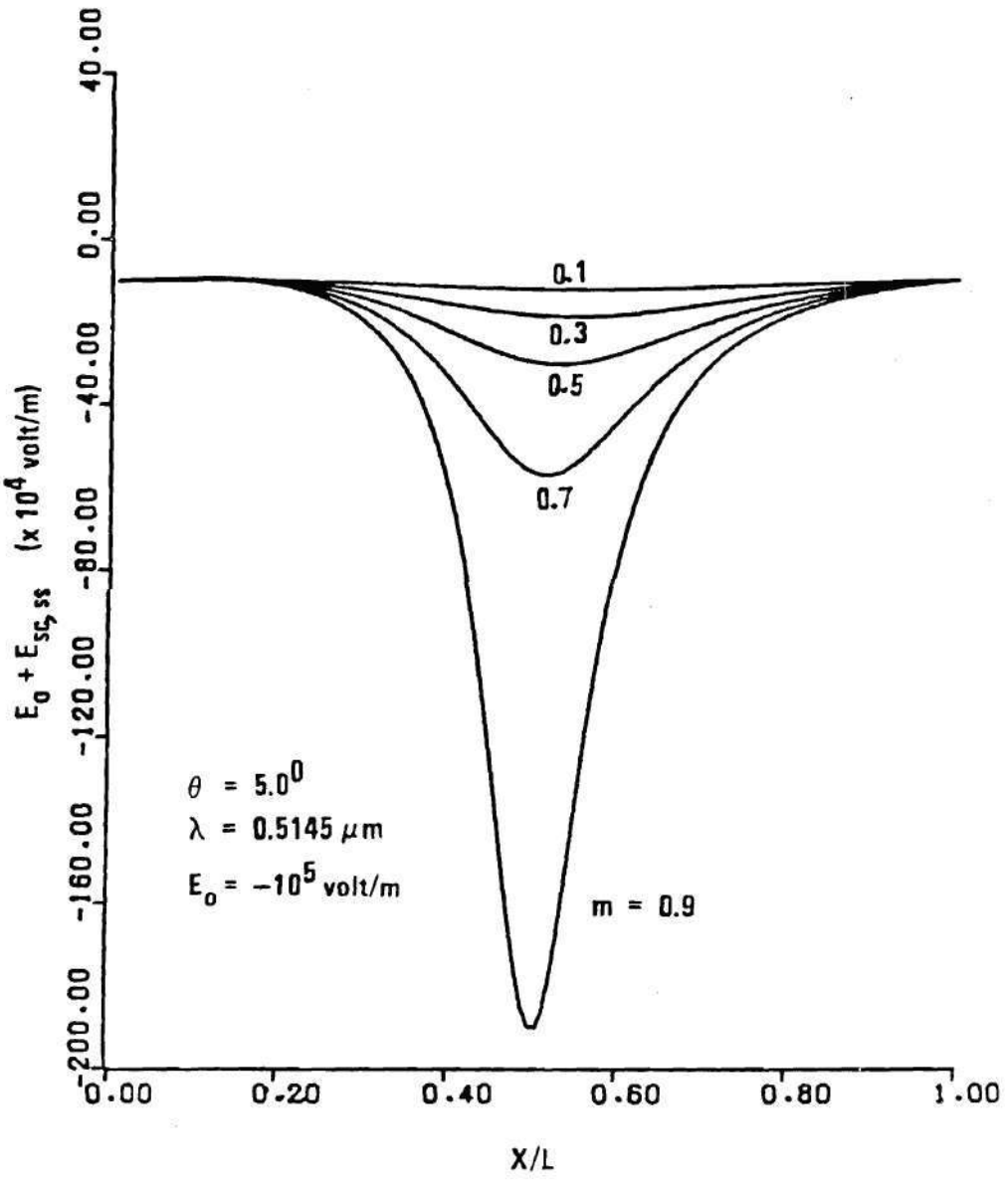

Figure 18. One Grating Period of the Steady-state Total Electric Field, $E(x) = E_o + E_{sc}(x)$, Produced by a Combination of Diffusion and Drift for Various Values of Beam Modulation Ratio.

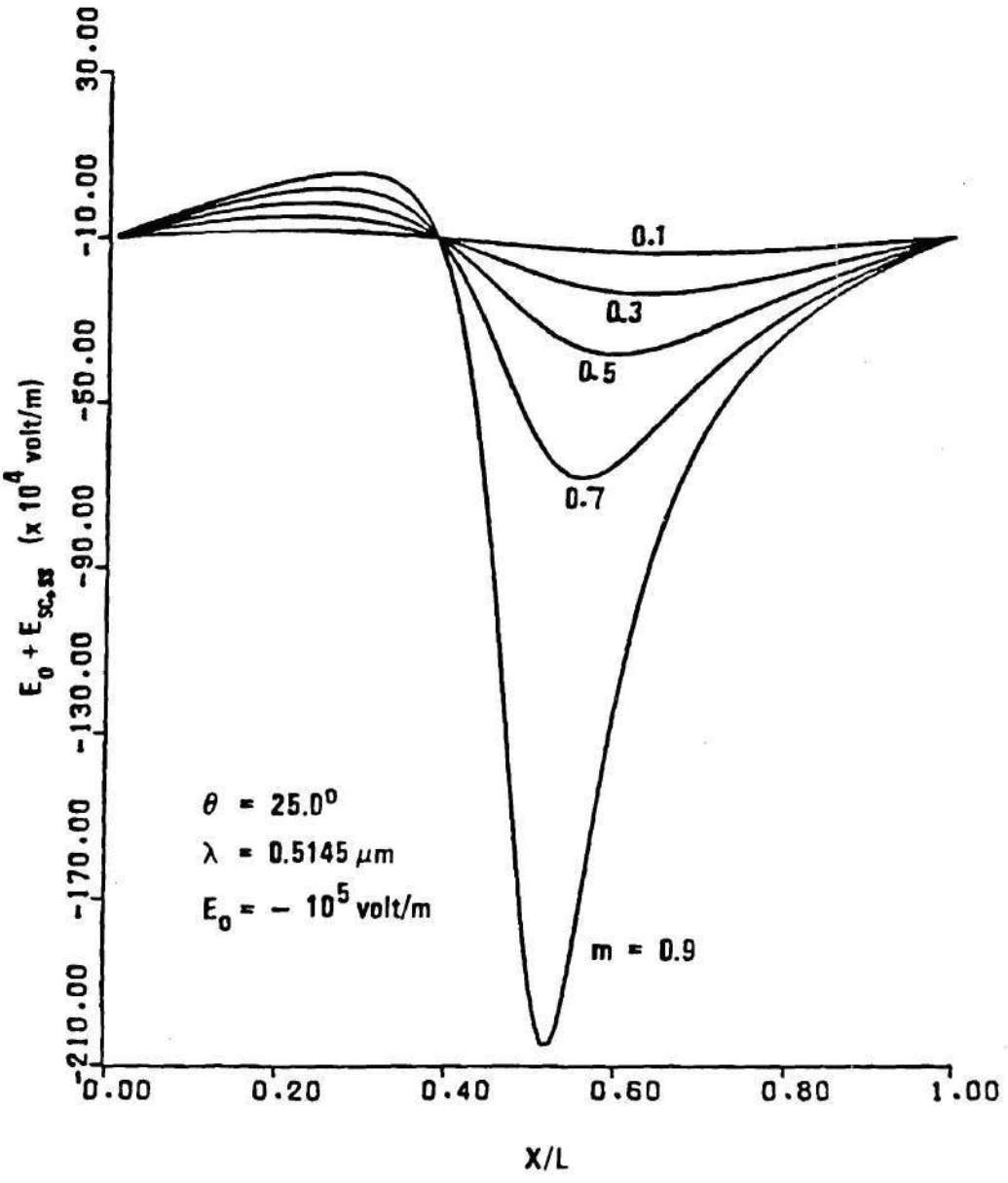

Figure 19. Same as Fig. 18 but for a Writing Angle of 25.0°.

the steady-state electric field patterns due to a combination of diffusion and drift for different values of beam modulation ratio at writing angles of 5.0° and 25.0°, respectively. In fact, the curves in Fig. 18 are the superpositions of the corresponding curves in Figs. 6 and 12, and the curves in Fig. 19 are the superpositions of the corresponding curves in Figs. 7 and 13. The field patterns in Fig. 18 are similar to those in Fig. 12. This reveals that when the writing angle is small, the diffusion component is small compared to the drift component. However, when the writing angle is large (small grating period), the diffusion component is important. This shows up in Fig. 19 in which the field patterns are quite different from those in Fig. 13. Finally, the steady-state electric field patterns due to a combination of diffusion and drift are plotted in Fig. 20.

These results indicate the following distinctions between the electric field patterns produced by the diffusion mechanism and those produced by the drift mechanism:

(i) The electric field pattern due to diffusion has odd symmetry at all times, whereas the field pattern due to drift has even symmetry at all times.

(ii) For diffusion, the field amplitude increases as writing angle increases (decreasing grating period). For drift, the field amplitude is independent of the writing angle (and grating period).

(iii) The exposure time needed to reach steady-state is somewhat longer for drift than for diffusion. In other words, the field due to diffusion saturates more rapidly than the field due to drift.

(iv) In the case of diffusion, the position for the maximum (and mini-

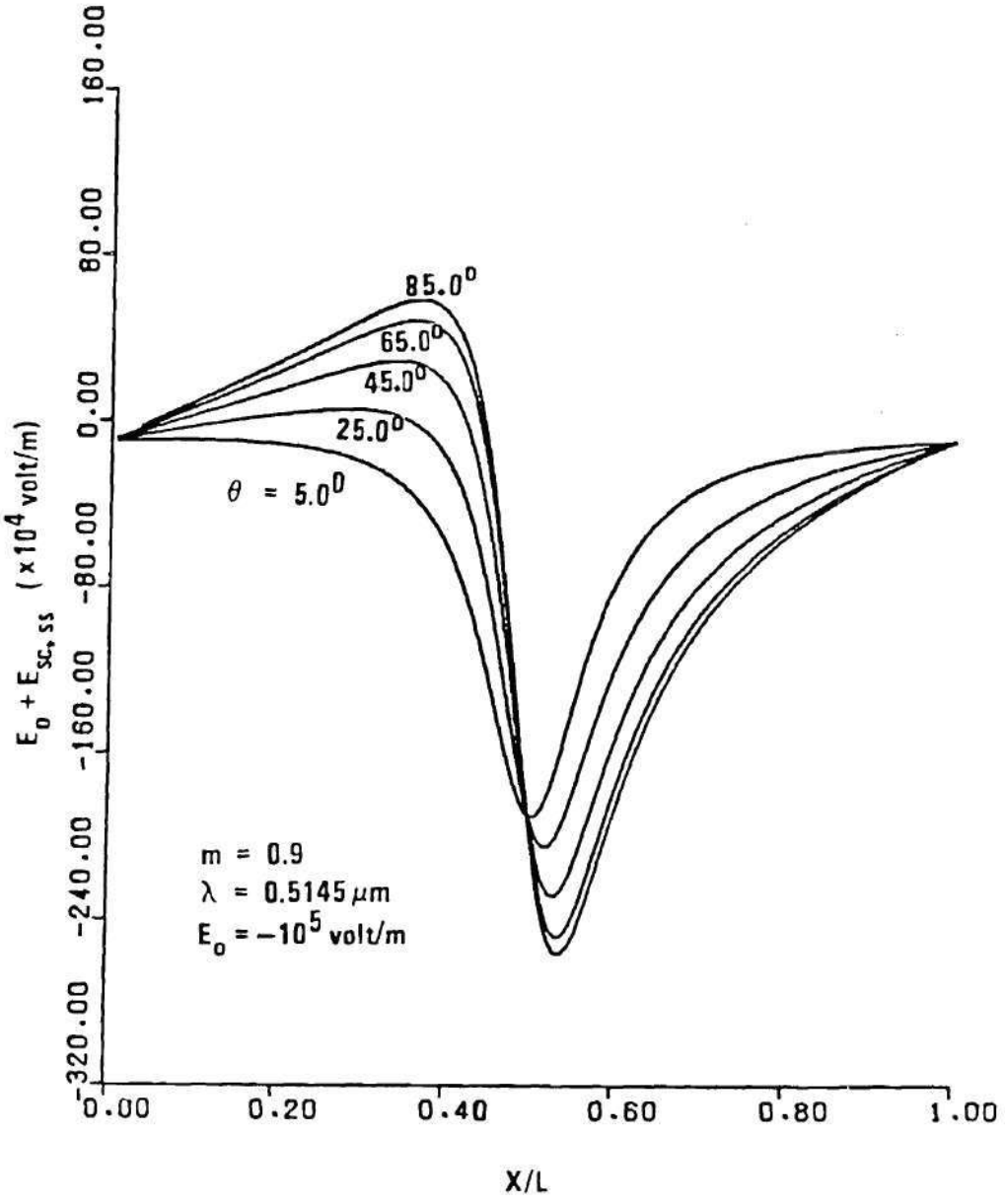

Figure 20. One Grating Period of the Calculated Steady-state Total Electric Field Produced by a Combination of Diffusion and Drift for Various Writing Angles.

mum) value of the electric field is a function of exposure. In the case of drift, the position for the field maximum (and minimum) remains fixed for all exposures.

(v) There is a 90.0° phase difference between the fundamental Fourier component of the electric field patterns for diffusion and drift for all exposures.

3.5 Discussion

The analysis of this chapter is applicable if holes instead of electrons were the charge carriers. The electric field pattern due to diffusion is the same as that produced by electrons except that it is reflected about the $x = 0$ axis [$E'_{sc}(x,t)$ becomes $E'_{sc}(-x,t)$]. The electric field patterns due to drift are independent of the type of charge carriers.

The electric field (due to diffusion and/or drift) in ferroelectric lithium niobate causes a spatial modulation of the refractive index via the electro-optic effect. For lithium niobate, the electro-optic effect is linear (Pockels effect). Thus, the amplitude of the modulation of the refractive index is proportional to the magnitude of the electric field. Therefore, the refractive-index pattern caused by the electric field via the electro-optic effect is the same as the electric field pattern calculated here. It follows that the spatial distribution of the refractive index (grating shape) resulting from diffusion is different from that resulting from drift. As indicated in Chapter II, different grating shapes produce different distributions of the higher-order diffraction efficiencies, and these higher-order diffraction efficiencies of a hologram grating produced by diffusion are different from

those of a hologram grating produced by drift. This indicates the possibility that the physical mechanisms (diffusion and/or drift) that occur during the hologram formation may be determined by measuring the higher-order diffraction efficiencies of a hologram.

CHAPTER IV

DETERMINATION OF GRATING SHAPE BY DIFFRACTION EFFICIENCIES[50]

4.1 Introduction

It has already been pointed out that volume (thick) holographic gratings have numerous applications. Among the materials used for recording volume holograms are those that exhibit light-induced refractive index changes (photorefractive effect), those that exhibit light-induced changes in optical absorption (photochromic effect), and those that exhibit both of these effects. Photorefractive materials include linear electro-optic, ferroelectric crystals such as lithium niobate.[45] In these materials, a sinusoidal exposure does not necessarily produce a sinusoidal change in refractive index. Depending on the material and the details of the exposure, different grating shapes may be generated.

In Chapter III, it has been shown that different refractive index profiles were generated through different types of physical mechanisms that are occuring during the writing of the holograms. In Chapter II, a method was presented for calculating the diffraction efficiencies of a thick dielectric grating having any aribitrary grating shape. In this chapter, the inverse problem is solved: a procedure for determining the grating shape from externally measurable quantities (such as diffraction efficiencies) is presented. It is assumed that the gratings are generated through a combination of diffusion and drift of photo-excited electrons and that an externally applied dc field and an effective photo-

voltaic field[27] may be present. The procedure is equally applicable to gratings generated through diffusion and drift of holes. However, Staebler and Amodei[49] have shown for lithium niobate that the refractive index gratings are generated by the diffusion and drift of electrons. With the procedure presented here, the grating shape of an unknown grating can be determined by knowing the fundamental and the higher-order diffraction efficiencies as measured at a single wavelength, which is not necessarily equal to the wavelength of the recording beams. This method utilizes the coupled-wave theory and, therefore, it is valid for thick (large Q) gratings. For thin dielectric gratings, in which the coupled-wave theory is not applicable, the refractive index profiles must in general be determined on the basis of electromagnetic boundary conditions. A detailed treatment of the diffraction by thin gratings is given in Ref. 51.

To test the calculational accuracy of the procedure, the refractive index profiles of thick gratings are determined from the calculated diffraction efficiency data for some known profile gratings. The results are then compared with the original profiles to verify the calculational accuracy of the procedure. In addition, as an illustration of the procedure, the refractive index profile of a lithium niobate holographic grating is determined from measurements of its fundamental and higher-order diffraction efficiencies.

4.2 The Model

All ferroelectric crystals exhibit a spontaneous polarization in a particular direction (polar axis) in the crystal. The polar axis has a positive sense in that the directions parallel and antiparallel to it

are distinguishable from one another. This may occur in ten out of the 32 crystal classes (point groups). Two of these ten crystal classes (1 and m) have no axis of rotational symmetry (e.g. $Bi_4Ti_3O_{12}$), while the remaining eight crystal classes (2, 3, 4, 6, 2m, 3m, 4m, and 6m) have a single axis of rotational symmetry (e.g. $LiNbO_3$, $Ba_2NaNb_5O_5$, and $BaTiO_3$). By convention[52] the c axis in these crystals is chosen to be the axis of rotational symmetry. The positive end of the c axis is defined via the piezoelectric effect.[52] For class 3m (e.g. $LiNbO_3$) the positive end of the c axis is the end that becomes negative when compression is applied to the c axis. All ferroelectric crystals lack inversion symmetry in their crystal structure and as such may exhibit the linear electrooptic effect (Pockels effect). The quadratic electrooptic effect (Kerr effect) may also be present, but usually the linear effect is dominant. Thus the quadratic effect is neglected here.

The geometry used for a thick optically-induced grating is presented in Fig. 21. The +x direction is chosen to coincide with the +c direction and is in the plane of incidence and parallel to the surfaces of the crystal, the y axis is perpendicular to the page, and the z axis is perpendicular to the surfaces of the crystal. The crystal is assumed to be lossless and the grating is assumed to be a pure phase grating. The light intensity (power per unit area transverse to the direction of energy flow) producing the grating is the sinusoidal interference pattern produced by the intersection of two plane waves and is given by Eq. (53). The electric field pattern, and therefore the grating profile, inside the crystal is also periodic (but not necessarily sinusoidal) in the x direction with period L. For simplicity, the grating is assumed to be

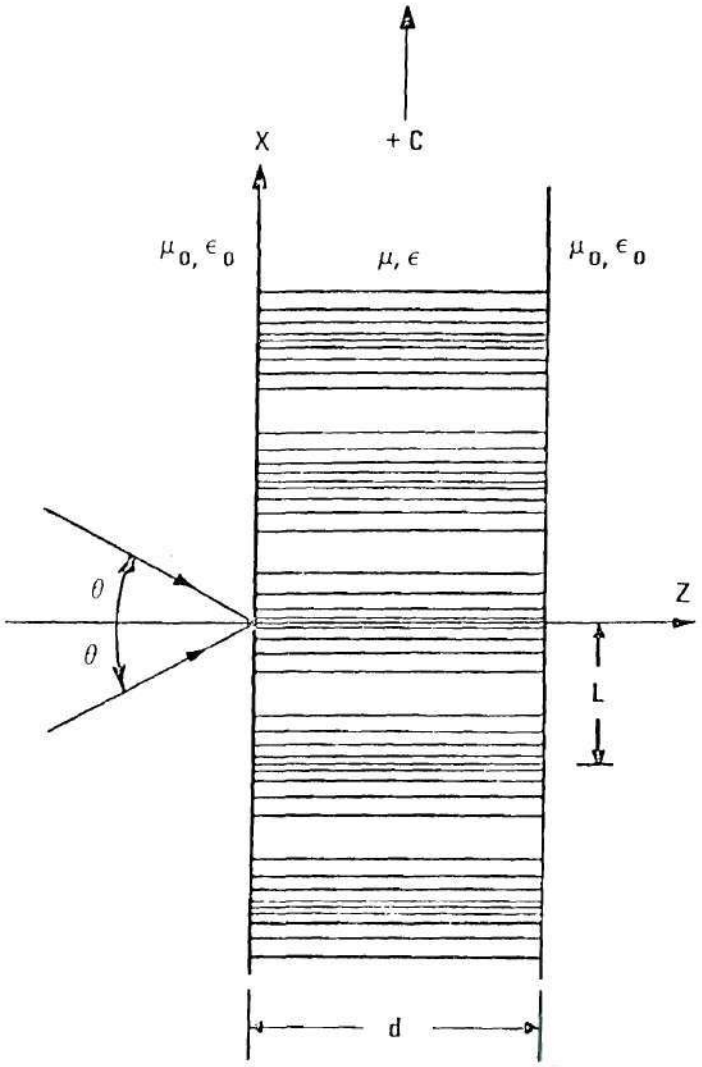

Figure 21. Geometry of a Thick Grating Showing Recording Beams. The Spatial Modulation of the Refractive Index Is Indicated by the Line Pattern.

uniform in the z direction.

4.3 Normalized Fourier Grating Components

The electric field patterns, and therefore the grating profiles, generated through diffusion and drift of electrons can be obtained for any given wavelength, exposure, and geometrical configuration either by analytic methods[47,48] or by a numerical method.[46] An analytical expression for the space-charge electric field pattern has been obtained by Cornish et al.[48] as given by

$$E_{sc}(x,t) = [(k_b T/e)\, mK \sin Kx + mE_o(1 - \cos Kx)](1 + m \cos Kx)^{-1}$$

$$\times \{1 - \exp[(-e\mu_n \tau g_o t/\varepsilon)(1 + m \cos Kx)]\}. \qquad (72)$$

Equation (72) can also be obtained from Eqs. (12) and (14) of Ref. 47 by choosing G = 0, since the constant G can be chosen arbitrarily. The term containing sin Kx in Eq. (72) is due to diffusion and the term containing (1 - cos Kx) is due to drift. In addition to the analytical expressions, the same electric field pattern can also be obtained numerically.[46] For convenience, a few typical numerical results are, again, presented here in Figs. 22, 23, and 24.* Figure 22 shows one grating period of the diffusion component of the electric field pattern. Figure 23 presents one grating period of the drift component of the electric field pattern produced with a uniform dc field E_o equal to -10^4 V/m

*It is easily shown, by plotting Eq. (72) with the same parameter values as in the numerical approach, that the analytical results thus obtained are in agreement with the numerical results obtained by the method given in Ref. 46.

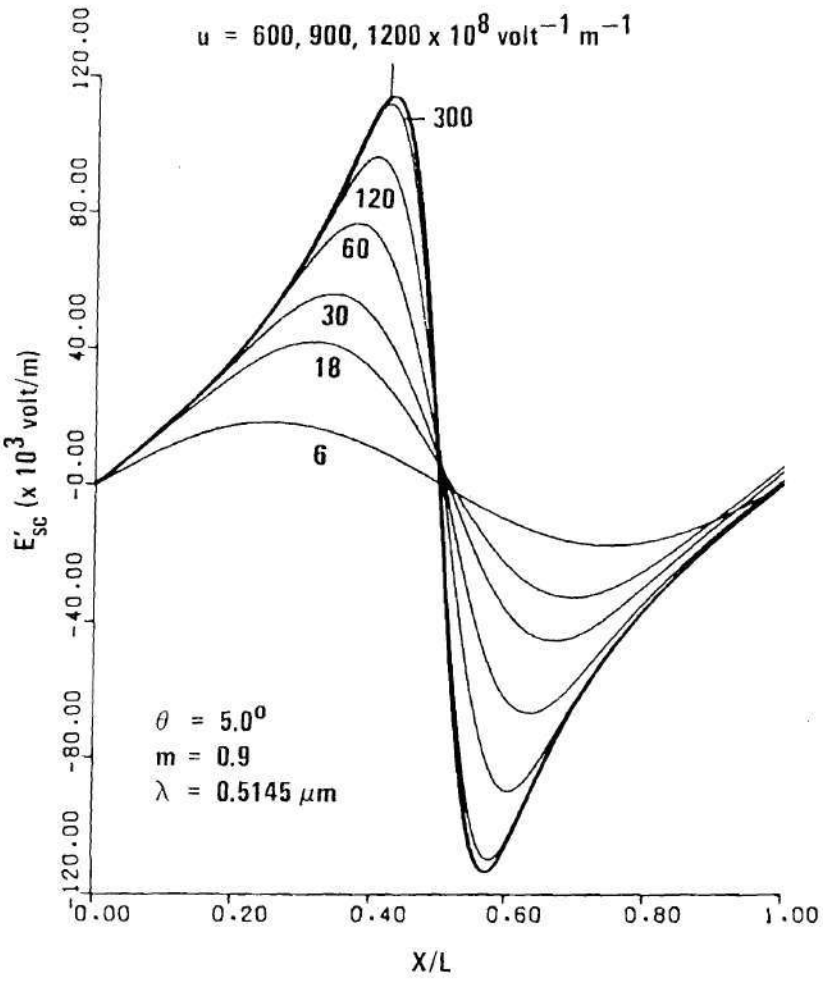

Figure 22. One Grating Period of the Calculated Diffusion Component of the Space-charge Field. No Drift is Present ($E_o = 0$ and $E''_{sc} = 0$).

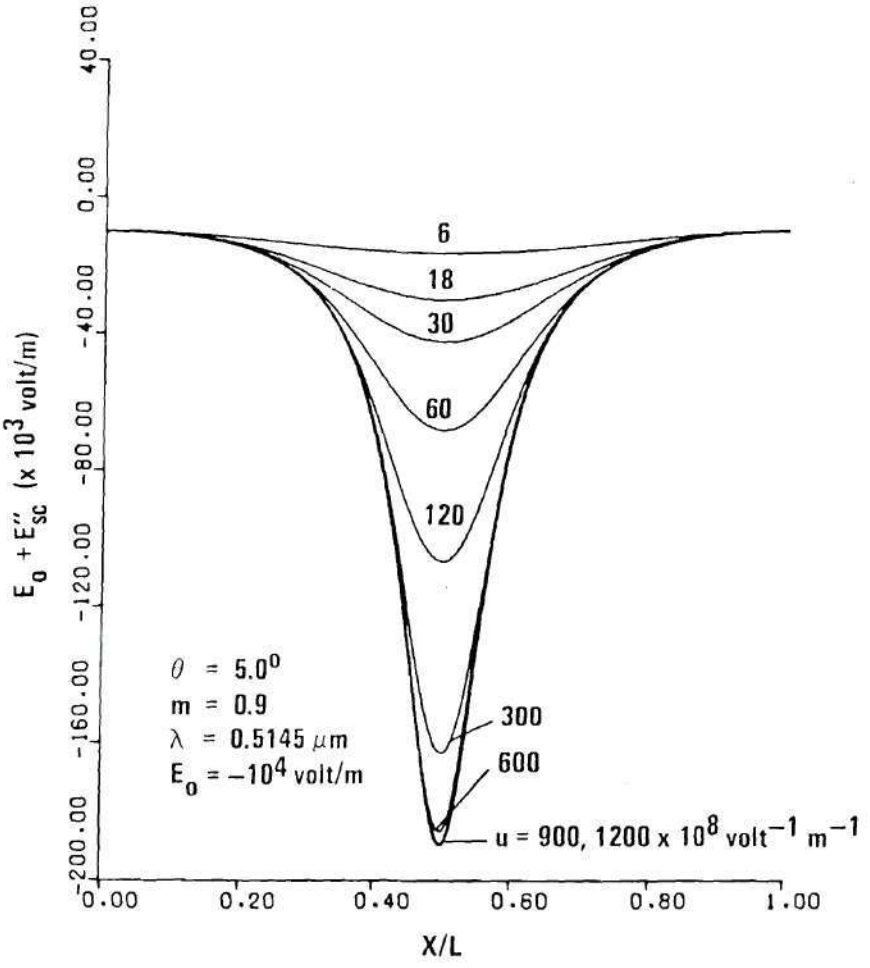

Figure 23. One Grating Period of the Calculated Drift Component of the Total Electric Field. No Diffusion is Present ($E'_{sc} = 0$).

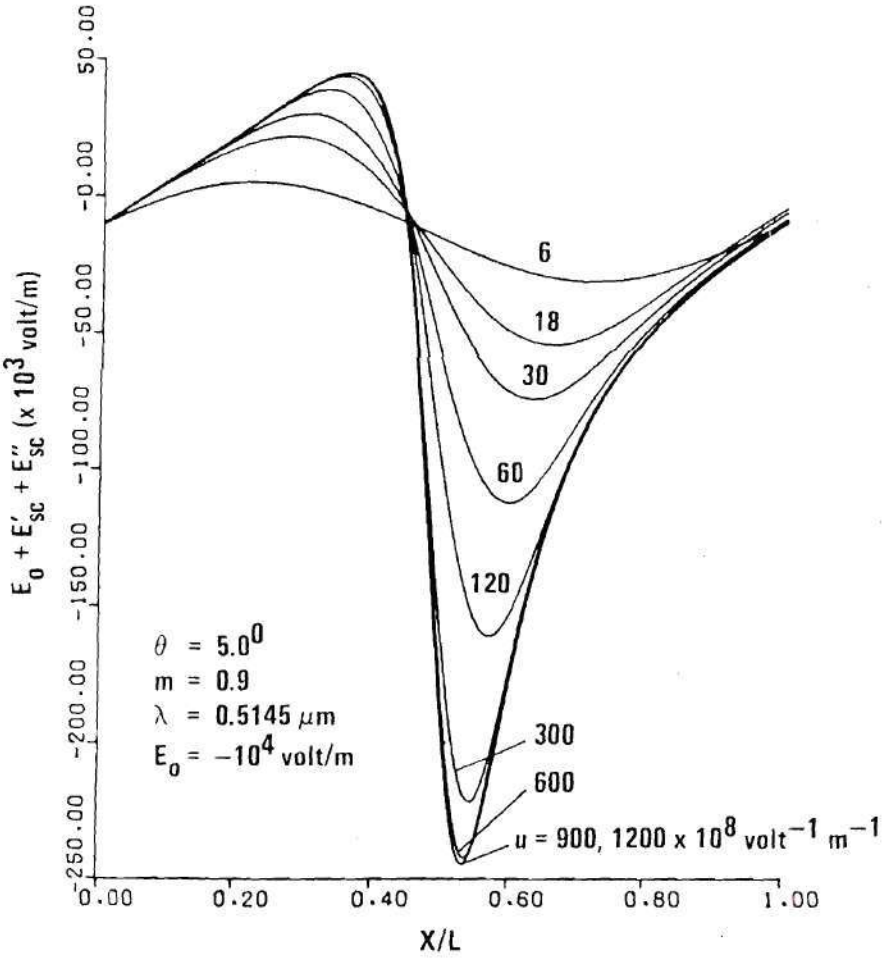

Figure 24. One Grating Period of the Calculated Total Electric Field Produced by a Combination of Diffusion and Drift.

during writing. The electric field E_o, in general, is the sum of an externally applied field and an effective field produced by the bulk photovoltaic effect in the material. Figure 24 shows one grating period of the total electric field pattern due to a combination of diffusion and drift with E_o equal to -10^4 V/m. In fact, each curve in Fig. 24 is the sum of the corresponding curves in Figs. 22 and 23. The permittivity used was $\varepsilon = 30\,\varepsilon_o$ and the exposure parameter u used in Figs. 22, 23, and 24 is given by $u = \mu_n \tau g_o t$. This u will henceforth be used as the independent variable. Frequently, the exposure time is used as the independent variable, however, it is more general to use the exposure parameter u. For photorefractive materials exhibiting the linear electro-optic effect, the grating profiles generated are geometrically the same as the electric field patterns. Therefore, when multiplied by the appropriate electro-optic coefficient of the crystal, the electric field patterns obtained here become the grating profiles generated through diffusion and/or drift of electrons.

Since the grating profiles generated for any given value of u are periodic in the x direction with period L, the refractive index modulation amplitude $\Delta n(x) \equiv n(x) - n_o$, which is proportional to $E_{sc}(x)$, can be written as a Fourier series

$$\Delta n(x) \equiv n(x) - n_o = \sum_{h=1}^{\infty} [n_{sh} \sin(hKx) + n_{ch} \cos(hKx)], \qquad (73)$$

where the Fourier components n_{sh} and n_{ch} are given by

$$n_{sh} = (2/L) \int_0^L n(x) \sin(hKx)\, dx, \qquad (74)$$

and

$$n_{ch} = (2/L) \int_0^L n(x)\cos(hKx)\ dx. \qquad (75)$$

As shown in Eq. (72) and in Fig. 22, the grating profiles generated through diffusion of electrons have odd symmetry with respect to the origin of the interference pattern ($x = 0$). Therefore, they can always be expanded in a sine series ($n_{ch} = 0$). Likewise, the grating profiles generated through drift of electrons have even symmetry with respect to $x = 0$ and can always be expanded in a cosine series ($n_{sh} = 0$). In the case that the grating profiles are generated through a combination of diffusion and drift, the Fourier series for these grating profiles, of course, contains both sine and cosine terms. To use Eqs. (74) and (75) to determine the Fourier components n_{sh} and n_{ch}, the grating profile $n(x)$ must be known in advance. This means that to determine n_{sh} and n_{ch}, the electric field patterns and the appropriate electro-optic coefficient of the crystal must be known. In the procedure to be presented here, however, only the normalized Fourier components are needed and these can be determined from the electric field patterns without knowledge of the linear electro-optic coefficient of the crystal. Using Eqs. (74) and (75), the normalized Fourier components are

$$f_{sh} \equiv n_{sh}/n_{sl} = \int_0^L E_{sc}(x)\ \sin(hKx)\ dx \ /\ \int_0^L E_{sc}(x)\ \sin(Kx)\ dx, \qquad (76)$$

and

$$f_{ch} \equiv n_{ch}/n_{cl} = \int_0^L E_{sc}(x)\ \cos(hKx)\ dx \ /\ \int_0^L E_{sc}(x)\ \cos(Kx)\ dx, \qquad (77)$$

where $E_{sc}(x)$ is the generated space-charge electric field pattern. Equations (76) and (77) represent the normalized Fourier components of a grating profile for a given exposure parameter u and writing beam modulation ratio m. Substituting Eq. (72) into Eqs. (76) and (77), letting $\xi \equiv Kx$, and using the property that integration of an odd periodic function over one period is zero, gives

$$f_{sh} = \int_0^{2\pi} g_1(\xi) \sin(h\xi)\, d\xi \;/\; \int_0^{2\pi} g_1(\xi) \sin\xi\, d\xi, \tag{78}$$

and

$$f_{ch} = \int_0^{2\pi} g_2(\xi) \cos(h\xi)\, d\xi \;/\; \int_0^{2\pi} g_2(\xi) \cos\xi\, d\xi, \tag{79}$$

where

$$g_1(\xi) = \sin\xi\,(1 + m\cos\xi)^{-1}\left\{1 - \exp\left[(-eu/\varepsilon)(1 + m\cos\xi)\right]\right\}, \tag{80}$$

and

$$g_2(\xi) = (1 - \cos\xi)(1 + m\cos\xi)^{-1}\left\{1 - \exp\left[(-eu/\varepsilon)(1 + m\cos\xi)\right]\right\}. \tag{81}$$

For the case of pure diffusion, there are no cosine terms in the Fourier series. Under this condition, only Eq. (78) has physical significance. Likewise, for the case of pure drift, only Eq. (79) has physical significance. From Eqs. (78) and (79), the normalized Fourier components f_{sh} and f_{ch} are independent of E_o and K. Physically, this means that f_{sh} and

f_{ch} are independent of the electric field E_o, the wavelength, and the incident angle of the writing beams. They are functions of u and m only. Thus, for a given value of m, $f_{sh} = f_{sh}(u)$ and $f_{ch} = f_{ch}(u)$. Figures 25, 26, and 27 present the first few orders of these normalized Fourier components as a function of u for beam modulation ratio m equal to 0.9, 0.5, and 0.1, respectively. The curves in Figs. 25, 26, and 27 are numerically obtained by use of Eqs. (78) and (79) for the exposure parameter u ranging from zero to 3×10^{10} $V^{-1}m^{-1}$. From Figs. 25, 26, and 27, it is seen that the beam modulation ratio m has a great influence on the normalized Fourier components $f_{sh}(u)$ and $f_{ch}(u)$. The absolute values of $f_{sh}(u)$ and $f_{ch}(u)$ increases with increasing m. Thus, for a given exposure, the higher-order grating harmonics are larger and the gratings become more nonsinusoidal for larger writing beam modulation ratios. From Figs. 25, 26, and 27, it is also observed that the absolute values of $f_{sh}(u)$ and $f_{ch}(u)$ for a given h increase with increasing u and then saturate and become equal to each other when u exceeds a certain level. The value of this level, however, depends on the modulation ratio m, increasing with increasing m. That is, $f_{sh}(u)$ and $f_{ch}(u)$ saturate slower for larger values of m. This means that the refractive index profiles reach their final shape at a lower exposure for smaller modulation ratios.

The fact that the normalized Fourier components $f_{sh}(u)$ and $f_{ch}(u)$ are independent of the electric field E_o, the wavelength, and the incident angle of the writing beams, combined with the coupled-wave method for calculating the diffraction efficiencies can be used to develop a procedure to determine the grating profile of the gratings produced by diffusion and drift of electrons knowing the fundamental and the higher-order

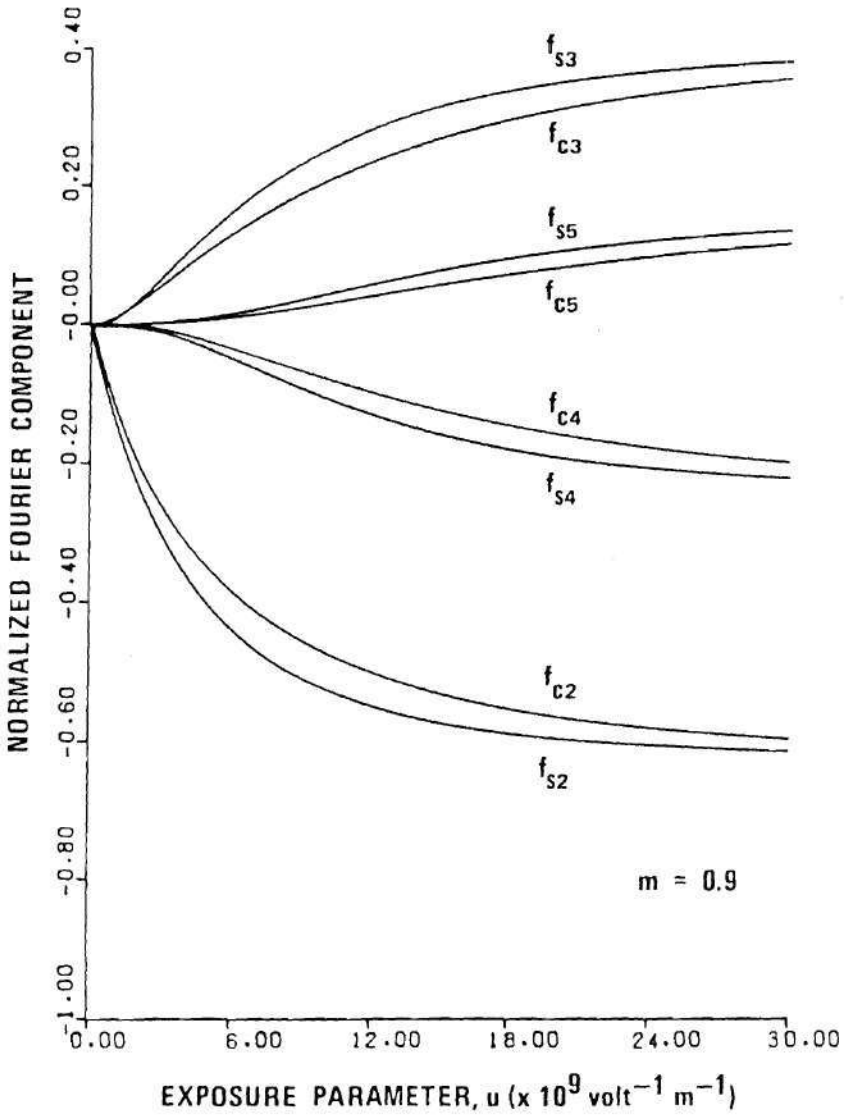

Figure 25. Normalized Fourier Components of the Grating Profile Generated Through Diffusion (Ratios of Sine Components) and Through Drift (Ratios of Cosine Components) as Functions of Exposure Parameter for a Modulation Ratio of 0.9.

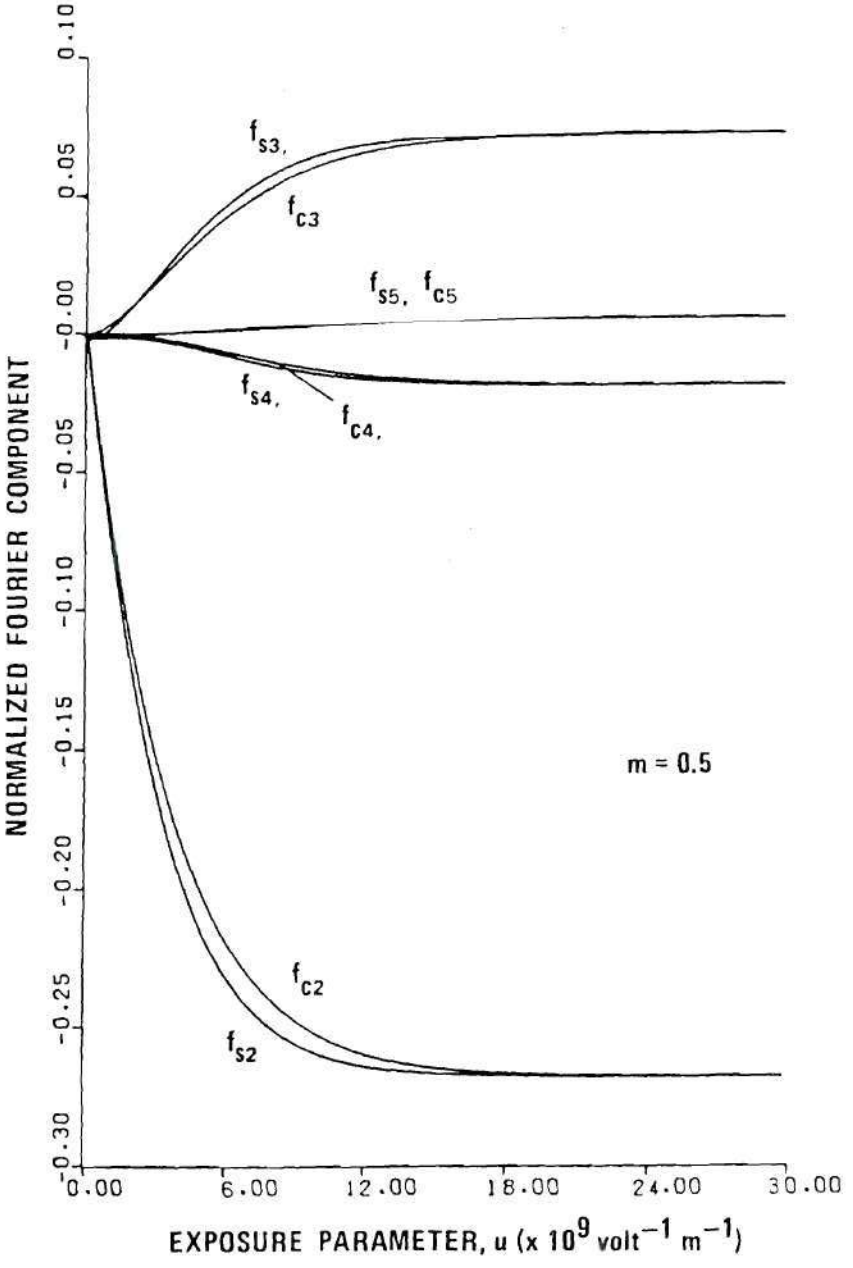

Figure 26. Same as Fig. 25 but for a Modulation Ratio of 0.5.

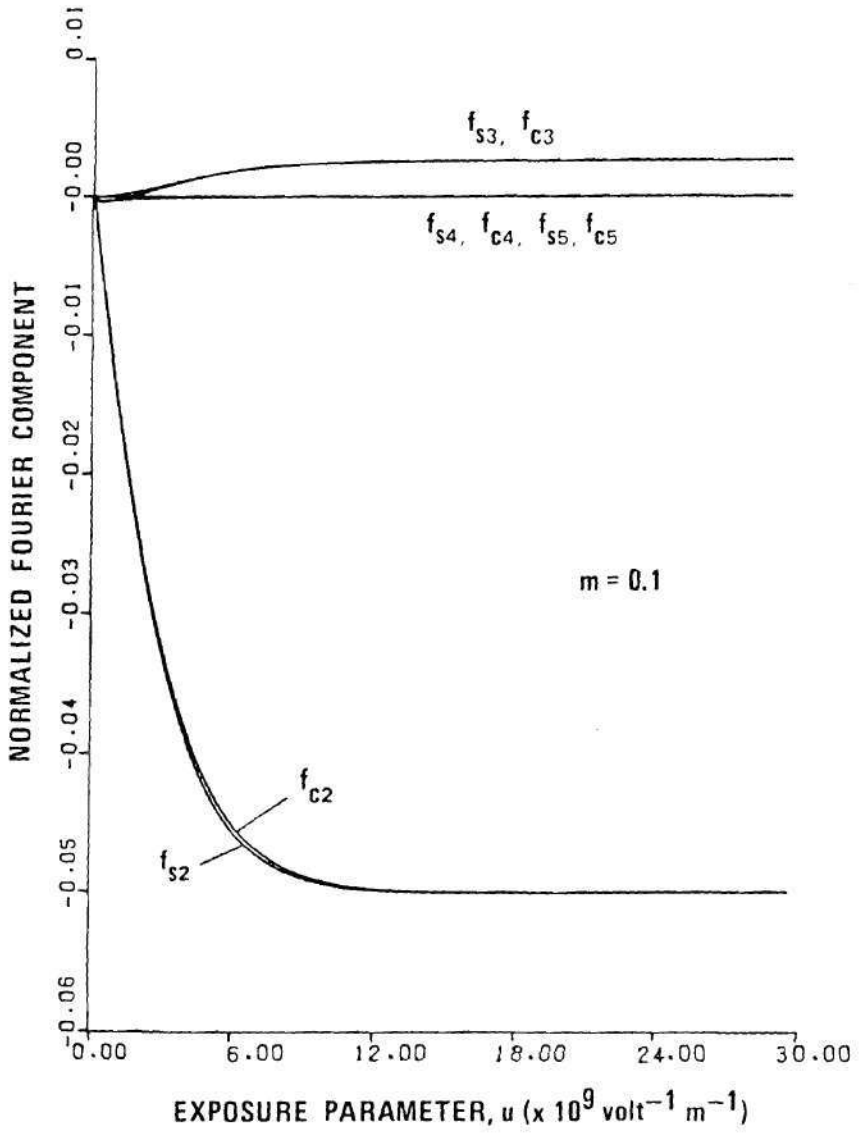

Figure 27. Same as Fig. 25 but for a Modulation Ratio of 0.1.

diffraction efficiencies of these gratings.

4.4 Determination of the Refractive Index Profile

4.4.1 Theory

In the preceding section, the characteristics of the normalized Fourier components f_{sh} and f_{ch} have been analyzed for gratings generated through diffusion and drift of electrons. In this section, the refractive index profile of these gratings are determined by knowing the fundamental and the higher-order diffraction efficiencies.

The m th-order diffraction efficiency for an E mode incident wave (wave polarized in plane of incidence) of free space wavelength λ_r at the m th-order Bragg angle θ_m is given by Eq. (46). A counterpart expression for the diffraction efficiency for H mode incident wave (wave polarized perpendicular to plane of incidence) is given by Eq. (33). The diffraction efficiencies are thus given and the Fourier components n_{sh} and n_{ch} are the quantities to be determined.

From Eq. (46), the first- and second-order diffraction efficiencies are

$$DE_1 = \sin^2 \{ [(n_{s1})^2 + (n_{c1})^2]^{\frac{1}{2}} \pi d \cos(2\theta_1)/(\lambda_r \cos \phi_1) \}, \qquad (82)$$

and

$$DE_2 = \sin^2 \left[\left(\{ L^2 n_o [(n_{c1})^2 - (n_{s1})^2] / (\lambda_r)^2 + n_{c2} \}^2 + [2L^2 n_o n_{s1} n_{c1} \right. \right.$$

$$\left. \left. / (\lambda_r)^2 + n_{s2}]^2 \right)^{\frac{1}{2}} \pi d \cos(2\theta_2)/(\lambda_r \cos \phi_2) \right]. \qquad (83)$$

From Eqs. (76) and (77),

$$n_{sh} = n_{sl}\, f_{sh}, \qquad h = 2, 3, 4, \cdots, \tag{84}$$

$$n_{ch} = n_{cl}\, f_{ch}, \qquad h = 2, 3, 4, \cdots. \tag{85}$$

Substituting Eqs. (84) and (85) into Eq. (83) with h = 2 gives

$$DE_2 = \sin^2\left[\left(\left\{L^2 n_o\left[(n_{cl})^2 - (n_{sl})^2\right]/(\lambda_r)^2 + n_{cl} f_{c2}\right\}^2 + \left[2L^2 n_o n_{sl} n_{cl}\right.\right.\right.$$

$$\left.\left.\left./(\lambda_r)^2 + n_{sl} f_{s2}\right]^2\right)^{\frac{1}{2}} \pi d \cos(2\theta_2)/(\lambda_r \cos\phi_2)\right]. \tag{86}$$

The values of f_{s2} and f_{c2} can be calculated for any given u via Eqs. (78) and (79). Therefore, n_{sl} and n_{cl} can be obtained for the same value of u by solving Eqs. (82) and (86) simultaneously. This can be achieved either analytically or numerically. Solving Eqs. (82) and (86) for a value of u, we get a pair of solutions denoted by $n_{sl}(u)$ and $n_{cl}(u)$. After solving Eqs. (82) and (86), the signs of the resultant n_{sl} and n_{cl} must be carefully chosen. These, of course, depend on the physical property of the recording material. Turner[53] has shown that, for lithium niobate with the +c axis directed in the +x reference direction, a positive electric field decreases the refractive index. That is, $\Delta n(x) \propto -E_{sc}(x)$. In this case, a Fourier series expansion [in the form of Eq. (73)] of $-E_{sc}(x)$ with $E_{sc}(x)$ given by Eq. (72) shows that n_{sl} is always negative and that n_{cl} is positive when E_o is positive (directed in the +x direction) and negative when E_o is negative. Ohmori et al.[54] have shown that

an applied external electric field in the +c direction during illumination results in a decreased index modulation for lithium niobate. Likewise, an applied field in the -c direction during illumination results in an increased index modulation. From this, the polarity of the effective electric field E_o is seen to be negative (directed in the -c direction). Therefore, the negative sign for n_{c1} must be chosen. Similarly, if the +c axis is in the -x direction, it can be shown that the positive sign for n_{s1} and the negative sign for n_{c1} must be chosen. No matter which direction (+x or -x) is chosen for the +c axis direction, the same refractive index profile in the lithium niobate crystal is obtained. This shows that there is no ambiguity in the solution. Once n_{s1} and n_{c1} are obtained, the corresponding higher-order Fourier components n_{s2}, n_{c2}, n_{s3}, n_{c3}, and so forth can be obtained via Eqs. (84) and (85). With this set of Fourier components, a new set of higher-order (higher than second order) diffraction efficiencies (as opposed to the original given set of diffraction efficiencies) are calculated. Let this new set of higher-order diffraction efficiencies be denoted by $DE_3'(u)$, $DE_4'(u)$, and so forth. This entire process is then repeated for other values of u. The particular value of u is sought that gives calculated higher-order diffraction efficiencies in agreement with the original diffraction efficiencies. An approximation to this value can be found numerically by the method of least squares. The sum of the squares of the deviations of the calculated diffraction efficiencies from the original diffraction efficiencies is

$$\delta(u) = \sum_{m=3,4,\ldots} [DE_m - DE_m'(u)]^2. \tag{87}$$

Using numerical techniques, a search is made for the particular u, say u_p, that results in a minimum $\delta(u)$. That is $\delta(u_p) \leq \delta(u)$ for all other values of u. The corresponding Fourier components $n_{sh}(u_p)$ and $n_{ch}(u_p)$, h = 1, 2, 3, ···, are the solutions desired. It should be noted that since DE_4, DE_5, etc. are usually very small compared to DE_3, the minimization of Eq. (87) is essentially equivalent to finding the value of u that produces the best match of DE_3.

As an example of the numerical method, Eqs. (82) and (86) may be solved to obtain $\delta(u)$ for a sequence of u with each u in the sequence being separated from its neighbors by an interval Δu. Selecting the particular u_p that induces the smallest $\delta(u)$, gives the Fourier components, $n_{sh}(u_p)$ and $n_{ch}(u_p)$, that are the desired solutions. The number of values of u in the sequence depends on the magnitude of Δu and the range of the exposure parameter. For example, if Δu is equal to 1.0×10^{8} $V^{-1}m^{-1}$ and the range of the exposure parameter explored is equal to 3.0×10^{10} $V^{-1}m^{-1}$, then the number of values of u in the sequence is 300. Of course, the smaller the value of Δu used the more accurate the solution will be. For practical calculations, the number of values of u in the sequence may be several hundreds to several thousands.

4.4.2 Summary of Method

From the foregoing analysis, a method to determine the refractive index profile of a thick grating, which was generated through diffusion and drift of electrons, may be summarized as follows:

1.. Given: m (beam modulation ratio during writing), DE_1, DE_2, DE_3, ···.

2. Procedure:

a. Generate the functions $f_{sh}(u)$ and $f_{ch}(u)$ via Eqs. (78) and (79).

b. Solve for the fundamental Fourier components $n_{s1}(u)$ and $n_{c1}(u)$ by use of Eqs. (82) and (86) for a value of u. Determine the corresponding higher-order Fourier components via Eqs. (84) and (85).

c. Calculate the new diffraction efficiencies $DE_3'(u)$, $DE_4'(u)$, etc. and then the sum of the squares of the deviations of the calculated diffraction efficiencies from the original diffraction efficiencies $\delta(u)$.

d. Repeat steps b and c for other values of u and then select the particular u_p that induces the smallest $\delta(u)$. The corresponding Fourier components, $n_{sh}(u_p)$ and $n_{ch}(u_p)$, h = 1, 2, 3, ···, are the solutions.

3. Results: The refractive index profile is obtained by substituting $n_{sh}(u_p)$ and $n_{ch}(u_p)$ into Eq. (73).

4.4.3 Test of calculational Accuracy

The procedure was numerically implemented and tested by determining the Fourier components of three typical gratings from the calculated diffraction efficiencies of these gratings. These gratings have the refractive index profile produced by the electric field patterns $[\Delta n(x) \propto -E_{sc}(x)]$ represented by the curves corresponding to u = 300 x 10^8 $V^{-1}m^{-1}$ in Figs. 22, 23, and 24. The first few orders of the Fourier components of the refractive index profile of these gratings are listed in the "original" rows in Table 10. The diffraction efficiencies of these gratings are calculated with $\lambda_r = 514.5$nm. With these diffraction efficiency data, the Fourier components of the refractive index of these gratings are determined by the procedure. The calculated Fourier components are

Table 10. Comparison of the Original Fourier Components and the Calculated Fourier Components of the Gratings Generated Through Diffusion of Electrons, Drift of Electrons, and a Combination of the Two.

Physical mechanism		Refractive Index Fourier Component (x 10^{-5})									
		n_{c1}	n_{s1}	n_{c2}	n_{s2}	n_{c3}	n_{s3}	n_{c4}	n_{s4}	n_{c5}	n_{s5}
Diffusion	Original	0.000	-6.842	0.000	4.216	0.000	-2.566	0.000	1.536	0.000	-0.900
	Calculated	0.000	-6.842	0.000	4.216	0.000	-2.566	0.000	1.536	0.000	-0.899
Drift	Original	-4.997	0.000	2.988	0.000	-1.755	0.000	1.009	0.000	-0.566	0.000
	Calculated	-4.997	0.000	2.988	0.000	-1.755	0.000	1.009	0.000	-0.566	0.000
Diffusion & Drift	Original	-4.997	-6.842	2.988	4.216	-1.755	-2.566	1.009	1.536	-0.566	-0.900
	Calculated	-4.997	-6.842	2.988	4.216	-1.755	-2.566	1.009	1.536	-0.566	-0.899

listed in the "calculated" rows in Table 10. From Table 10, it is seen that the procedure yields excellent numerical accuracy. The largest percentage deviation of the calculated Fourier components from the original Fourier components is about one tenth of 1%. Other reading wavelengths (488.0 and 632.8 nm) have also been used to perform these calculations and the same results were obtained. This illustrates that the reading wavelength λ_r used in the procedure is not necessarily equal to the wavelength λ of the writing beams that produce the grating and that the refractive index profile determined is independent of the reading wavelength. In addition to the grating profiles listed in Table 10, other grating profiles (such as the grating profiles generated by the electric field patterns represented by the u = 30, 60, and 120 x 10^8 $V^{-1}m^{-1}$ curves in Figs. 22, 23, and 24) have also been used to test the procedure and deviations greater than one tenth of 1% were not found for any case.

4.4.4 Effect of Boundary Reflections

The effect of boundary reflections was not included in the procedure. In practice, boundary reflections can sometimes be eliminated by antireflection coatings on the surfaces of the grating. However, antireflection coatings usually eliminate reflections only for a particular wavelength and angle. Since numerous different angles are required in the procedure, antireflection coatings may be impractical. When boundary reflections exist, the measured diffraction efficiency at each Bragg angle must be corrected by dividing by the appropriate transmittance factor τ_m.[35,55] When the surfaces of the grating are perfectly flat and perfectly parallel, this transmittance factor is given by Eq. (34). The R_m in Eq. (34) for E-mode polarization of the reading beam is given by

$R_m = \tan^2(\theta_m - \phi_m)/\tan^2(\theta_m + \phi_m)$. Equation (34) is a very sensitive function of grating thickness; a change of a fraction of a wavelength in thickness may produce a relatively large change in the value of τ_m. In this case, mechanical measurements of the grating thickness alone are not sufficiently precise. Optical measurements of the grating thickness need to be employed to supplement the mechanical measurements. An optical method to determine the grating thickness is measuring the incident and the transmitted powers of a beam incident on the grating. The thickness of the grating is given in terms of the ratio of the transmitted and incident power by[56]

$$d = (1/2\beta)\cos^{-1}\{[(1 + R^2) - (1 - R)^2(P_i/P_t)]/(2R)\}, \qquad (88)$$

where P_i and P_t are the incident and transmitted powers, respectively, $R = \tan^2(\theta - \phi)/\tan^2(\theta + \phi)$, and $\beta = 2\pi n_o(\cos\phi)/\lambda_r$. The angle ϕ is the refraction angle corresponding to any angle of incidence θ. In order to use Eq. (88), the angle of incidence θ must be sufficiently angularly separated from any Bragg angle in these thick gratings so that there is negligible diffraction (or equivalently the measurement can be made before the grating is recorded). There are an infinite number of values of d that satisfy Eq. (88). However, the one that is closest to the value obtained from the mechanical measurement can be chosen. In most practical cases, the surfaces of the gratings are neither perfectly flat nor perfectly parallel. If the cosine factors in Eq. (34) average to zero due to variations in thickness over the illuminated region, the transmittance factor reduces to

$$\tau_m = (1 - R_m)^2/[1 + (R_m)^2]. \tag{89}$$

The transmittance as given by Eq. (89) is not a function of the grating thickness and thus the need for a precision thickness measurement is alleviated in this case. The diffraction efficiency expressions [Eqs. (33) and (46)], however, still require a knowledge of the grating thickness. In this case, mechanical measurements of the thickness are usually sufficiently precise as the diffraction efficiencies are relatively insensitive to errors in the grating thickness.

4.4.5 Effect of Experimental Errors

Using the foregoing procedure, the refractive index profile of a grating in a linear electro-optic crystal can be determined if the fundamental and the higher-order diffraction efficiencies of the grating are known. The diffraction efficiencies are measured values, and therefore, some experimental error is unavoidable. These experimental errors will affect the calculated grating refractive index profile. However, if the errors are small, a reasonably accurate grating profile can still be obtained. This is illustrated in Fig. 28. The central curve in Fig. 28 represents the actual profile of a grating. The other curves in Fig. 28 represent the grating profiles calculated from diffraction efficiencies which are 5% lower and 5% higher than those corresponding to the actual profile. From Fig. 28, it is observed that a several percent systematic error in the diffraction efficiencies results in a small change in the calculated grating profile. In addition to the grating profile presented in Fig. 28, other grating profiles produced with smaller exposure parameters have also been analyzed. It is found that the error in the grating

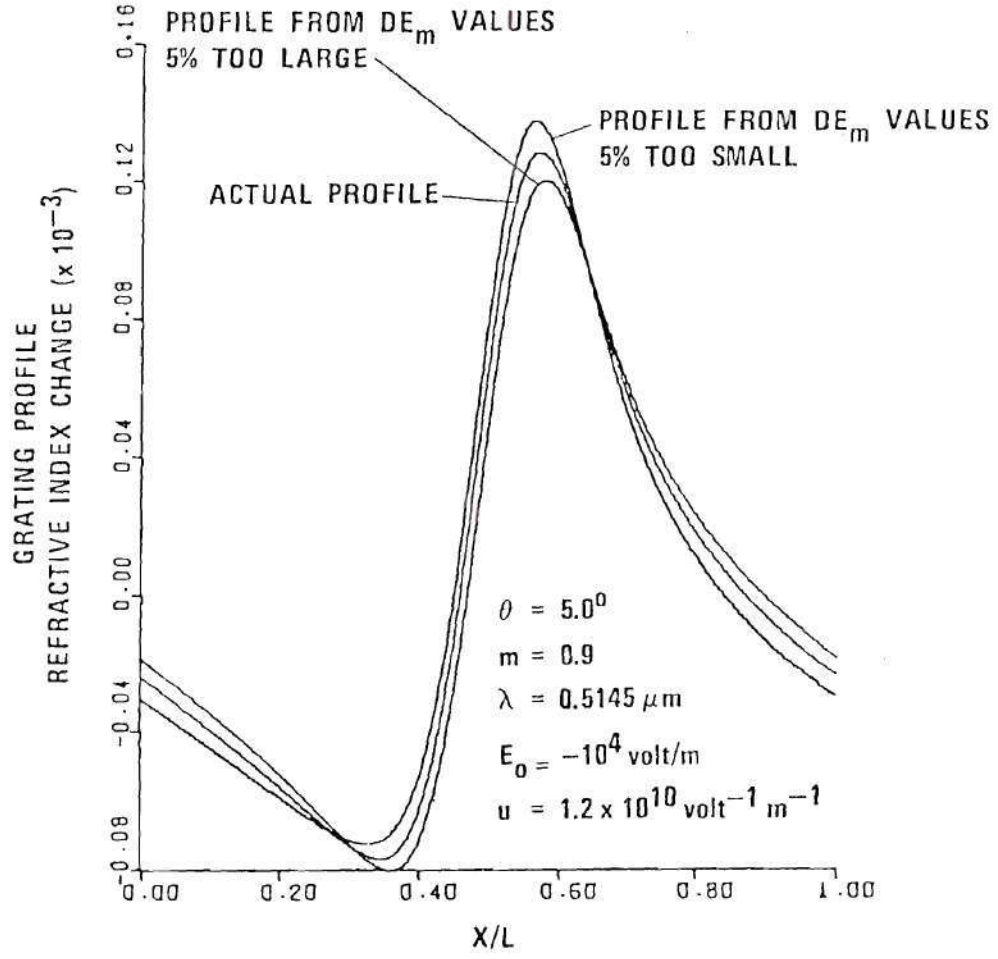

Figure 28. One Grating Period of the Refractive Index Profile Calculated from Diffraction Efficiencies That Are a) 5.0% Too Large and b) 5.0% Too Small Compared to the Actual Profile.

profile decreases with decreasing exposure parameters. If, instead of a systematic error of 5%, a random error of 2% is present, the calculated profile similarly approximates the actual profile. Figure 29 presents the grating profiles obtained from diffraction efficiencies with 2% random error. If the random error exceeds 2%, less accurate profiles will be obtained.

4.4.6 An Experimental Example

For illustration, the refractive index profile of a lithium niobate holographic grating is determined from measurements of its fundamental and higher-order diffraction efficiencies. The holographic grating was recorded in a 2.12-mm-thick 0.02 mole% Fe-doped lithium niobate crystal with the grating vector parallel to the c axis of the crystal. The hologram was written with a wavelength of 514.5 nm, a total power density of 8.77 mW/mm^2, external writing angle of $\pm$ 5.00°, a writing time of 187 sec, polarization in the plane of incidence, a modulation ratio of 0.994, and no applied electric field. Experimentally, the diffraction efficiencies were measured with a low power He-Ne laser (λ_r = 632.8 nm). The measured diffraction efficiencies are DE_1 = 21.6%, $DE_2 = 8.64 \times 10^{-2}$%, and $DE_3 = 7.74 \times 10^{-3}$%. When corrected by their corresponding transmittance factors the diffraction efficiencies become DE_1 = 29.7%, DE_2 = 0.123%, and $DE_3 = 1.08 \times 10^{-2}$%. These corrected diffraction efficiencies are then used in the procedure to determine the refractive index profile of the grating. By the method of least squares, the exposure parameter for this grating was found to be $u_p = 4.74 \times 10^8\ V^{-1}m^{-1}$ for $\varepsilon = 30\,\varepsilon_o$. The resultant refractive index profile is shown in Fig. 30. By fitting Eq. (72) to the profile in Fig. 30, it is found that the effective electric field during

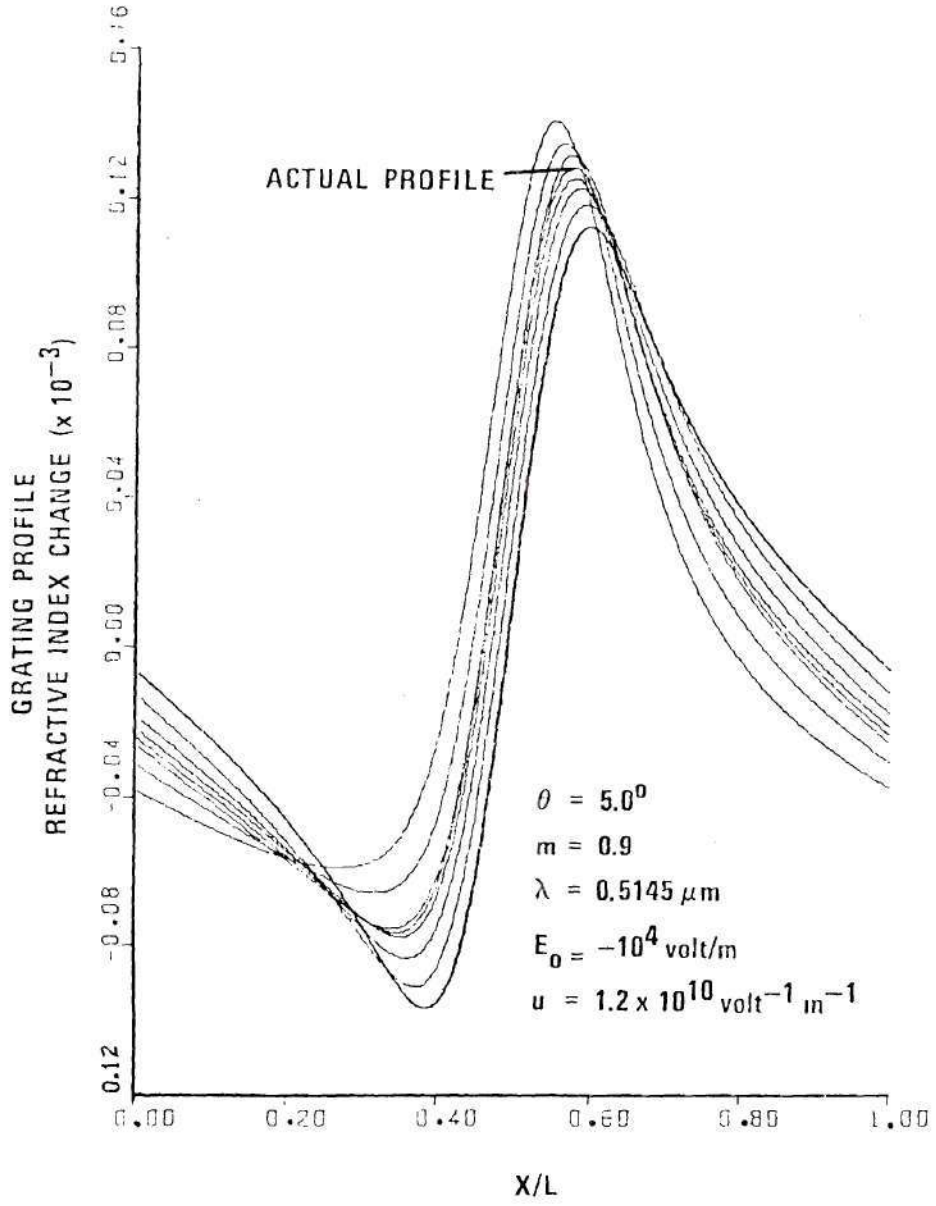

Figure 29. One Grating Period of the Refractive Index Profiles Calculated from Diffraction Efficiencies with 2% Random Error Compared to the Actual Profile.

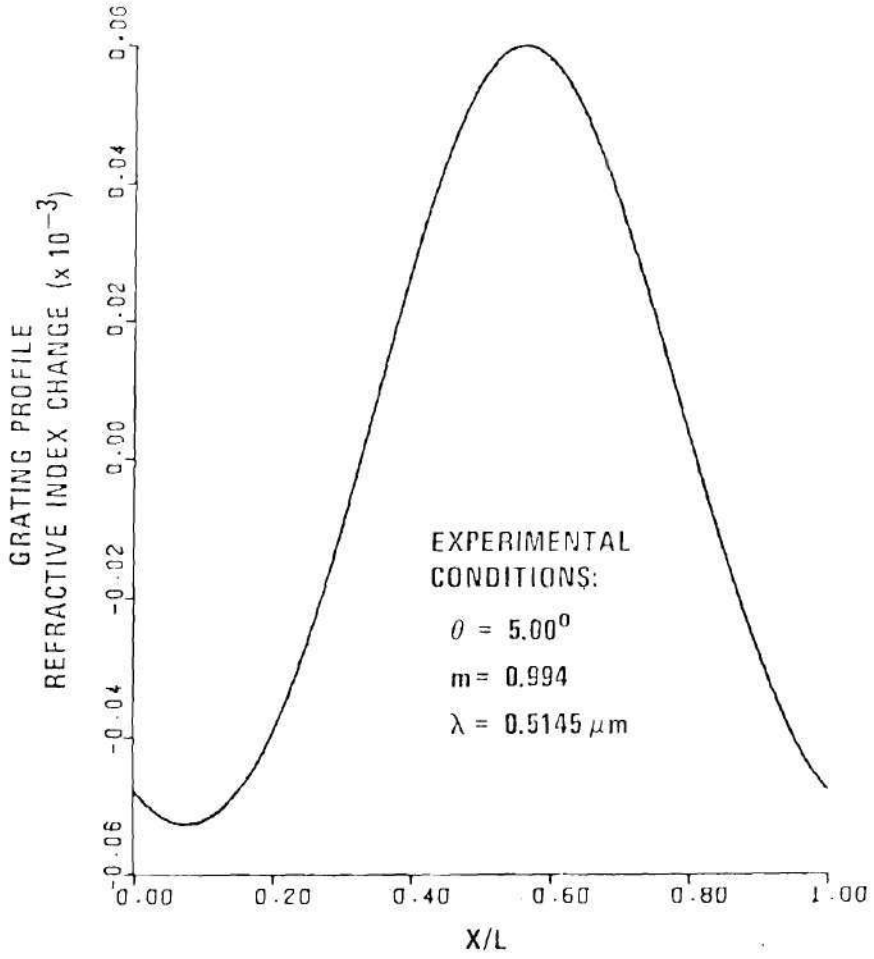

Figure 30. One Grating Period of the Refractive Index Profile of a Holographic Grating Recorded in a 2.12-mm-thick Iron-doped Lithium Niobate Crystal with No Applied Electric Field During Recording.

writing was $E_o = -1.06 \times 10^5$ V/m. This particular grating is nearly sinusoidal due to the relatively small exposure.

4.5 Discussion

Because the incident angle of the reading beam can not exceed 90.0^o, the number of higher-order Bragg angles available is limited to the integer that is nearest to, but less than $2L/\lambda_r$. If a suitably short wavelength source is available, the accessibility of higher-order Bragg angles is assured. However, the higher-order diffraction efficiencies are usually small and thus the first three or so orders of the diffraction efficiency are usually sufficient.

Although, in the foregoing analysis, the gratings are assumed to be generated through diffusion and drift of electrons, the method is equally applicable to gratings generated by holes. Electric field patterns produced by diffusion of holes are a mirror reflection about $x = 0$ of those produced by diffusion of electrons. The electric field patterns generated by drift of holes are the same as those generated by drift of electrons. Thus the drift electric field pattern is independent of the type of charge carrier.

In addition, the procedure presented in this chapter can also be applied to the case in which the reading beam is H mode polarized. It can be shown straightforwardly that the grating profiles determined by E mode and H mode polarizations are identical. Since any polarization can be decomposed into E and H modes, the grating profile can, therefore, be determined from diffraction efficiency data for any given polarization of the reading beam.

The phenomenon of birefringence must, in principle, also be taken

into account. In this case, the refractive index is a function of the angle of incidence and, therefore, the appropriate values of refractive index must be used in the foregoing procedure. However, for uniaxial crystal (such as lithium niobate), if the crystal is oriented in such a way that its optic axis is parallel to the x axis for the geometry used in this chapter, birefringence appears only in the case of E mode polarization. In addition, since the amplitude of the spatial modulation of the refractive index would be 10^{-4} or smaller, the error in determining the grating refractive index profile is negligible due to the very small variations in the birefringence at different Bragg angles. For example, in the case of lithium niobate at λ_r = 514.5 nm, changes in the amplitude of the fundamental grating do not exceed one tenth of 1% (using n_{sl} = $- 2.9 \times 10^{-5} n_0$ and $n_{cl} = - 2.1 \times 10^{-5} n_0$ with $n_0 = 2.337$ and $n_E = 2.243$, where n_0 and n_E are the principal indices of refraction for ordinary and extraordinary waves, respectively).

CHAPTER V

EXPERIMENTS AND DETERMINATION OF PHYSICAL MECHANISMS

5.1 Introduction

In this chapter, experimental measurements of the diffraction efficiencies of thick gratings in lithium niobate crystals are presented. From these diffraction efficiencies data, the refractive index profiles of the gratings are determined using the procedure described in Chapter IV. The effective electric field E_o in the crystal during hologram writing is then determined by best fitting of the theoretical space-charge electric field pattern [Eq. (72)] to the predicted grating profile using appropriate parameters and a scale factor. From the magnitudes of $(k_b T/e)K$ and E_o, the percentage amounts of diffusion and drift in the process of hologram writing are determined.

Three typical experiments have been conducted and the results are presented here. In the first experiment, no external electric field was applied during hologram recording. In the second experiment, a dc field equal to 1.06×10^5 V/m was applied in the -c axis direction during hologram recording. In the third experiment, an electric field of the same magnitude was applied in the +c axis direction during hologram recording. The grating profiles are determined for these gratings.

5.2 Experimental Set-up

The experimental set-up is shown in Fig. 31. An argon laser beam of 514.5 nm is split by the beam splitter into two beams (object and re-

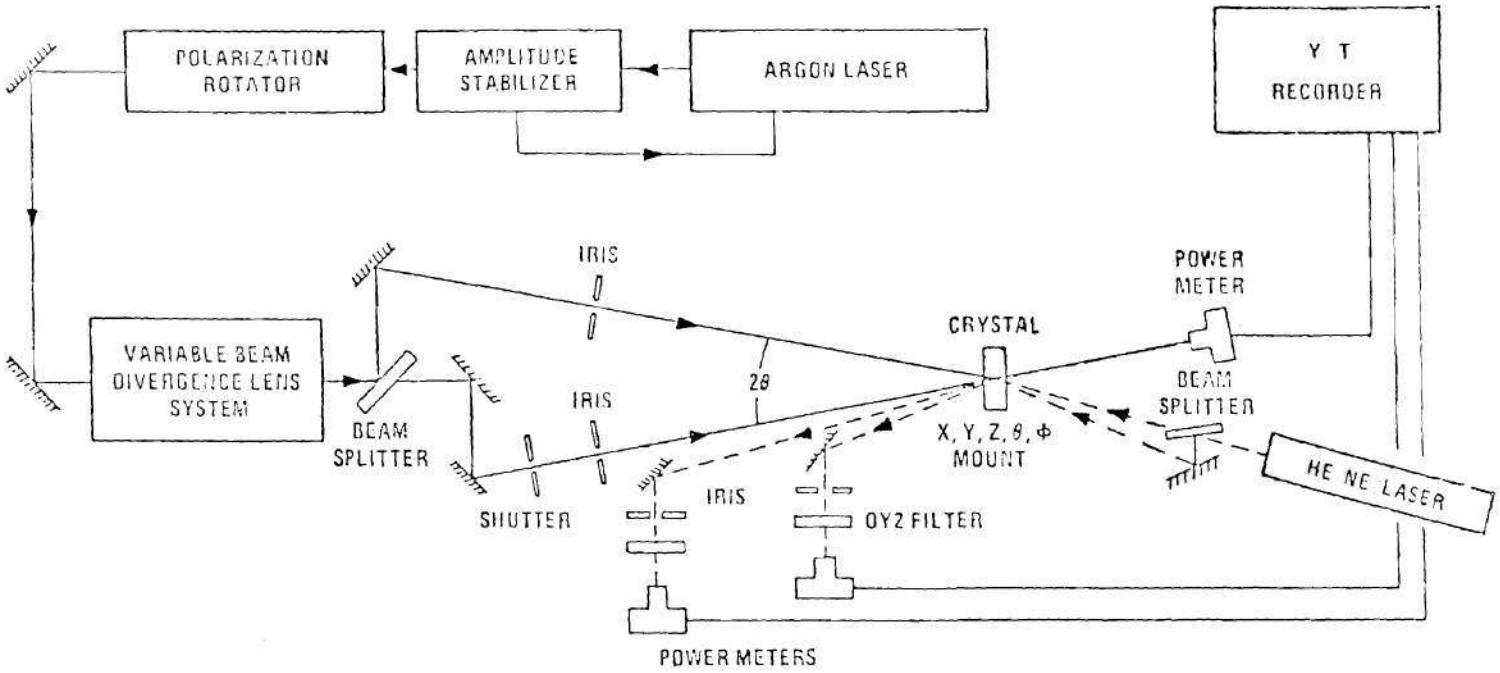

Figure 31. Experimental Set-up for Hologram Recording and Read-out.

ference beams), which are apertured to a diameter of 3.18 mm and impinge upon the iron doped lithium niobate crystal at an angle of $\pm$ 5.0°. The relative intensities of the two beams, which determine the beam modulation ratio m, can be controlled by means of a variable beam splitter. The beams are polarized in the plane of incidence. The width of the crystal between +c and -c edges is 10 mm and its thickness is 2.12 mm. The crystal is oriented such that its c axis is parallel to the plane of incidence with the +c axis direction in the +x reference direction. By means of electrodes placed at +c and -c edges of the crystal, a voltage of up to 10 kV (correspoding to an electric field of 10^6 V/m) could be applied. After recording, a lower power HeNe laser beam, also polarized in the plane of incidence, was used at its appropriate Bragg angles to measure the fundamental and the higher-order diffraction efficiencies. The light intensities, the beam modulation ratio, the recording angle, and the applied electric field can be varied at will.

5.3 Experiments — Hologram Recording and Read-out

5.3.1 Experiment 1: No Applied Electric Field During Hologram Recording

In this experiment, the hologram was recorded without an externally applied electric field during recording. The experimental conditions were presented in Section 4.4.6 and the resultant refractive index profile was shown in Fig. 30.

5.3.2 Experiment 2: Applied Electric Field in the -c Axis Direction

From Experiment 1, the effective electric field E_o was found to be 1.06×10^5 V/m directed in the -c direction. Therefore, in this experiment, a voltage of 1.06 kV was applied to the electrode on the +c edge (producing an electric field of 1.06×10^5 V/m in the -c axis direction)

during hologram recording. The hologram was recorded in different part of the crystal in order not to interfere with the hologram recorded in Experiment 1. The hologram was written with a total power density of 8.75 mw/mm^2, a writing time of 186 sec, and a modulation ratio of 0.992. The measured diffraction efficiencies are $DE_1 = 16.6\%$, $DE_2 = 8.91 \times 10^{-2}\%$, and $DE_3 = 9.14 \times 10^{-4}\%$. When corrected by their corresponding transmittance factors, the diffraction efficiencies become $DE_1 = 22.8\%$, $DE_2 = 0.127\%$, and $DE_3 = 1.28 \times 10^{-3}\%$. By the method of least squares, the exposure parameter for this grating was found to be $u_p = 4.70 \times 10^8$ $V^{-1}m^{-1}$ for $\varepsilon = 30\varepsilon_o$. The resultant refractive index profile for this grating is shown in Fig. 32. By fitting Eq. (72) to the profile in Fig. 32, it is found that the effective electric field E_o was -2.05×10^5 V/m (directed in the -c axis direction). This reveals that when an electric field of 1.06×10^5 V/m is applied in the -c axis direction the magnitude of the effective electric field is doubled. In this case, the drift component doubles its strength while the diffusion component remains unchanged and, therefore, as can be seen from Fig. 32, the peak of the grating profile shifts towards the x = 0 axis (the peak of the grating profile is exact on the x = 0 axis for pure drift case).

5.3.3 Experiment 3: Applied Electric Field in the +c Axis Direction

In this experiment, a voltage of -1.06 kV was applied in the -c axis direction (producing an electric field of 1.06×10^5 V/m in the +c axis direction) during hologram recording. The total power density of the writing beams is 8.48 mw/mm^2. The writing time is 185 sec and the writing beam modulation ratio is 0.989. The measured diffraction efficiencies are $DE_1 = 16.1\%$, $DE_2 = 6.48 \times 10^{-2}\%$, and $DE_3 = 1.25 \times 10^{-3}\%$.

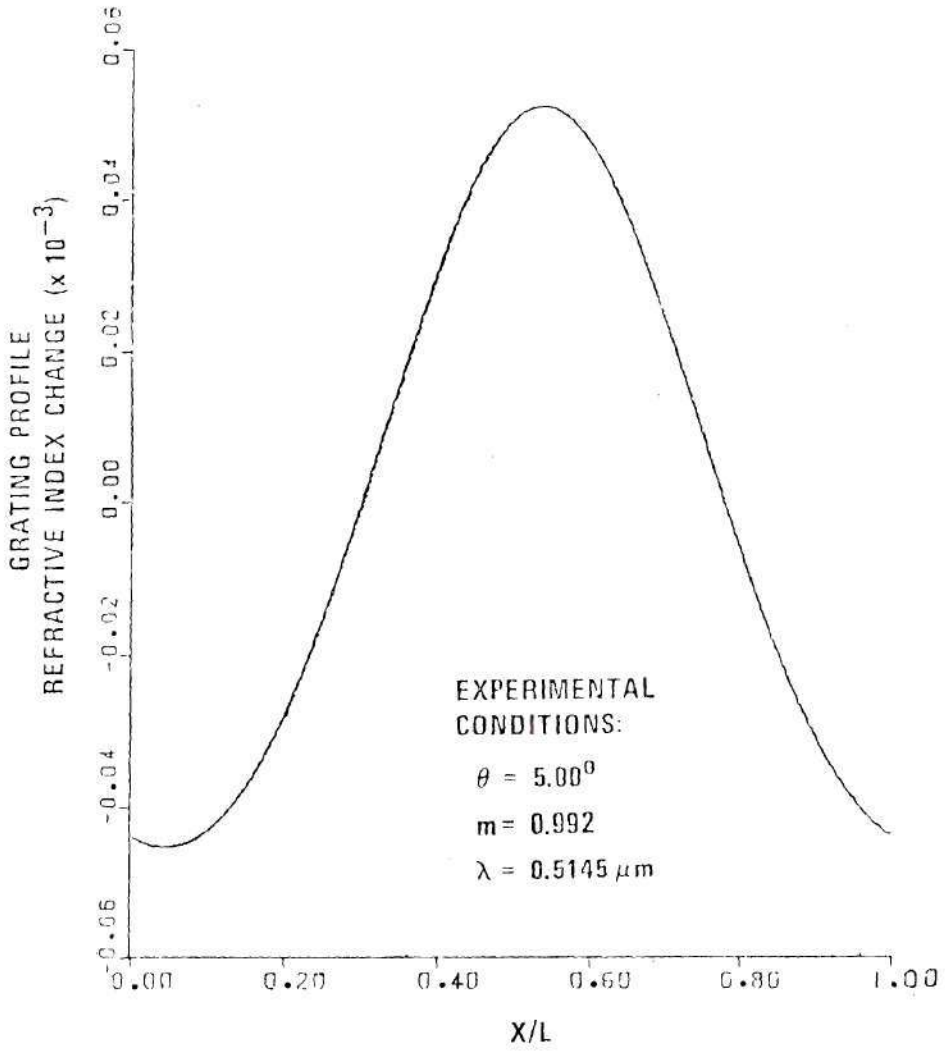

Figure 32. One Grating Period of the Refractive Index Profile of a Holographic Grating Recorded in a 2.12-mm-thick Iron-doped Lithium Niobate Crystal with an Electric Field of 1.06×10^5 V/m Applied in the -c Axis Direction.

The corrected diffraction efficiencies are $DE_1 = 22.2\%$, $DE_2 = 9.26 \times 10^{-2}\%$, and $DE_3 = 1.75 \times 10^{-3}\%$. By the method of least squares, the exposure parameter for this grating was found to be $4.53 \times 10^8\ V^{-1}m^{-1}$. The resultant refractive index profile of this grating is shown in Fig. 33. Again, by fitting Eq. (72) to the grating profile in Fig. 33, the effective electric field was found to be $E_o = -9.00 \times 10^3$ V/m (directed in the -c axis direction). This shows that when an electric field of 1.06×10^5 V/m is applied in the +c axis direction, the effective electric field is almost cancelled by the applied field. In this case, the drift component becomes very small compared to the diffusion component and therefore, as shown in Fig. 33, the peak of the grating profile shifts away from the x = 0 axis.

5.4 Determination of Physical Mechanisms

From Eq. (72), the percentage amounts of diffusion and drift in the process of hologram recording are

$$\text{Diffusion} = (k_b T/e)K/\left[(k_b T/e)K + E_o\right] \times 100\%, \tag{90}$$

and

$$\text{Drift} = E_o/\left[(k_b T/e)K + E_o\right] \times 100\%. \tag{91}$$

Equations (90) and (91) are independent of material parameters and type of charge carriers. Using Eqs. (90) and (91), the percentage amounts of diffusion and drift in the recording process can be calculated for any experimental conditions, provided that the effective electric field E_o is known. As mentioned earlier, the value of E_o can be obtained by fitting Eq. (72) to the grating profile determined from the measured diffraction efficiency data. Therefore, the percentage amounts of diffusion and

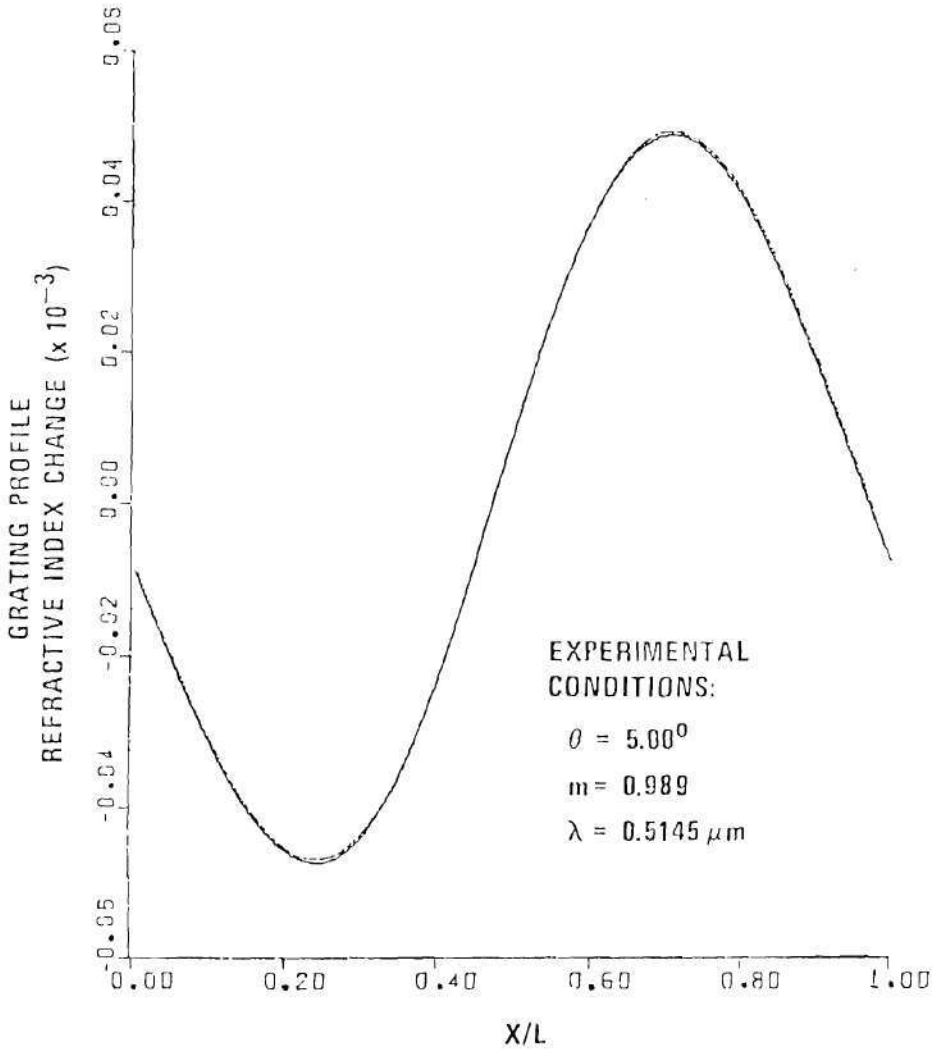

Figure 33. One Grating Period of the Refractive Index Profile of a Holographic Grating Recorded in a 2.12-mm-thick Iron-doped Lithium Niobate Crystal with an Electric Field of 1.06×10^5 V/m Applied in the +c Axis Direction.

drift in the recording process of a hologram can be determined by measurements of the fundamental and the higher-order diffraction efficiencies of the grating.

The experiments presented in the preceding section were conducted at room temperature. Therefore, according to the experimental conditions described in Section 5.2, the value of $(k_b T/e)K$ is 5.5×10^4 V/m. Since the value of E_o for each experiment has been found, the percentage amounts of diffusion and drift in these experiments can be determined. They are listed in Table 11.

Table 11. Percentage Amounts of Diffusion and Drift for Different Experiments.

Experiment	Diffusion	Drift
1	34%	66%
2	21%	79%
3	86%	14%

5.5 Discussion

The front and back surfaces of the lithium niobate crystal used in the experiments are not perfectly parallel. The angle between these two surfaces was found to be 0.124^o (446.55 arc sec). In addition, a reflectance test of the crystal also shows that there is no periodic variation in the reflected power. Therefore, the use of the complicated transmittance factor expression [Eq. (34)] is waived. The transmittance factors used in the preceding section to correct the diffraction effici-

encies were obtained by practical measurements of the transmitted powers before recording. The measured values of these factors are very close to those obtained via Eq. (89).

In the preceding section, the effect of birefringence has been taken into account since the diffraction efficiencies were measured with E-mode polarization beams. The average refractive index used at each Bragg angle was obtained by the equation[57]

$$n_o(\theta_m) = n_O n_E / [(n_O)^2 \sin^2(\theta_m) + (n_E)^2 \cos^2(\theta_m)]^{\frac{1}{2}}, \qquad (92)$$

where $n_O = 2.337$ and $n_E = 2.243$ are the principal indices of refraction for ordinary and extraordinary waves, respectively.

CHAPTER VI

CONCLUSIONS AND RECOMMENDATIONS

This dissertation is a culmination of a research effort on the determination of grating shape and physical mechanisms in lithium niobate holographic recording. A four part research program has been conducted. The first part of this research program was the calculation of arbitrary-order diffraction efficiencies of thick gratings with arbitrary grating shape. The second part of this research program was the investigation of the relationship between the grating shape and the physical mechanisms (diffusion and drift of charge carriers). The third part of this research program was the reverse problem of the first part: development of a procedure to determine the grating profile from the fundamental and the higher-order diffraction efficiencies of the grating. The forth and last part of this research program was experimental application of these techniques to a lithium niobate crystal. From the grating profiles determined from the measured diffraction efficiencies, the physical mechanisms are quantified. The main results of the complete research effort can be summarized as follows:

1. Calculation of Arbitrary-order Diffraction Efficiencies of Thick Gratings with Arbitrary Grating Shape. A method for calculating arbitrary-order diffraction efficiencies of thick, lossless transmission gratings with arbitrary periodic grating shapes has been developed. This represents an extension of previous work to nonsinusoidal gratings and

to higher-order Bragg angles. A Fourier-series representation of the grating is employed, along with a coupled-wave theory of diffraction. For illustration, numerical values of the diffraction efficiencies at the first three Bragg angles are calculated for sinusoidal, square-wave, triangular, and saw-tooth gratings. Numerical results for the same grating shapes with the same parameters are also calculated for comparison, by extending Burckhardt's numerical method for analyzing thick sinusoidal gratings. The comparison shows that the coupled-wave theory provides results with relative computational ease and results that are in agreement with calculations *obtained* by extending the more-rigorous Burckhardt's theory to nonsinusoidal grating shapes and to higher-order Bragg angles.

2. Grating Shape and Physical Mechanisms in Lithium Niobate Holographic Recording. The description of the formation of thick-phase holograms over the entire range of exposure has been accomplished using numerical methods. The space-charge field patterns (and thus the refractive index profiles for lithium niobate crystals) generated through diffusion and drift of charge carriers are calculated. The treatment allows for the presence of an effective electric field due to the photovoltaic effect and an externally applied electric field. The results of this approach agree with those of the analytical approaches in Refs. 47 and 48.

3. Determination of Grating Shape by Diffraction Efficiencies. An infinite variety of refractive index profiles (grating shapes) may result when lithium niobate crystals are exposed to the interference pattern of two intersecting plane light waves. The grating shapes produced depend on the details of the exposure and the physical processes that are operative in the crystals. A method for determining the refractive index

profile of unknown thick optically-induced phase gratings in lithium niobate crystals has been developed. This method, based on the coupled-wave theory, requires a knowledge of the fundamental and the higher-order diffraction efficiencies of the grating. The physical mechanisms through which the gratings were generated are assumed to be diffusion and drift of electrons. The procedure allows for the presence of an effective electric field due to the bulk photovoltaic effect and an externally applied electric field. The calculational accuracy of the procedure is tested by determining the refractive index profiles from the calculated diffraction efficiencies of known grating profiles. Comparison of the resultant calculated refractive index profiles to the original profiles verifies that this calculational method is very accurate. As an illustration of the procedure, the refractive index profile of a lithium niobate holographic grating is determined from measurements of its fundamental and higher order diffraction efficiencies.

4. Experiments and Determination of Physical Mechanisms. Three typical experiments with different experimental conditions have been conducted. In the first experiment, no external field was applied to the crystal during recording. In the second experiment, an electric field of 1.06×10^5 V/m was applied in the -c axis direction during recording. In the third experiment, an electric field of the same magnitude was applied in the +c axis direction during recording. The holograms in these three experiments were recorded in different parts of the crystal. The grating profiles of these gratings as well as the percentage amounts of diffusion and drift in the process of recording have been determined.

Some possibilities for extensions are apparent. The gratings

considered in this dissertation are lossless transmission gratings. However, the techniques presented in this dissertation, with some modification, can also be applied to lossy gratings as well as reflection gratings. In addition, the diffusion length of the photoexcited electrons has been assumed to be very short compared to the grating period. This assumption can be removed by using the continuity equation[29] $\partial n/\partial t = g - n/\tau + (1/e)\,\partial J/\partial x$, where g is the local generation rate. In this case, it is impossible to analyze the formation of phase holograms for the entire exposure range by analytic methods. However, the numerical approach in Chapter III of this dissertation can be extended to cover this case without difficulty.

APPENDIX

CALCULATION OF DIFFRACTION EFFICIENCIES BY A NUMERICAL METHOD

This appendix extends Burckhardt's numerical solution for diffraction from a sinusoidal phase grating to a nonsinusoidal phase grating. The solutions for both H-mode and E-mode polarizations are obtained and presented.

1. H-Mode Solution

The geometrical configuration used here is the same as the grating and coordinate system shown in Fig. 1 in Chapter II. The H-mode wave equation again is

$$\left[\nabla^2 + k^2 \varepsilon_r(x)\right] E(x,z) = 0. \tag{A-1}$$

The spatial distribution of the relative dielectric constant as given by Eq. (1) can be rewritten as

$$\varepsilon_r(x) = \sum_{h=-\infty}^{\infty} \hat{\varepsilon}_h \, e^{jhKx}, \tag{A-2}$$

where

$$\hat{\varepsilon}_h = \begin{cases} (\varepsilon_{ch} - j\varepsilon_{sh})/2 & \text{for} \quad h > 0, \\ \varepsilon_{ro} & \text{for} \quad h = 0, \\ (\varepsilon_{c|h|} + j\varepsilon_{s|h|})/2 & \text{for} \quad h < 0. \end{cases} \tag{A-3}$$

By assuming a solution of the form,

$$E(x,z) = X(x)Z(z), \tag{A-4}$$

we obtain the following equations

$$\frac{d^2Z}{dz^2} - a^2Z = 0, \tag{A-5}$$

$$\frac{d^2X}{dx^2} + \left(a^2 + k^2 \sum_{h=-\infty}^{\infty} \hat{\varepsilon}_h e^{jhKx} \right) X = 0, \tag{A-6}$$

where a^2 is the separation constant. The solution of Eq. (A-5) is

$$Z(z) = Ae^{az} + A'e^{-az}, \tag{A-7}$$

where A and A' are determined from the boundary conditions and a is determined from an eigenvalue problem. Equation (A-6) is Hill's equation, and its general solution is

$$X(x) = \sum_{h=-\infty}^{\infty} b_h e^{j(k\sin\theta + hK)x}. \tag{A-8}$$

Inserting Eq. (A-8) into Eq. (A-6), we get the following matrix equation

$$DB = a^2B, \tag{A-9}$$

where B is a column vector with $B^T = [\cdots\ b_{-3}\ b_{-2}\ b_{-1}\ b_0\ b_1\ b_2\ b_3\ \cdots]$

and D is an infinite hermitian matrix given as

$$D = \begin{bmatrix} \cdots & \cdots & \cdots & \cdots & \cdots & \cdots \\ r & \hat{\varepsilon}_1 & \hat{\varepsilon}_2 & \hat{\varepsilon}_3 & \cdots & \cdots \\ \hat{\varepsilon}_{-1} & r & \hat{\varepsilon}_1 & \hat{\varepsilon}_2 & \hat{\varepsilon}_3 & \cdots \\ \hat{\varepsilon}_{-2} & \hat{\varepsilon}_{-1} & r & \hat{\varepsilon}_1 & \hat{\varepsilon}_2 & \hat{\varepsilon}_3 \\ \hat{\varepsilon}_{-3} & \hat{\varepsilon}_{-2} & \hat{\varepsilon}_{-1} & r & \hat{\varepsilon}_1 & \hat{\varepsilon}_2 \\ \cdots & \hat{\varepsilon}_{-3} & \hat{\varepsilon}_{-2} & \hat{\varepsilon}_{-1} & r & \hat{\varepsilon}_1 \\ \cdots & \cdots & \hat{\varepsilon}_{-3} & \hat{\varepsilon}_{-2} & \hat{\varepsilon}_{-1} & r \\ \cdots & \cdots & \cdots & \cdots & \cdots & \cdots \end{bmatrix}, \qquad \text{(A-10)}$$

where $r = -k^2\hat{\varepsilon}_0 + (k \sin\theta + hK)^2 = -k^2\varepsilon_{ro} + (k \sin\theta + hK)^2$. Eq. (A-9) is similar in form to Eq. (9) of Ref. 31. The only difference is that the matrix D in Eq. (A-9) here is Hermitian whereas the matrix in Eq. (9) of Ref. 31 is symmetric with real elements. Kaspar[36] has treated the case in which the matrix D is symmetric with complex elements.

Equation (A-9) has nontrivial solutions only when a^2 is an eigenvalue. To each a_i^2 there corresponds an eigenvector B_i with elements $b_{h,i}$, where $b_{h,i}$ designates the h th component of the i th eigenvector B_i. For the computation of the eigenvalues a_i^2 and the eigenvector B_i, the infinite matrix D in Eq. (A-9) must be truncated. A discussion on this problem has been given by Burckhardt.[31] In general, better accuracy is obtained when a larger matrix is used. However, larger matrices will usually produce numbers which are too large or too small for a digital computer to handle. In the calculations of the results in Tables 6 and 7, the matrix D was truncated to become a 6x6 matrix. The field inside

the grating is the summation of the individual solution for each a_i. That is,

$$E(x,z) = \sum_i \{ [A_i \exp(a_i z) + A_i' \exp(-a_i z)] \times \sum_h b_{h,i} \exp\, j(k \sin\theta + hK)x \} . \quad \text{(A-11)}$$

The method for determining A_i and A_i' is identical to that described by Burckhardt[31] and, therefore, will not be repeated here. The electric field amplitude of any order at the right hand side boundary of Fig. 1 in Chapter II is

$$E_h(d) = \sum_i [A_i \exp(a_i d) + A_i' \exp(-a_i d)] b_{h,i} . \quad \text{(A-12)}$$

The h th-order diffraction efficiency is defined as

$$DE_h = \frac{E_h(d)\, E_h^*(d)}{E_o(0)\, E_o^*(0)} , \quad \text{(A-13)}$$

where $E_o(0)$ is the electric field amplitude of the incident wave. Therefore, the h th-order diffraction efficiency can be obtained by simply inserting Eq. (A-12) into Eq. (A-13).

2. E-Mode Solution

Recall that E-mode is the mode for which the electric field is parallel to the x-z plane and the magnetic field ia parallel to the y

axis. The solution for this mode goes along the same line as that of H-mode. However, since the second term in Eq. (35) in Chapter II does not vanish, there are some additional problems. In this case it is simpler to solve for the magnetic field strength H because H has only one component, which points in the y direction. The wave equation for $\vec{H}$ is

$$\nabla^2\vec{H} + \nabla\varepsilon_r \times (\frac{1}{\varepsilon_r} \nabla \times \vec{H}) + k^2\varepsilon_r\vec{H} = 0. \tag{A-14}$$

Letting

$$\vec{H} = H(x,z)\hat{y}, \tag{A-15}$$

where $\hat{y}$ is the unit vector in the y direction, we obtain

$$\nabla^2 H - \frac{1}{\varepsilon_r}\frac{d\varepsilon_r}{dx}\frac{\partial H}{\partial x} + k^2\varepsilon_r H = 0. \tag{A-16}$$

By setting

$$H(x,z) = X(x)Z(z), \tag{A-17}$$

we have the following equations

$$\frac{d^2Z}{dz^2} - a^2Z = 0, \tag{A-18}$$

$$\frac{d^2X}{dx^2} - \frac{1}{\varepsilon_r}\frac{d\varepsilon_r}{dx}\frac{dX}{dx} + (k^2\varepsilon_r + a^2)X = 0, \tag{A-19}$$

where a^2, again, is the separation constant. Equation (A-18) is identical to Eq. (A-5), and its solution is given by Eq. (A-7). Our task now is to solve Eq. (A-19). Inserting Eq. (A-2) into Eq. (A-19) gives

$$\frac{d^2X}{dx^2} - \left\{ \left[\sum_{h=-\infty}^{\infty} jhK\hat{\varepsilon}_h \exp(jhKx) \right] / \left[\sum_{h=-\infty}^{\infty} \hat{\varepsilon}_h \exp(jhKx) \right] \right\} \frac{dX}{dx}$$

$$+ \left\{ k^2 \left[\sum_{h=-\infty}^{\infty} \hat{\varepsilon}_h \exp(jhKx) \right] + a^2 \right\} X = 0. \qquad \text{(A-20)}$$

If we solve Eq. (A-20) the same way as we solved Eq. (A-6), the matrix in the resultant matrix equation is no longer Hermitian. Some additional complications are encountered during the process of evaluating the eigenvalues. Therefore, in order to avoid any unnecessary complications, we do not solve Eq. (A-20) directly but make a substitution that leads to a Hermitian matrix and then solve the resulting new equation. The substitution is made as follows. Let

$$U(x) = X(x) / \left[\sum_{h=-\infty}^{\infty} \hat{\varepsilon}_h \exp(jhKx) \right]^{\frac{1}{2}}, \qquad \text{(A-21)}$$

then, Eq. (A-20) becomes

$$\frac{d^2U}{dx^2} + \left[f(x) + a^2 \right] U = 0, \qquad \text{(A-22)}$$

where

$$f(x) = k^2 \sum_{h=-\infty}^{\infty} \hat{\varepsilon}_h \exp(jhKx) - \frac{1}{2} \left[K^2 \sum_{h=-\infty}^{\infty} h^2 \hat{\varepsilon}_h \exp(jhKx) \right] / \left[\sum_{h=-\infty}^{\infty} \hat{\varepsilon}_h \exp(jhKx) \right]$$

$$+ \frac{3}{4} K^2 \Big[\sum_{h=-\infty}^{\infty} h^2 \hat{\varepsilon}_h \exp(jhKx) \Big]^2 / \Big[\sum_{h=-\infty}^{\infty} \hat{\varepsilon}_h \exp(jhKx) \Big]^2. \qquad \text{(A-23)}$$

Equation (A-23) can be rewritten as a Fourier series

$$f(x) = \sum_{p=-\infty}^{\infty} c_p \exp(jpKx), \qquad \text{(A-24)}$$

where c_p are the complex Fourier coefficients which can be calculated by

$$c_p = \frac{K}{2\pi} \int_{-\pi/K}^{\pi/K} f(x) \exp(-jpKx)\, dx, \qquad \text{(A-25)}$$

or

$$c_p = \frac{1}{L} \int_{-L/2}^{L/2} f(x) \exp\left[-jp(2\pi/L)x\right] dx. \qquad \text{(A-26)}$$

Equation (A-22) has the form of Hill's equation. Therefore, as in the case of H-mode solution, the general solution of Eq. (A-22) is

$$U(x) = \sum_{h=-\infty}^{\infty} b_h \exp\left[j(k \sin\theta + hK)x\right]. \qquad \text{(A-27)}$$

Substituting Eqs. (A-24) and (A-27) into Eq. (A-22), we have the following matrix equation

$$DB = a^2 B, \qquad \text{(A-28)}$$

where B, again, is a column vector with $B^T = [\cdots\ b_{-3}\ b_{-2}\ b_{-1}\ b_0\ b_1\ b_2\ \cdots]$ and D is an infinite Hermitian matrix given by

$$D = \begin{bmatrix} \cdots & \cdots & \cdots & \cdots \\ (k\sin\theta-2K)^2-c_0 & -c_{-1} & -c_{-2} & -c_{-1} \\ -c_1 & (k\sin\theta-K)^2-c_0 & -c_{-1} & -c_{-2} \\ -c_2 & -c_1 & (k\sin\theta)^2-c_0 & -c_{-1} \\ -c_3 & -c_2 & -c_1 & (k\sin\theta+K)^2-c_0 \\ \cdots & \cdots & \cdots & \cdots \end{bmatrix}. \qquad \text{(A-29)}$$

Again, Eq. (A-28) has nontrivial solutions only when a^2 is an eigenvalue. The matrix D in Eq. (A-28) must be truncated in practical calculations. In the calculations of the results listed in Tables 8 and 9, the matrix D used was a 6x6 matrix. From Eq. (A-17) we then have the magnetic field strength $H(x,z)$ in the grating

$$H(x,z) = X(x)Z(z)$$

$$= \left[\sum_{p=-\infty}^{\infty} \hat{\epsilon}_p \exp(jpKx)\right]^{\frac{1}{2}} \times \sum_i \left\{\left[A_i \exp(a_i z) + A_i' \exp(-a_i z)\right]\right.$$

$$\left. \times \sum_h b_{h,i} \exp\left[j(k\sin\theta + hK)x\right]\right\}, \qquad \text{(A-30)}$$

where again A_i and A_i' are constants which must be determined from the boundary conditions. The method for determining A_i and A_i' is the same as that given in Ref. 31 and is omitted here. Compared to the H-mode solution, there is an additional difficulty in obtaining the field amplitudes

H_h of various orders because of the presence of the first factor on the right-hand side of Eq. (A-30). To avoid this difficulty we write the first factor on the right-hand side of Eq. (A-30) as a Fourier series

$$\left[\sum_{p=-\infty}^{\infty} \hat{\varepsilon}_p \exp(jpKx)\right]^{\frac{1}{2}} = \sum_{m=-\infty}^{\infty} \gamma_m \exp(jmKx), \tag{A-31}$$

where the Fourier coefficient γ_m can be evaluated by use of Eq. (A-25) or Eq. (A-26) with f(x) replaced by the factor on the left-hand side of Eq. (A-31). Inserting Eq. (A-31) into Eq. (A-30) we obtain

$$H(x,z) = \sum_i \left\{ \left[A_i \exp(a_i z) + A_i' \exp(-a_i z) \right] \right.$$

$$\left. \times \sum_h \Gamma_{h,i} \exp\, j(k \sin\theta + hK)x \right] \Big\}, \tag{A-32}$$

with

$$\Gamma_{h,i} = \sum_m \gamma_{-m}\, b_{h+m,i}. \tag{A-33}$$

The h th-order field amplitude at the right-hand side boundary of Fig. 1 is

$$H_h(d) = \sum_i \left[A_i \exp(a_i d) + A_i' \exp(-a_i d) \right] \Gamma_{h,i}, \tag{A-34}$$

and the h th-order diffraction efficiency is given by Eq. (A-13) but with E replaced by H.

BIBLIOGRAPHY

1. D. Gabor, "A New Microscopic Principle," Nature, vol. 161, pp. 777-778, May 1948.

2. E. N. Leith and J. Upatnieks, "Reconstructed Wavefronts and Communication Theory," Journal of the Optical Society of America, vol. 52, pp. 1123-1130, October 1962.

3. E. N. Leith and J. Upatnieks, "Wavefront Reconstruction with Continuous-Tone Objects," Journal of the Optical Society of America, vol. 53, pp. 1377-1381, December 1963.

4. E. N. Leith and J. Upatnieks, "Wavefront Reconstruction with Diffused Illumination and Three-Dimensional Objects," Journal of the Optical Society of America, vol. 54, pp. 1295-1301, November 1964.

5. Y. N. Denisyuk, "On the Reproduction of the Optical Properties of an Object by the Wave Field of Its Scattered Radiation," Optics and Spectroscopy, vol. 15, pp. 279-284. October 1963.

6. P. J. van Heerden, "Theory of Optical Information Storage in Solid," Applied Optics, vol. 2, pp. 393-400, April 1963.

7. K. S. Pennington and L. H. Lin, "Multicolor Wavefront Reconstruction," Applied Physics Letters, vol. 7, pp. 56-57, August 1, 1965.

8. G. W. Stroke and A. E. Labeyrie, "White-light Reconstruction of Holographic Images Using the Lippmann-Bragg Diffraction Effect," Physics Letters, vol. 20, pp. 368-370, March 1966.

9. H. Kogelnik, "Coupled-wave Theory for Thick Hologram Gratings," The Bell System Technical Journal, vol. 48, No. 9, pp. 2909-2947, November 1969.

10. M. R. B. Forshaw, "Thick Holograms: A survey," Optics and Laser Technology, vol. 6, pp. 28-35, February 1974.

11. B. H. Crawford, "The Preparation of Ultra-fine Grain Photographic Emulsions," Journal of Scientific Instruments, vol. 31, pp. 333-335, September 1954.

12. J. N. Latta and R. C. Fairchild, "Two-element Hologram Telescope Lens," Journal of the Optical Society of America, vol. 63, p. 487, March 1973.

BIBLIOGRAPHY (Continued)

13. R. Shubert and J. H. Harris, "Optical Guided-wave Focusing and Diffraction," Journal of the Optical Society of America, vol. 61, pp. 154-161, February 1971.

14. H. Kogelnik and C. V. Shank, "Stimulated Emission in a Periodic Structure, "Applied Physics Letters, vol. 18, pp. 152-154, February 15, 1971.

15. I. P. Kaminow, H. P. Weber, and E. A. Chandross, "Poly (methyl methacrylate) Dye Laser with Internal Diffraction Grating Resonator," Applied Physics Letters, vol. 18, pp. 497-499, June 1, 1971.

16. H. Kogelnik and T. P. Sosnowski, "Holographic Thin-film Couplers," The Bell System Technical Journal, vol. 49, pp. 1602-1608, September, 1970.

17. M. L. Dakss, L. Kuhn, P. F. Heidrich, and B. A. Scott, "Grating Coupler for Efficient Excitation of Optical Guided Waves In Thin Films," Applied Physics Letters, vol. 16, pp. 523-525, June 15, 1970.

18. J. M. Hammer, "Digital Electro-optic Grating Deflector and Modulator," Applied Physics Letters, vol. 18, pp. 147-149, February 15, 1971.

19. T. K. Gaylord, "The High Capacity Storage Problem: Is Optical Holography the Answer?" Optical Spectra, vol. 6, pp. 25-37, November 1972.

20. L. d'Auria, J. P. Huignard, C. Slezak, and E. Spitz, "Experimental Holographic Read-write Memory Using 3-D storage," Applied Optics, vol. 13, pp. 808-818, April 1974.

21. T. K. Gaylord and F. K. Tittel, "Angular Selectivity of Lithium Niobate Volume Holograms," Journal of Applied Physics, vol. 44, pp. 4771-4773, October 1973.

22. J. J. Amodei and D. L. Staebler, "Holographic Recording in Lithium Niobate," RCA Review, vol. 33, pp. 71-93, March 1972.

23. D. L. Staebler and W. Phillips, "Fe-doped $LiNbO_3$ for Read-write Applications," Applied Optics, vol. 13, pp. 788-794, April 1974.

24. F. S. Chen, "Optically Induced Change of Refractive Index in $LiNbO_3$ and $LiTaO_3$," Journal of Applied Physics, vol. 40, pp. 3389-3396, July 1969.

BIBLIOGRAPHY (Continued)

25. W. D. Johnston, Jr., "Optical Index Damade in $LiNbO_3$ and Other Pyroelectric Insulators," Journal of Applied Physics, vol. 41, pp. 3279-3285, July 1970.

26. J. J. Amodei, "Electron Diffusion Effects During Hologram Recording in Crystals," Applied Physics Letters, vol. 18, pp. 22-24, January 1, 1971.

27. A. M. Glass, D. von der Linde, and T. J. Negran, "High-voltage Bulk Photovoltaic Effect and the Photorefractive Process in $LiNbO_3$," Applied Physics Letters, vol. 25, pp. 233-235, August 15, 1974.

28. J. J. Amodei, "Analysis of Transport Process During Holographic Recording in Insulators," RCA Review, vol. 32, pp. 185-199, June 1971.

29. L. Young, W. K. Y. Wong, M. L. W. Thewalt, and W. D. Cornish, "Theory of Formation of Phase Holograms in Lithium Niobate," Applied Physics Letters, vol. 24, pp. 264-265, March 15, 1974.

30. S. F. Su and T. K. Gaylord, "Calculation of Arbitrary-order Diffraction Efficiencies of Thick Gratings with Arbitrary Grating Shape," Journal of the Optical Society of America, vol. 65, pp. 59-64, January 1975.

31. C. B. Burckhardt, "Diffraction of a Plane Wave at a Sinusoidally Stratified Dielectric Grating," Journal of the Optical Society of America, vol. 56, pp. 1502-1509, November 1966.

32. P. Phariseau, "On the Diffraction of Light by Progressive Supersonic Waves," Proceeding of the Indian Academy of Science, vol. 44A, pp. 165-170, October 1956.

33. C. F. Quate, C. D. W. Wilkinson, and D. K. Winslow, "Interaction of Light and Microwave Sound," Proceedings of IEEE, vol. 53, pp. 1604-1623, October 1965.

34. R. S. Chu and T. Tamir, "Guided-wave Theory of Light Diffraction by Acoustic Microwaves," IEEE Transactions on Microwave Theory and Techniques, vol. MTT-18, pp. 486-504, August 1970.

35. H. Kogelnik, "Bragg Diffraction in Hologram Gratings with Internal Reflection," Journal of the Optical Society of America, vol. 57, pp. 431-433, March 1967.

BIBLIOGRAPHY (Continued)

36. F. G. Kaspar, "Diffraction by Thick, Periodically Stratified Gratings with Complex Dielectric Constant," Journal of the Optical Society of America, vol. 63, pp. 37-45, January 1973.

37. T. Tamir and H. C. Wang, "Scattering of Electromagnetic Waves by a Sinusoidal Stratified Half-space, I," Canadian Journal of Physics, vol. 44, pp. 2073-2093, September 1966.

38. T. Tamir, "Scattering of Electromagnetic Waves by a Sinusoidal Stratified Half-space, II," Canadian Journal of Physics, vol. 44, pp. 2461-2494, October 1966.

39. D. A. Watkins, Topics in Electromagnetic Theory (Wiley, New York, 1958).

40. W. R. Klein, C. B. Tipnis, and E. A. Hiedemann, "Experimental Study of Fraunhofer Light Diffraction by Ultrasonic Beams of Moderately High Frequency at Oblique Incidence," Journal of the Acoustical Society of America, vol. 38, pp. 229-233, August 1965.

41. W. R. Klein, "Theoretical Efficiency of Bragg Devices," Proceedings of IEEE, vol. 54, pp. 803-804, May 1966.

42. M. G. Cohen and E. I. Gordon, "Acoustic Scattering of Light in a Fabry-Perot Resonator," The Bell System Technical Journal, vol. 45, pp. 945-966, July-August 1966.

43 D. Marcuse, Light Transmission Optics (Van Nostrand Reinhold, New York, 1972), p. 71.

44. W. W. Rigrod, "Diffraction Efficiency of Nonsinusoidal Bragg Reflection Gratings," Journal of the Optical Society of America, vol. 64, pp. 97-99, January 1974; vol. 64, p. 895E, 1974.

45. F. S. Chen, J. T. LaMacchia and D. B. Fraser, "Holographic Storage in Lithium Niobate," Applied Physics Letters, vol. 13, pp. 223-225, October 1, 1968.

46. S. F. Su and T. K. Gaylord, "Unified Approach to the Formation of Phase Holograms in Ferroelectric Crystals," Journal of Applied Physics, vol. 46, pp. 5208-5213, December 1975.

47. G. A. Alphonse, R. C. Alig, D. L. Staebler, and W. Phillips, "Time-dependent Characteristics of Photo-induced Space-charge Field and Phase Holograms in Lithium Niobate and Other Photorefractive Media," RCA Review, vol. 36, pp. 213-229, June 1975.

BIBLIOGRAPHY (Continued)

48. W. D. Cornish, M. G. Moharam, and L. Young, "Effects of Applied-fields on Hologram Writing in Lithium Niobate," (unpublished).

49. D. L. Staebler and J. J. Amodei, "Coupled-wave Analysis of Holographic Storage in $LiNbO_3$," Journal of Applied Physics, vol. 43, pp. 1042-1049, March 1972.

50. S. F. Su and T. K. Gaylord, "A Procedure for Determining Unknown Optically-induced Refractive Index Profiles of Thick Gratings in Ferroelectric Crystals," (to be published).

51. G. W. Stroke, Handbuch der Physik, vol. 29, p. 426, 1965.

52. Standards on Piezoelectric Crystals, Proceedings of Institute of Radio Engineers, vol. 37, pp. 1378-1395, 1949.

53. E. H. Turner, "High-frequency Electro-optic Coefficients of Lithium Niobate," Applied Physics Letters, vol. 8, pp. 303-304, June 1, 1966.

54. Y. Ohmori, Y. Yasojima, and Y. Inuishi, "Control of Optical Damage in Reduced $LiNbO_3$ by External Applied Field," Applied Physics Letters, vol. 25, pp. 716-717, December 15, 1974.

55. W. D. Cornish and L. Young, "Influence of Multiple Internal Reflections on Diffraction Efficiency of Holograms Stored in Lithium Niobate," Journal of Applied Physics, vol. 46, pp. 1252-1254, March 1975.

56. M. Born and E. Wolf, Principles of Optics (Pergamon Press, London, 1959), pp. 61-62.

57. A. Yariv, Introduction to Optical Electronics (Holt, Rinehart and Winston, New York, 1971), p. 12.

VITA

Shing-fong Su was born in Taichung Hsien, Taiwan on October 1, 1946. He is the youngest son of Swei-Sun Su and Thou-Thwey Su. On December 21, 1971 he was married to Terry Bih-hwa Lin of Taiwan and they have one son, Johnny Su.

He graduated from Taichung First High School, Taichung, Taiwan in 1965. In 1969, he received a B.S. in Electrical Engineering from the National Taiwan University in Taipei, Taiwan. He received an M.S. in Electrical Engineering from the University of New Hampshire, Durham, New Hampshire in 1972.

From 1969 to 1970, he was with the Chinese Navy as a second lieutenant. From 1972 to 1975, he was a Graduate Research Assistant in the School of Electrical Engineering, Georgia Institute of Technology.